

REPORT DOCUMENTATION PAGE				Form Approved OMB No. 0704-0188	
Public reporting burden for this collection of information is estimated to average 1 hour per response, including the time for reviewing instructions, searching existing data sources, gathering and maintaining the data needed, and completing and reviewing this collection of information. Send comments regarding this burden estimate or any other aspect of this collection of information, including suggestions for reducing this burden to Department of Defense, Washington Headquarters Services, Directorate for Information Operations and Reports (0704-0188), 1215 Jefferson Davis Highway, Suite 1204, Arlington, VA 22202-4302. Respondents should be aware that notwithstanding any other provision of law, no person shall be subject to any penalty for failing to comply with a collection of information if it does not display a currently valid OMB control number. PLEASE DO NOT RETURN YOUR FORM TO THE ABOVE ADDRESS.					
1. REPORT DATE (DD-MM-YYYY) 22-08-2013		2. REPORT TYPE Final		3. DATES COVERED (From - To) 02-10-2008 to 31-10-2013	
4. TITLE AND SUBTITLE Turbulent Flow and Large Surface Wave Events in the Marine Boundary Layers				5a. CONTRACT NUMBER N00014-09-C-0091	
				5b. GRANT NUMBER	
				5c. PROGRAM ELEMENT NUMBER	
6. AUTHOR(S) Peter P Sullivan - National Center for Atmospheric Research James C McWilliams - Department of Atmospheric Sciences and Institute of Geophysics and Planetary Physics, UCLA				5d. PROJECT NUMBER	
				5e. TASK NUMBER	
				5f. WORK UNIT NUMBER	
7. PERFORMING ORGANIZATION NAME(S) AND ADDRESS(ES) University Corporation for Atmospheric Research PO Box 3000 Boulder, CO 80307-3000				8. PERFORMING ORGANIZATION REPORT NUMBER n/a	
9. SPONSORING / MONITORING AGENCY NAME(S) AND ADDRESS(ES) Office of Naval Research Regional Office Seattle-N63374 300 Fifth Ave, Suite 710 Seattle, WA 98104				10. SPONSOR/MONITOR'S ACRONYM(S)	
				11. SPONSOR/MONITOR'S REPORT NUMBER(S)	
12. DISTRIBUTION / AVAILABILITY STATEMENT Distribution A - For Public Release, Distribution Unlimited					
13. SUPPLEMENTARY NOTES					
14. ABSTRACT A massively parallel large-eddy simulation (LES) code for atmospheric planetary boundary layers (PBLs) above moving and stationary waves is described.					
15. SUBJECT TERMS					
16. SECURITY CLASSIFICATION OF:			17. LIMITATION OF ABSTRACT UU	18. NUMBER OF PAGES 117 incl cover form	19a. NAME OF RESPONSIBLE PERSON Peter Sullivan
a. REPORT U	b. ABSTRACT U	c. THIS PAGE U			19b. TELEPHONE NUMBER (include area code) 303-497-8953

TURBULENT FLOW AND LARGE SURFACE WAVE EVENTS IN THE MARINE BOUNDARY LAYERS

Peter P. Sullivan¹ and James C. McWilliams²

¹National Center for Atmospheric Research

²Department of Atmospheric And Oceanic Sciences, UCLA

NCAR is sponsored by the National Science Foundation

Support from Office of Naval Research

HIGH RESOLUTION AIR-SEA INTERACTION DRI

GOALS AND ACCOMPLISHMENTS

Technical goal:

- Next generation LES model of the marine PBL with a phased resolved spectrum of surface waves $\lambda > \mathcal{O}(10m)$
- Use measured 2D wave fields as surface boundary conditions

Science goals:

- Wind response to transients, mis-aligned winds and waves, non-equilibrium winds and waves
- Variation of surface layer winds with wave age C_p/U_{10}

TECHNICAL ACCOMPLISHMENTS

Built a 3-D LES model for a full marine PBL with a spectrum of resolved time-varying surface waves at the lower boundary

- Non-orthogonal, moving meshes that track the time varying surface
- Co-located arrangement of flow variables (compact stencil)
- Can impose a realistic 2-D wave spectrum with random phases. Waves are advanced in time using the dispersion relation
- Rough-wall high Reynolds number boundary conditions
- Accounts for the wave motion (orbital velocities)
- Allows “steep” waves $ak \sim 0.3$
- Applicable to stationary terrain (*e.g.*, 3D hills and bumps)
- Mesh spacing $(\Delta x, \Delta y, \Delta z) \sim \mathcal{O}(1m)$ near the water surface.
- Meshes are $1024 \times 1024 \times 512$ gridpoints
- Fully parallel MPI implementation (tested with as many as 8192 cores)

Manuscript:

A large eddy simulation model of turbulent atmospheric boundary layers with time-dependent and stationary surface-following grids

RECENT LES CODE IMPROVEMENTS

- Option to impose Donelan (1985) empirical wave spectrum

$$E(\omega, \phi) = D(\omega, \phi)F(\omega)$$

- Fixes to the surface boundary conditions for the wave orbital velocities given wave height $h = h(x, y, t)$

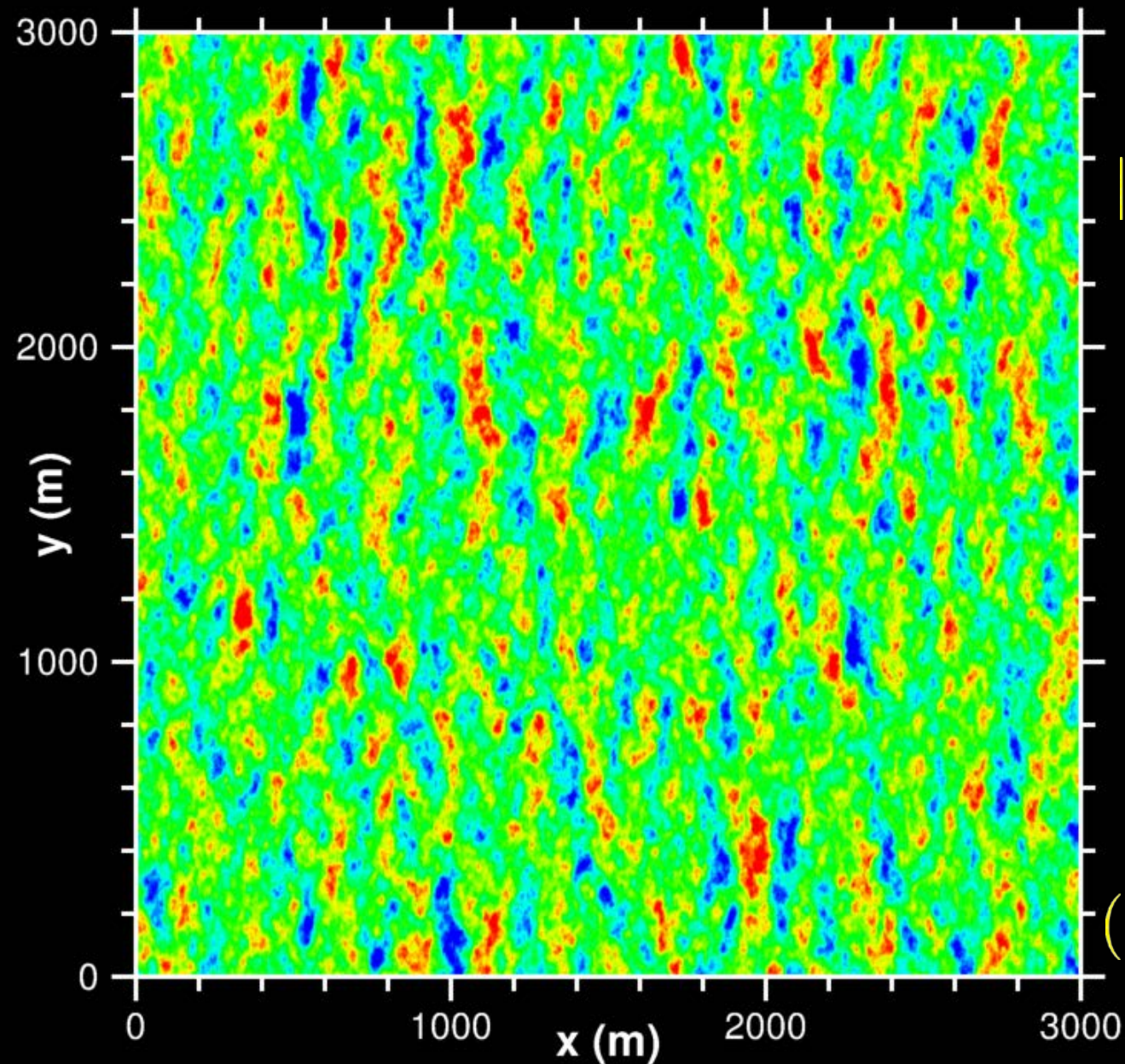
$$w_o = \frac{\partial h}{\partial t} + u_o \frac{\partial h}{\partial x} + v_o \frac{\partial h}{\partial y}$$

- Proper boundary condition for the ghost point pressure for non-orthogonal grids (important fix for waves and hills)
- Improved grid generation (smoother grids)
- Timing associated with advancing the wavefields
- Ability to impose wave shapes from wind-wave tank simulations
- Improved convergence of pressure solver for spilling breakers



Snapshot of wave height

$$|\eta(x, y, t)| \leq 7.5(m)$$



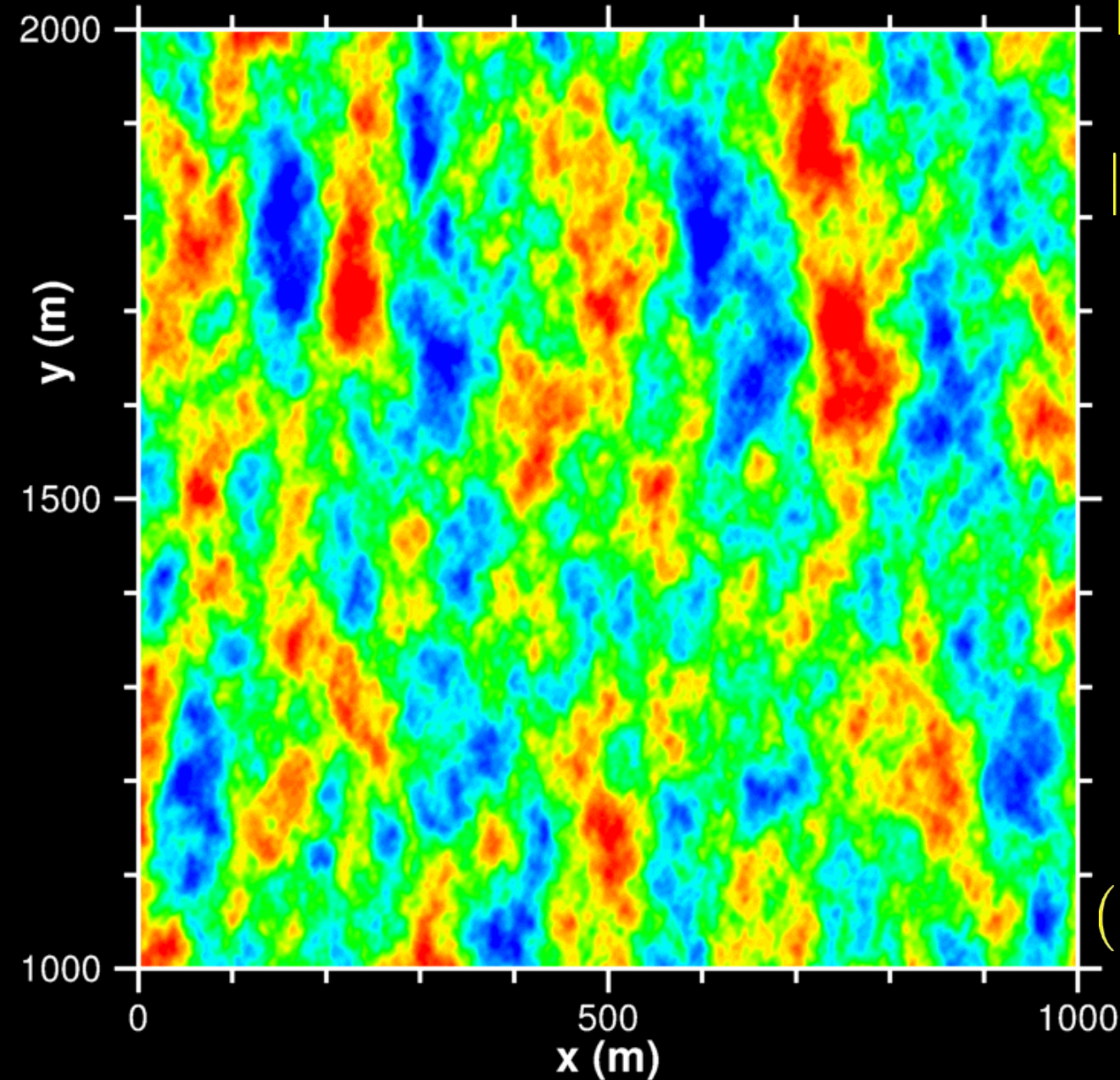
$$(\Delta x, \Delta y) = 2.9 m$$



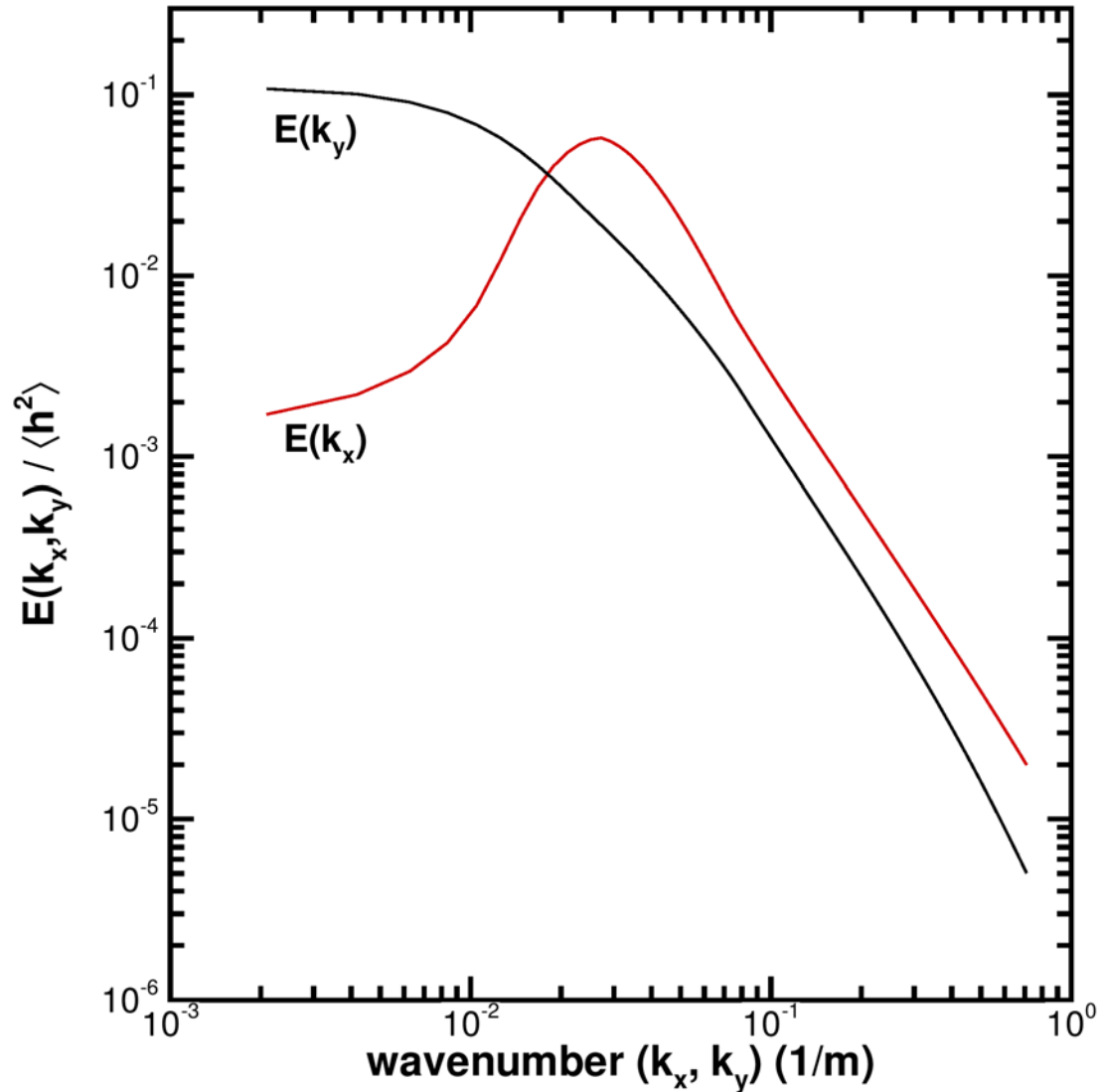
Snapshot of wave height

$$|\eta(x, y, t)| \leq 7.5(m)$$

$$(\Delta x, \Delta y) = 2.9 m$$

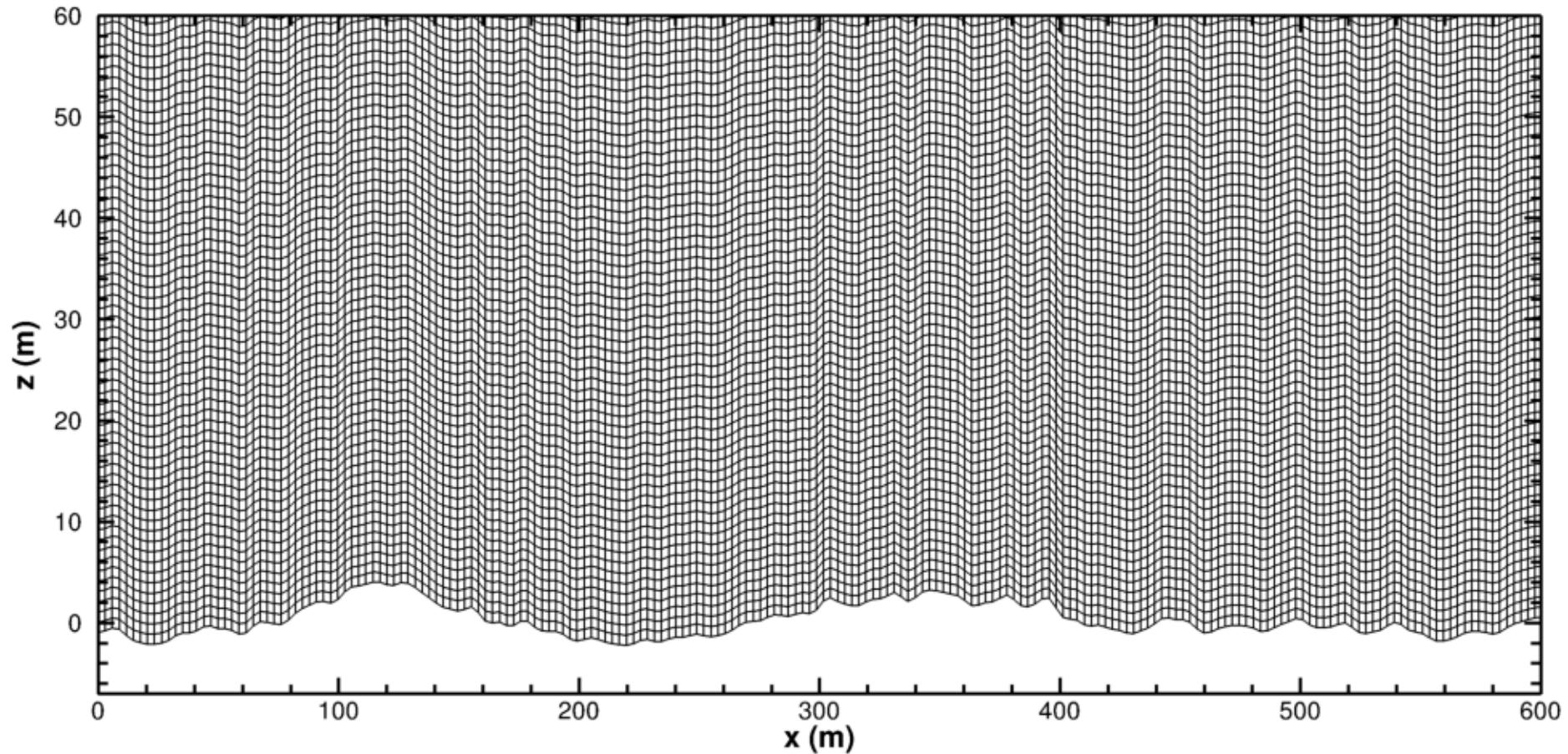


SURFACE WAVE FIELDS



Horizontal grid resolution of the LES equals the max. wavenumber in the wave spectrum

GRID MOVEMENT IN THE LOWER BOUNDARY LAYER



Grid speed $z_t = f(\xi, \eta, \zeta, t)$

LES INVESTIGATIONS OF WIND-WAVE INTERACTION

LES database (incomplete):

- Imposed waves using Donelan spectrum
- Neutral and weakly unstable with $Ug = [5 - 25] \text{ m s}^{-1}$
- Wave age $C_p/U_{10} = [1.1 - 4.8]$ ← New

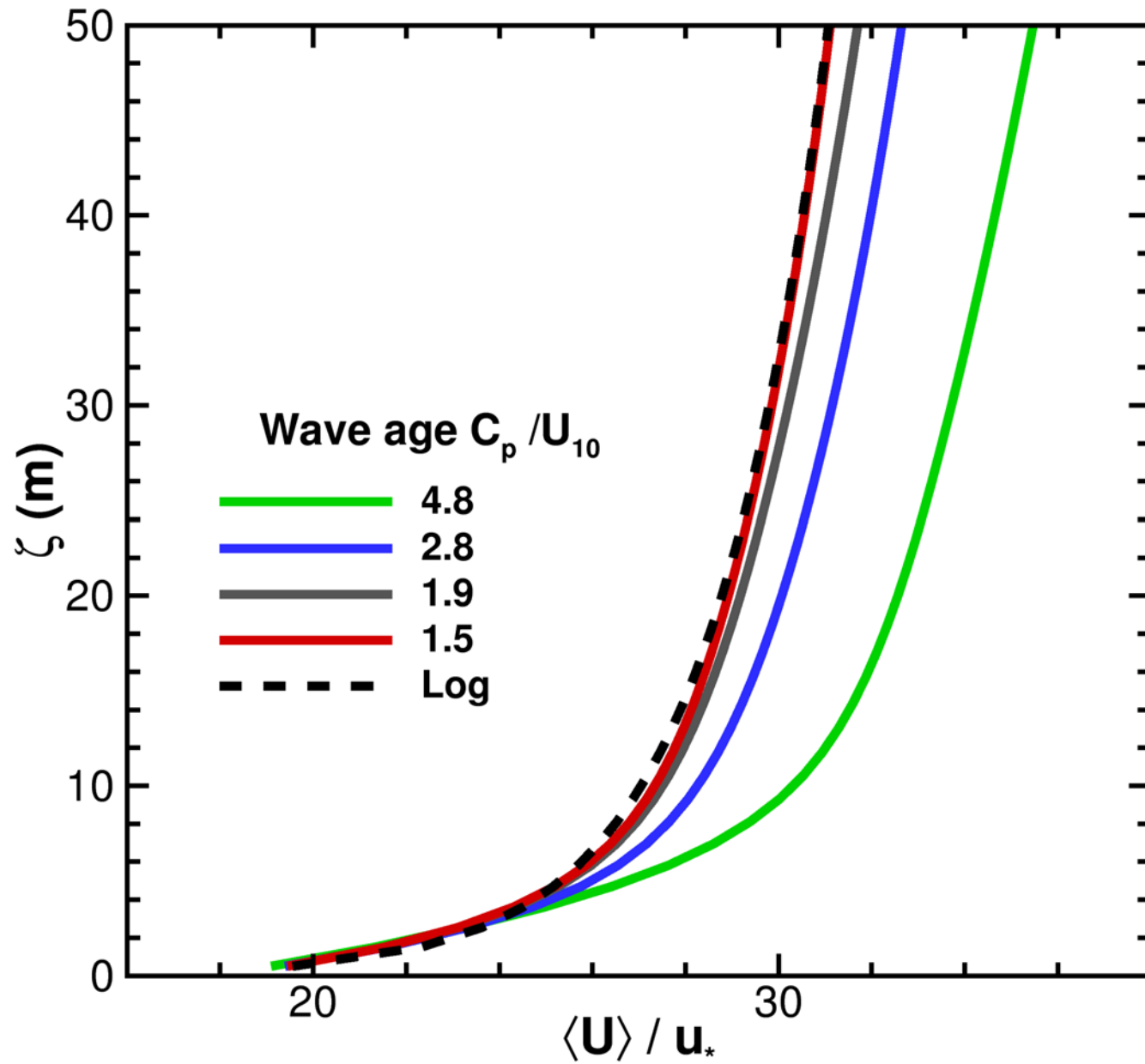
Differences between slow waves, fast waves and stationary bumps:

- Flow structures
- Velocity and pressure fields
- Statistics (means, variances, fluxes)
- Clear dependence on wave age in surface layer
- Non-equilibrium situations are intriguing

Manuscript:

Large eddy simulations of marine atmospheric boundary layers with a resolved spectrum of surface waves

VERTICAL PROFILE OF MEAN WIND



WORK STILL IN PROGRESS

- Fine mesh resolution runs on “Yellowstone”
- Simulations of laboratory breakers
- Site simulations of HiRES will not be completed with the current DRI funding

“YELLOWSTONE” COMPUTATIONAL AWARD

The NCAR-Wyoming supercomputer center is home to *Yellowstone*

- The largest IBM Idataplex in operation
- Peta-scale machine with 72,000 processors

Awarded Proposal: *Large eddy simulations of high wind atmospheric boundary layers above a spectrum of resolved moving wind waves*

- Total computational hours: 12×10^6
- Duration: 1 January 2013 - 31 December 2013
- Hours consumed to date: 5×10^6

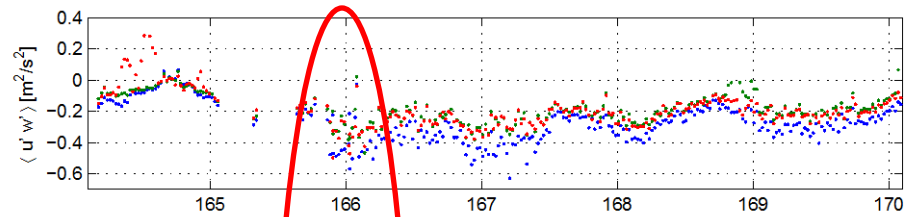
LES EXPERIMENTS ON YELLOWSTONE

- Slightly unstable flow $Q_* = 0.01 \text{ K m s}^{-1}$
- Geostrophic winds $U_g = [5, 25] \text{ m s}^{-1}$
- $z_i \sim 400 \text{ m}$, $z_o = 0.0002 \text{ m}$
- Donelan wave spectrum
- Wave age $C_p/U_{10} = [1.1 - 4.8]$
- Domain $(3000 \times 3000 \times 800) \text{ m}$
- Grid $(1024 \times 1024 \times 512)$ $\longleftarrow 0.5 \times 10^9 \text{ gridpoints}$
- $\Delta x = \Delta y = 2.9 \text{ m}$, $\Delta z = 1.0 \text{ m}$ at surface
- 2048 processors, $\sim 500,000$ “Yellowstone” core hours

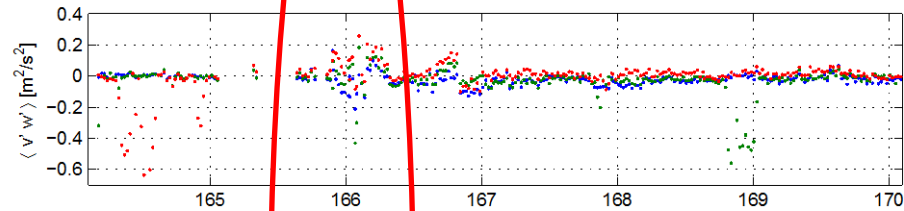
Multiple scales in the MABL: Can we capture them?

SURFACE FLUXES AND WIND SPEED FROM HIRES

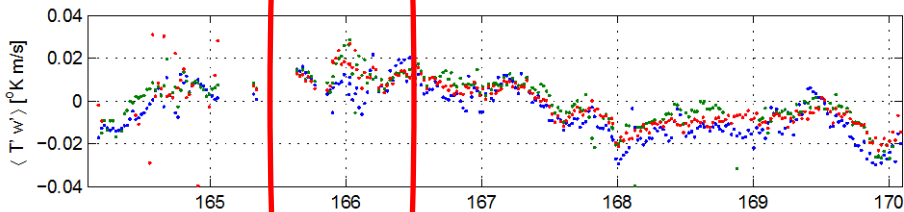
Momentum flux $u'w'$



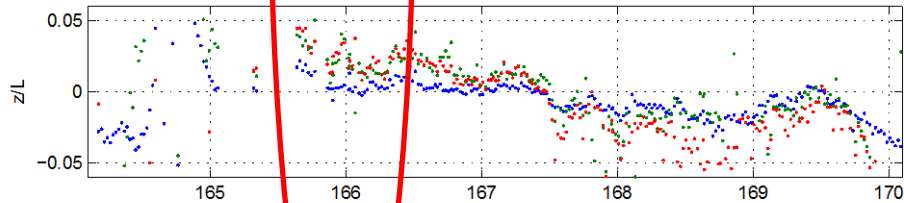
Momentum flux $v'w'$



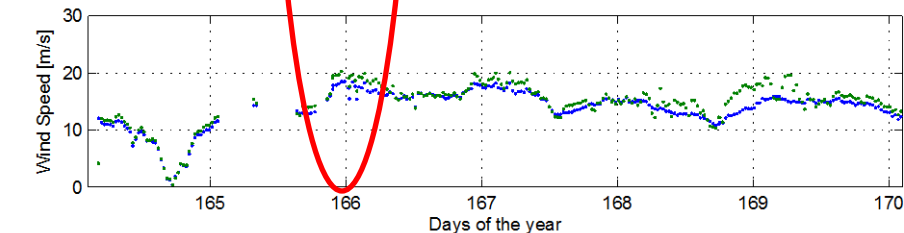
Temperature flux $T'w'$



Stability $-z/L$



Windspeed

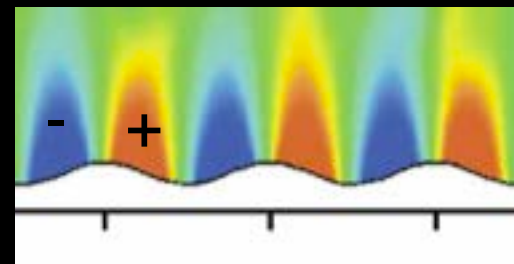
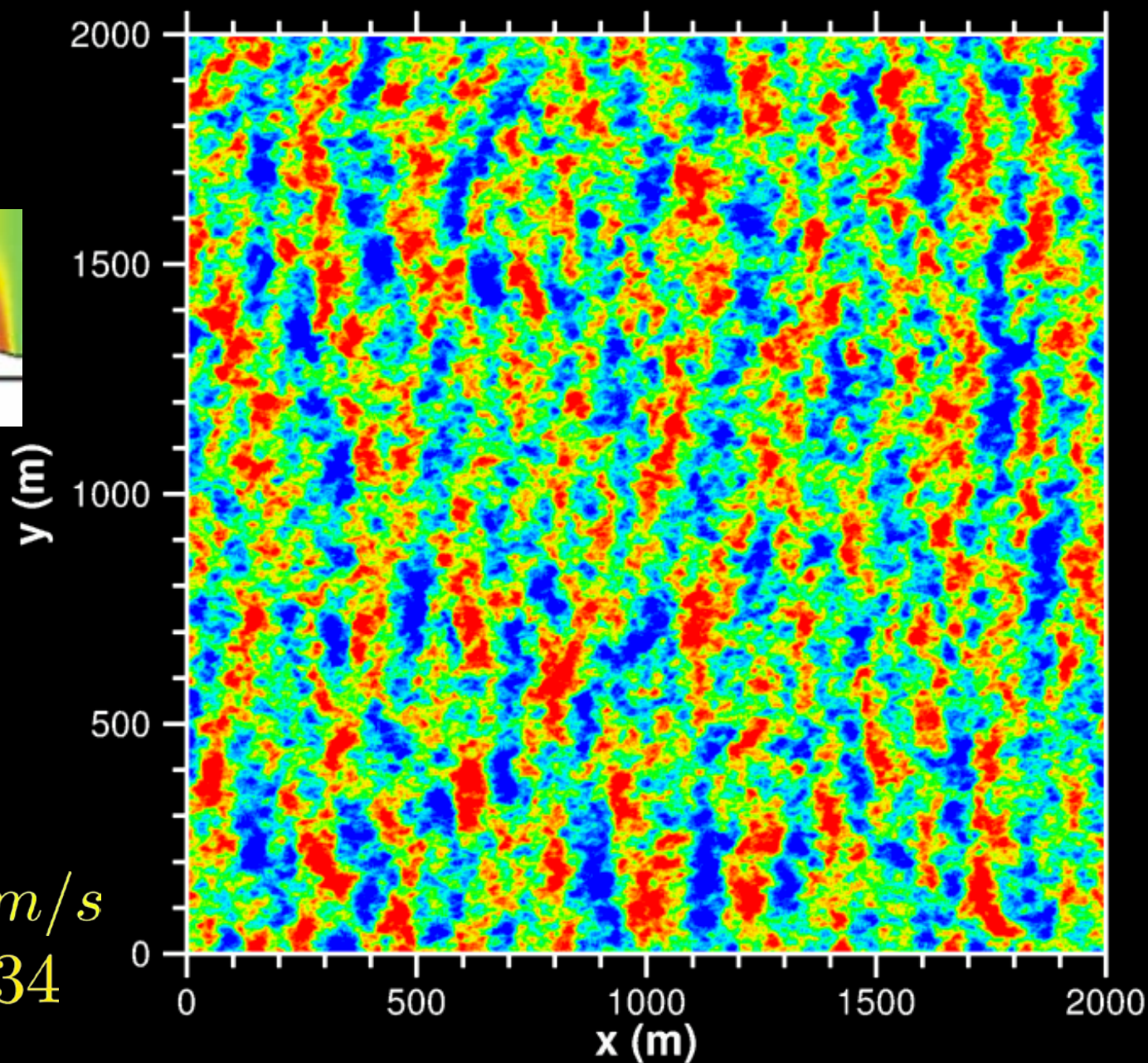


Most often a mixed regime of high winds and weak unstable/stable stability

Courtesy T. Hristov

w (m/s)

$z = 0.50$ m

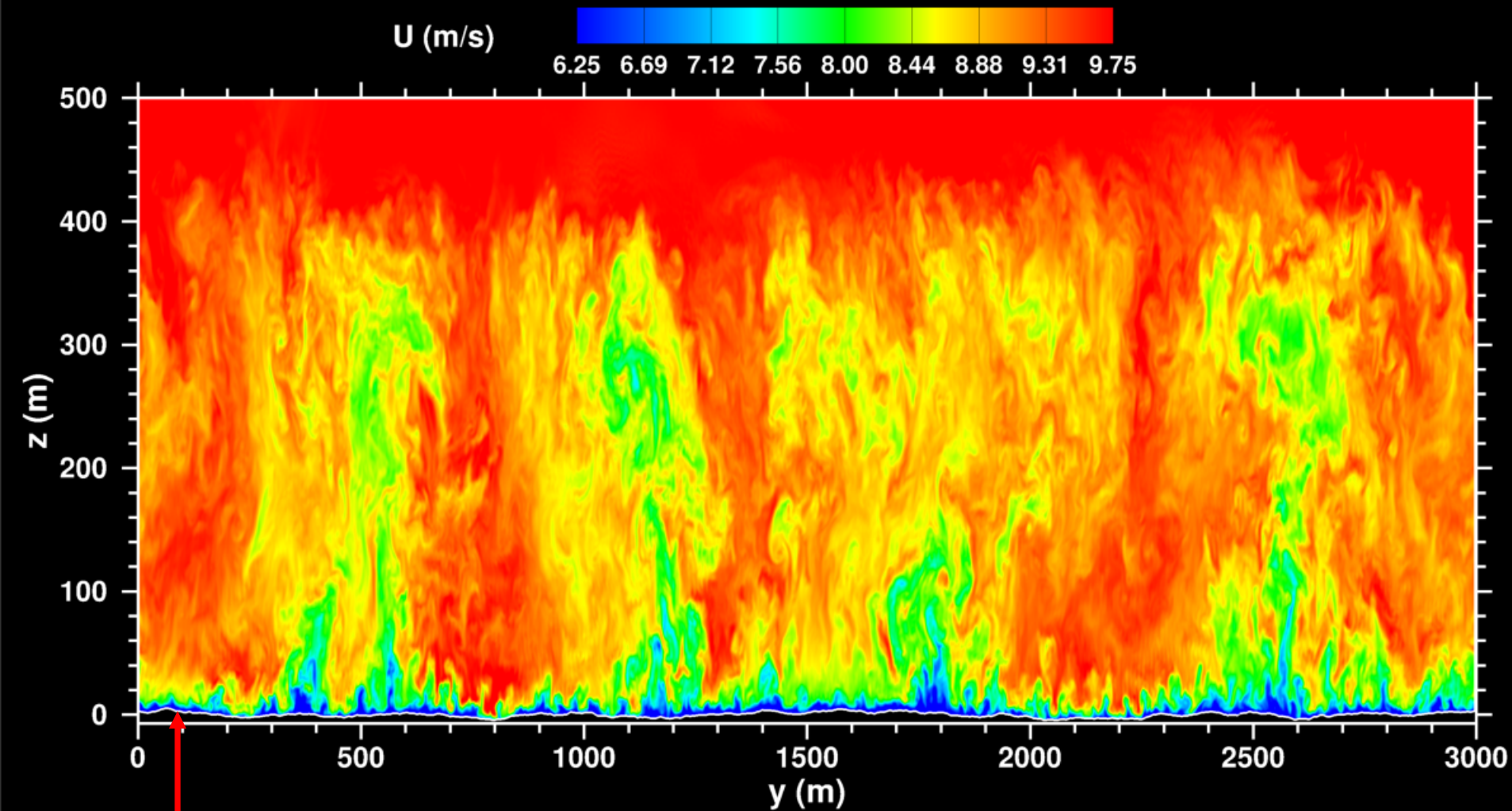


$$U_g = 10 \text{ m/s}$$

$$Q_* = 0.01 \text{ K m/s}$$

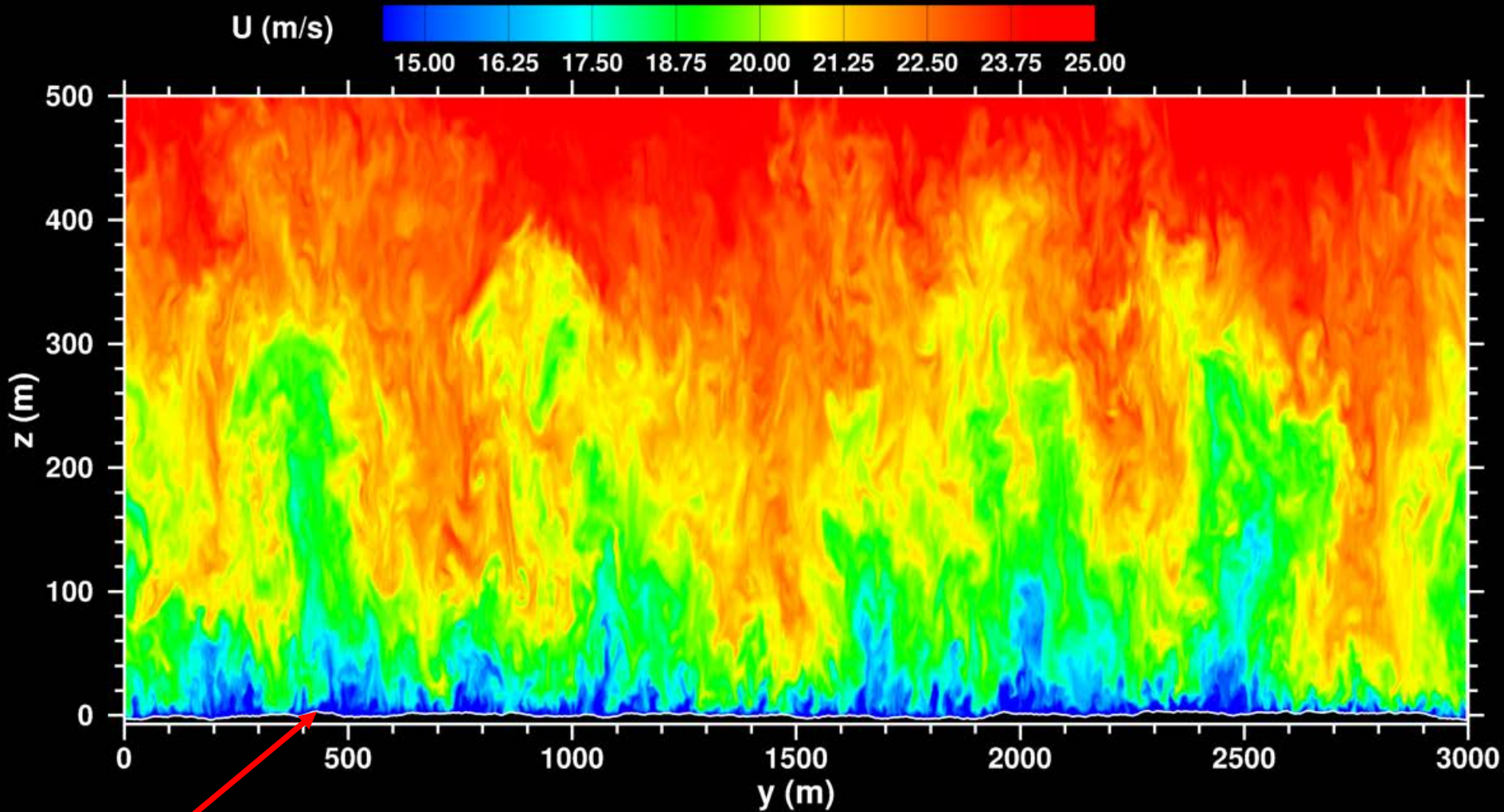
$$C_p/U_{10} = 2.34$$

U Contours in yz-plane, $U_g = 10$ m/s, $Q^* = 0.01$ K m/s



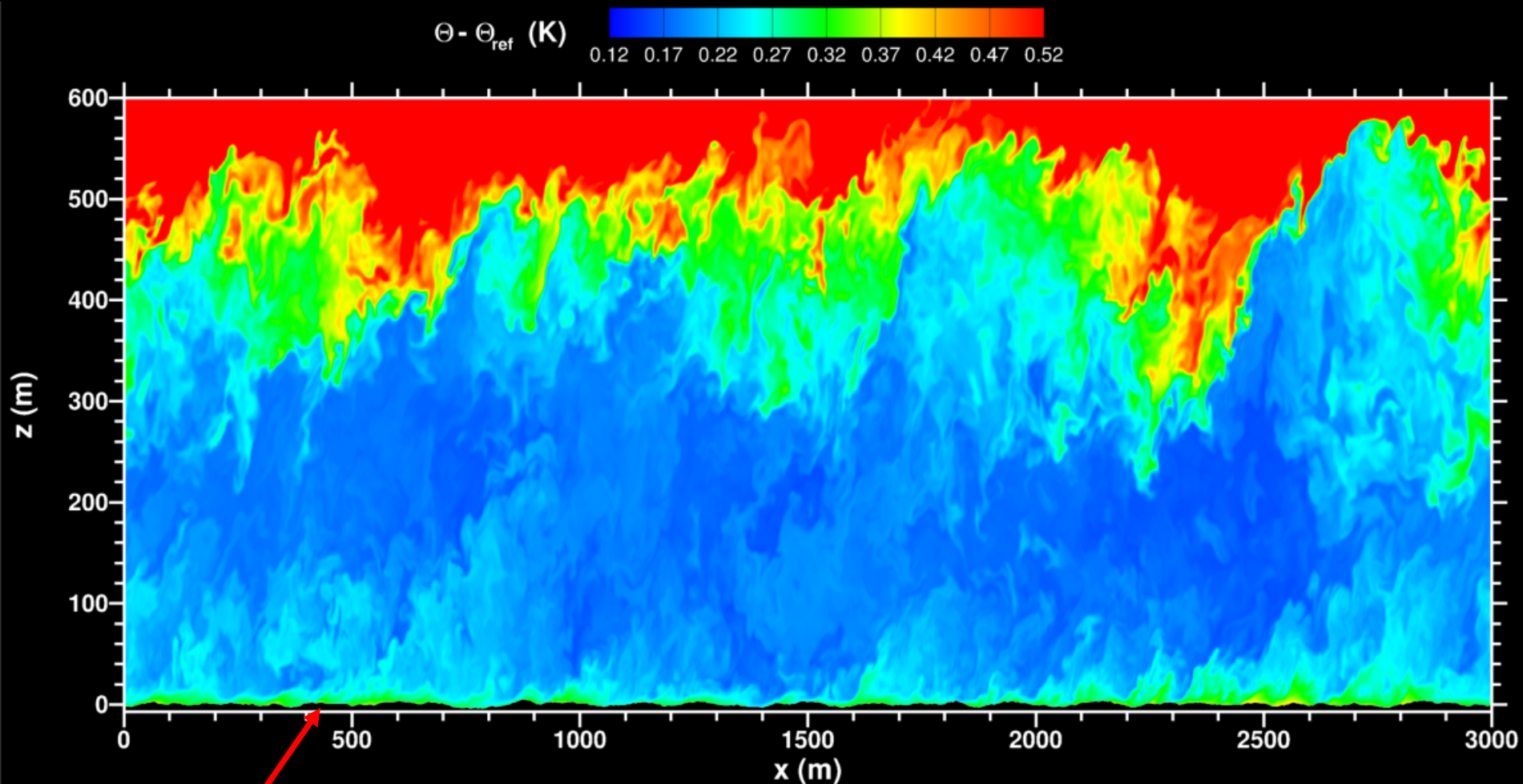
Wavy boundary

U Contours in yz-plane, $U_g = 25$ m/s, $Q^* = 0.01$ K m/s



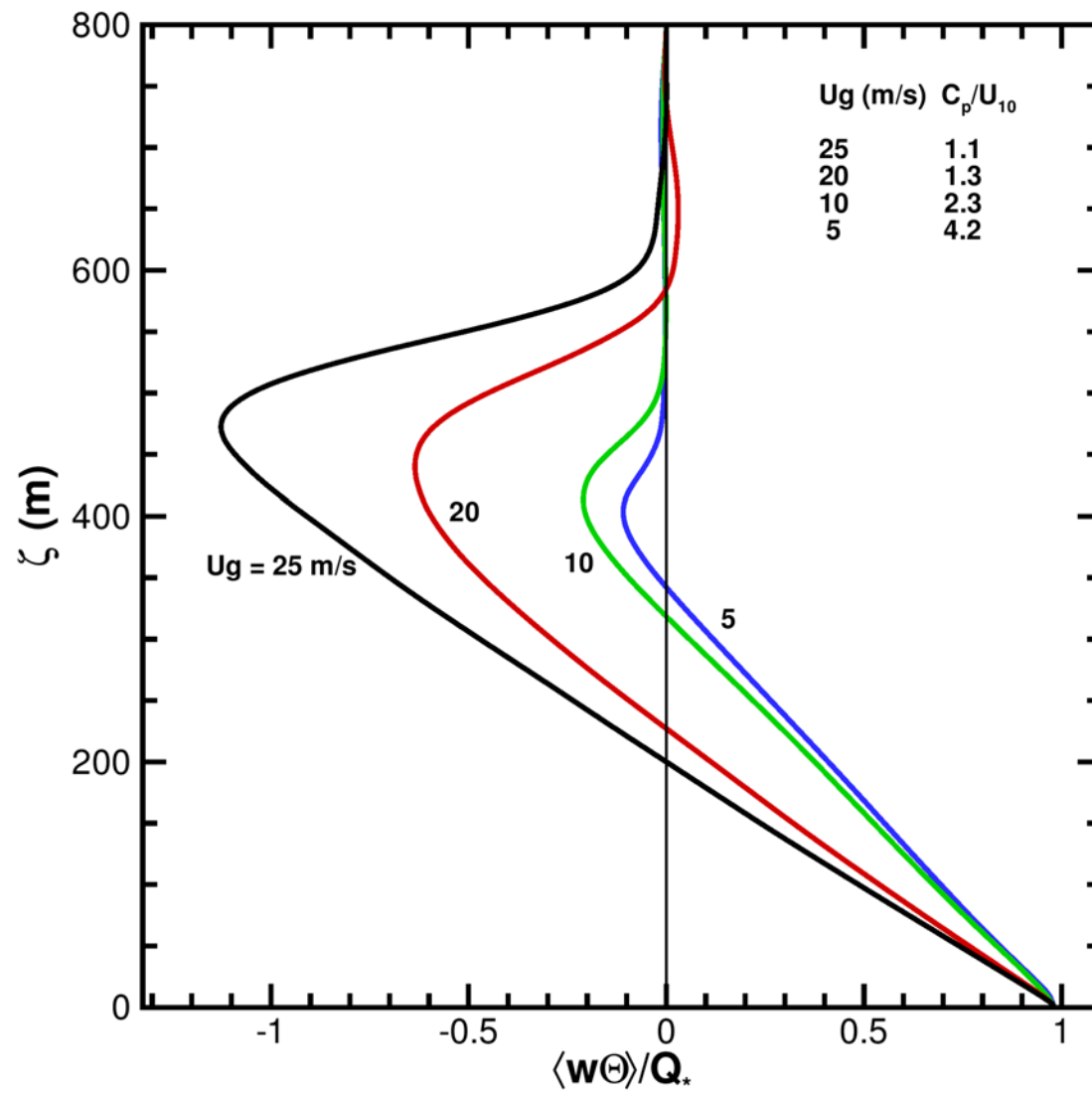
Wavy boundary

θ Contours in xz-plane, $U_g = 25$ m/s, $Q^* = 0.01$ K m/s



Wavy boundary

NORMALIZED TEMPERATURE FLUX $\langle W\theta' \rangle$

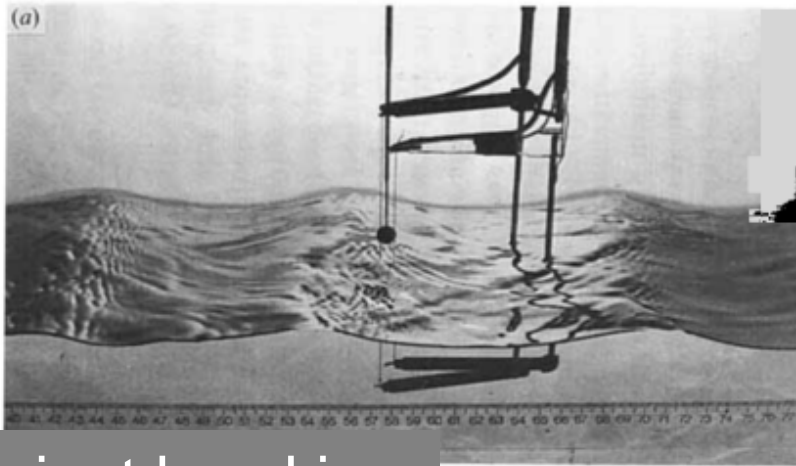


CLOUD STREETS OVER THE OCEAN

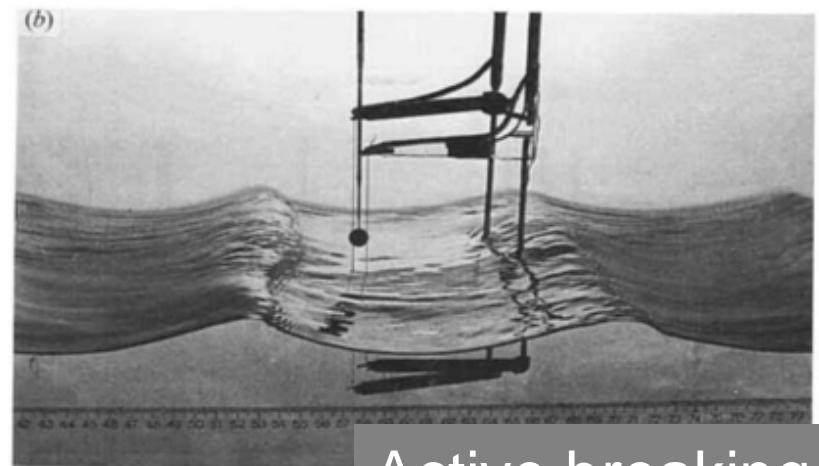


The influence of wave breaking on the surface pressure distribution in wind-wave interactions

By MICHAEL L. BANNER



Incipient breaking



Active breaking

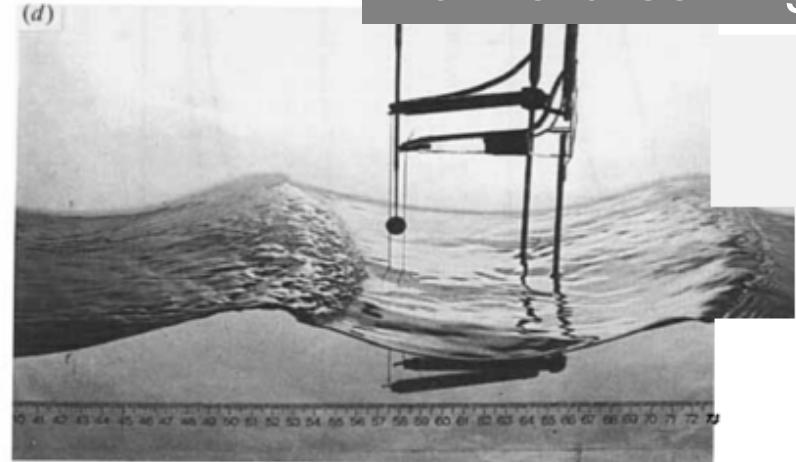
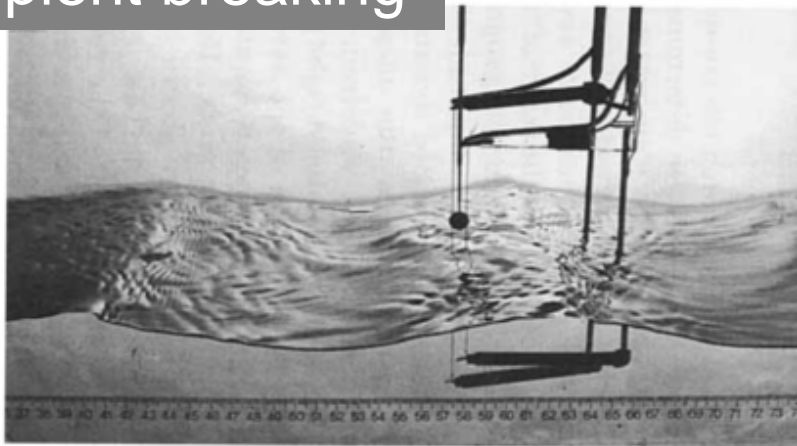
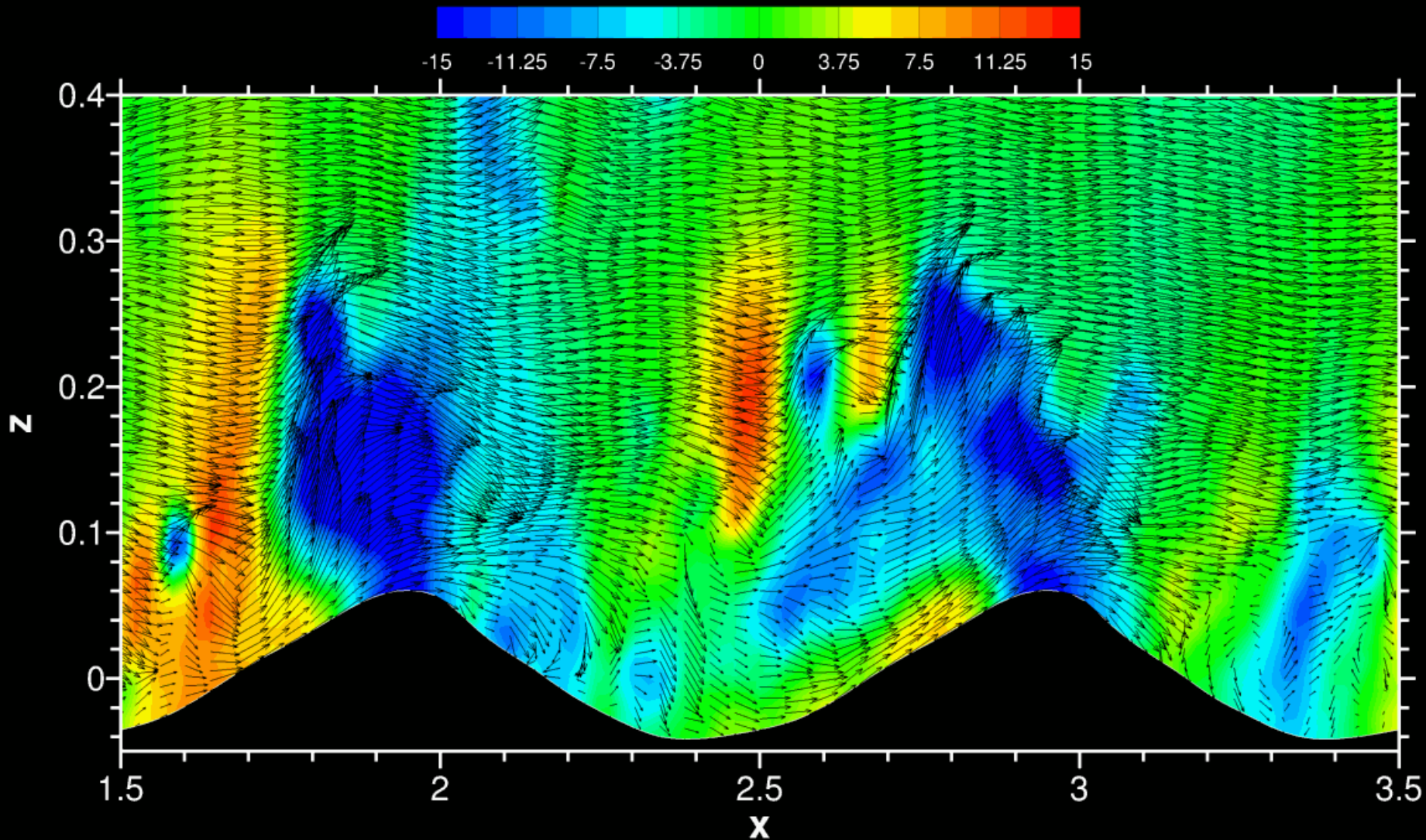
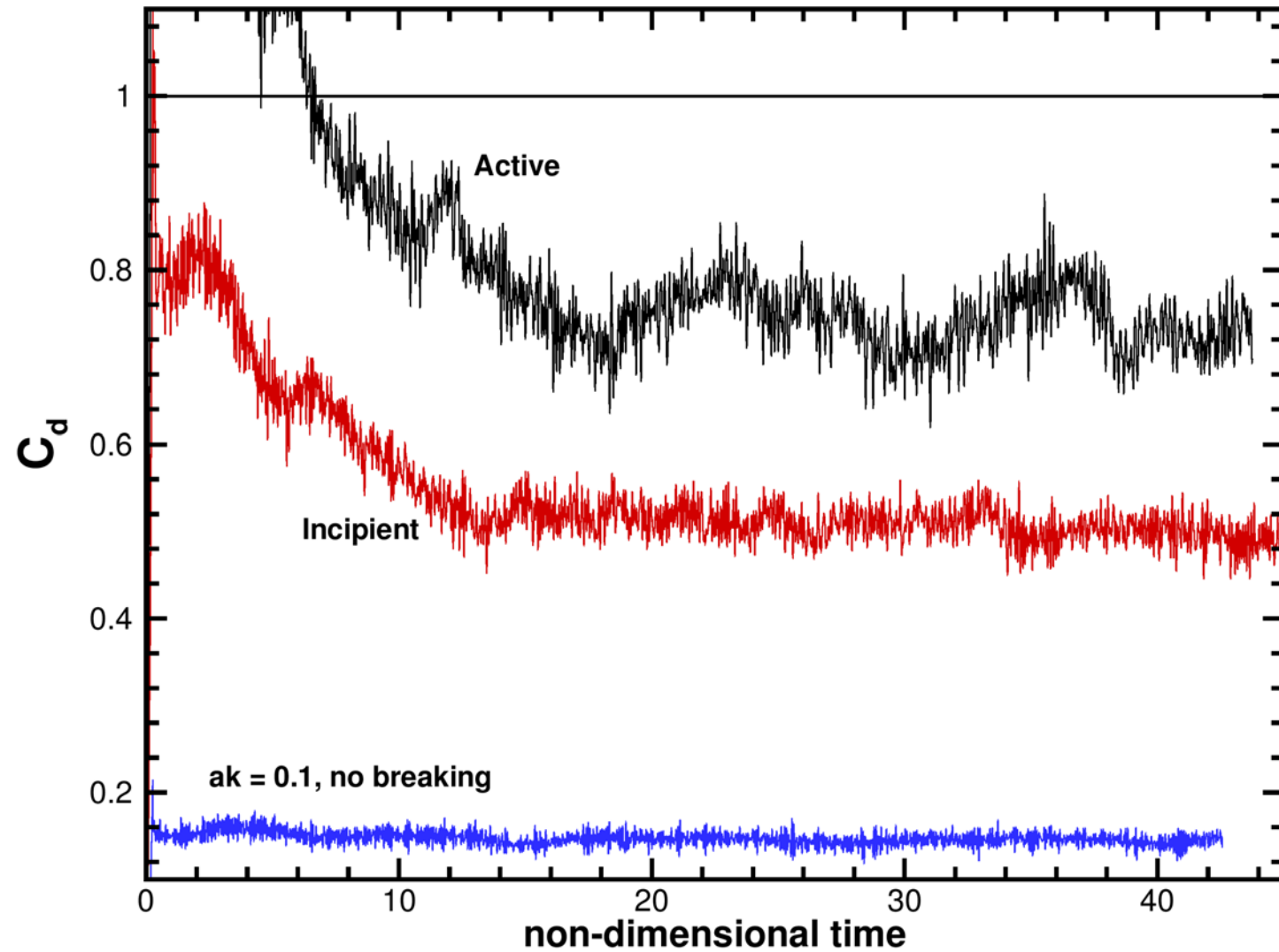


FIGURE 8. Photographs showing typical breaking and incipient breaking waves in the propagating wind-wave experiments. The horizontal lengthscale is in cm. The wind speed was 5.5 m/s from left to right. (a) 3.35 Hz incipient breaking waves. (b) 3.35 Hz breaking waves. (c) 2.85 Hz incipient breaking waves. (d) 2.85 Hz breaking waves.

(U,W) Vectors and Pressure over Active Breakers

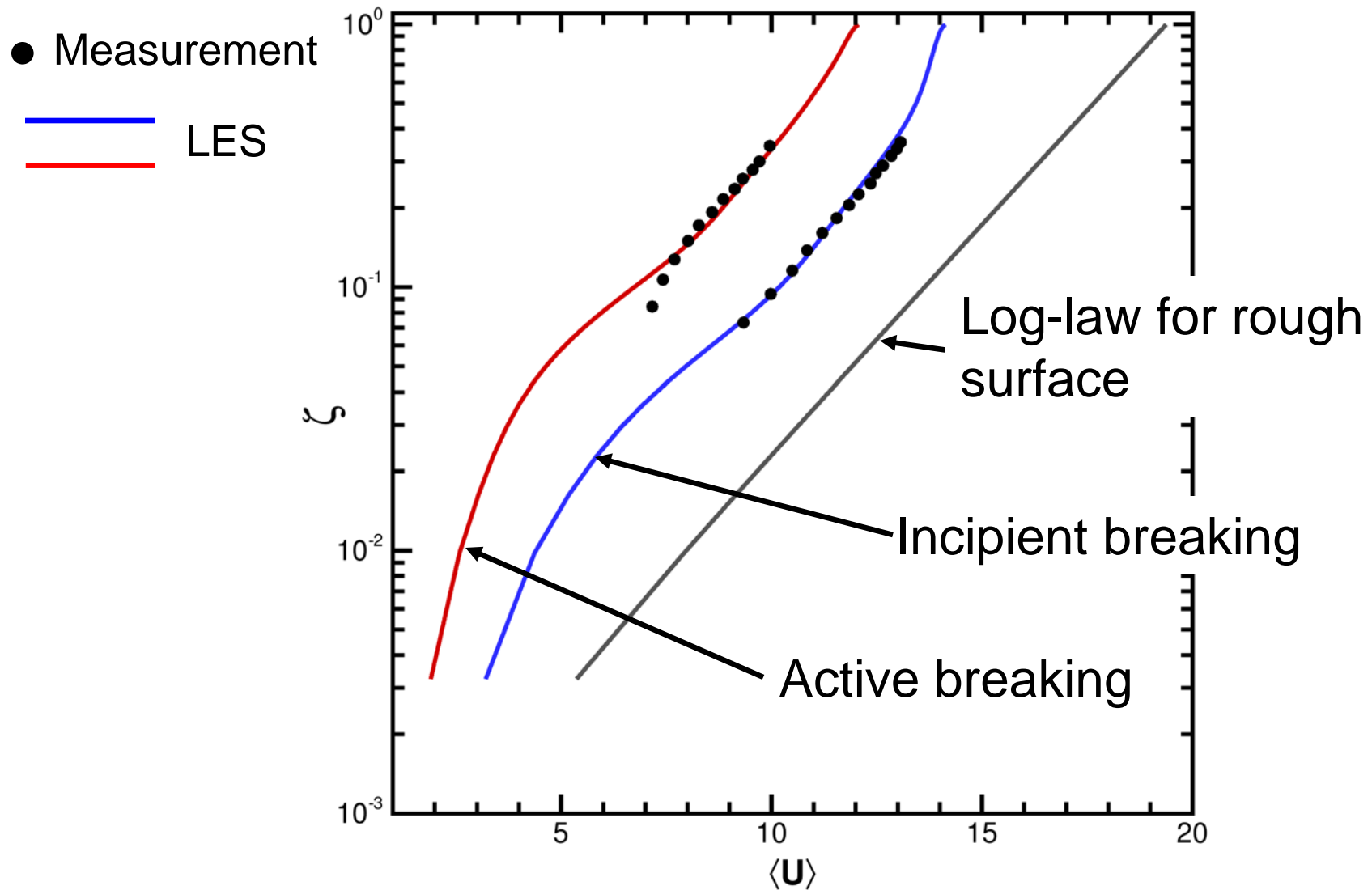


FORM DRAG OVER BREAKING LABORATORY WAVES



WIND PROFILES OVER BREAKING LABORATORY WAVES

LES-MEASUREMENT COMPARISON

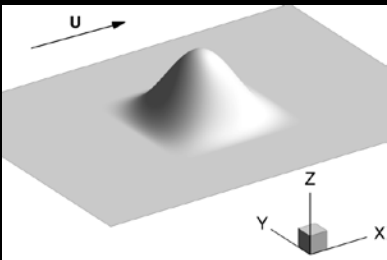


SUMMARY

- Coupled a LES for the marine PBL to a realistic 3D time-dependent wavefield
- Coordinate transform $\mathbf{x}_i \rightarrow \xi_i$ accounts for mesh movement
- LES of neutral and weakly unstable stratified flow above resolved waves
- Clear dependence on wave age in surface layer
- Competition between “wave pumping” and turbulence
- Carrying forward high resolution simulations with 10^9 gridpoints on Yellowstone using 2048 or more cores
- New LES for laboratory breaking waves
- HiRES site simulations are not planned under the current DRI
- Two manuscripts under construction
 - Algorithm Description
 - LES process studies of wind-wave interaction for a full marine PBL

MEETING PAPERS AND PRESENTATIONS

- 19th Boundary Layer & Turbulence Meeting, 2010 (2 extended abstracts)
- 20th Boundary Layer & Turbulence Meeting, 2012
- Direct & Large Eddy Simulation 9, 2013
- 6th Theoretical Fluid Mechanics Conference, AIAA, 2011
- Gulf of Mexico Oil Spill and Ecosystem Conference, 2013

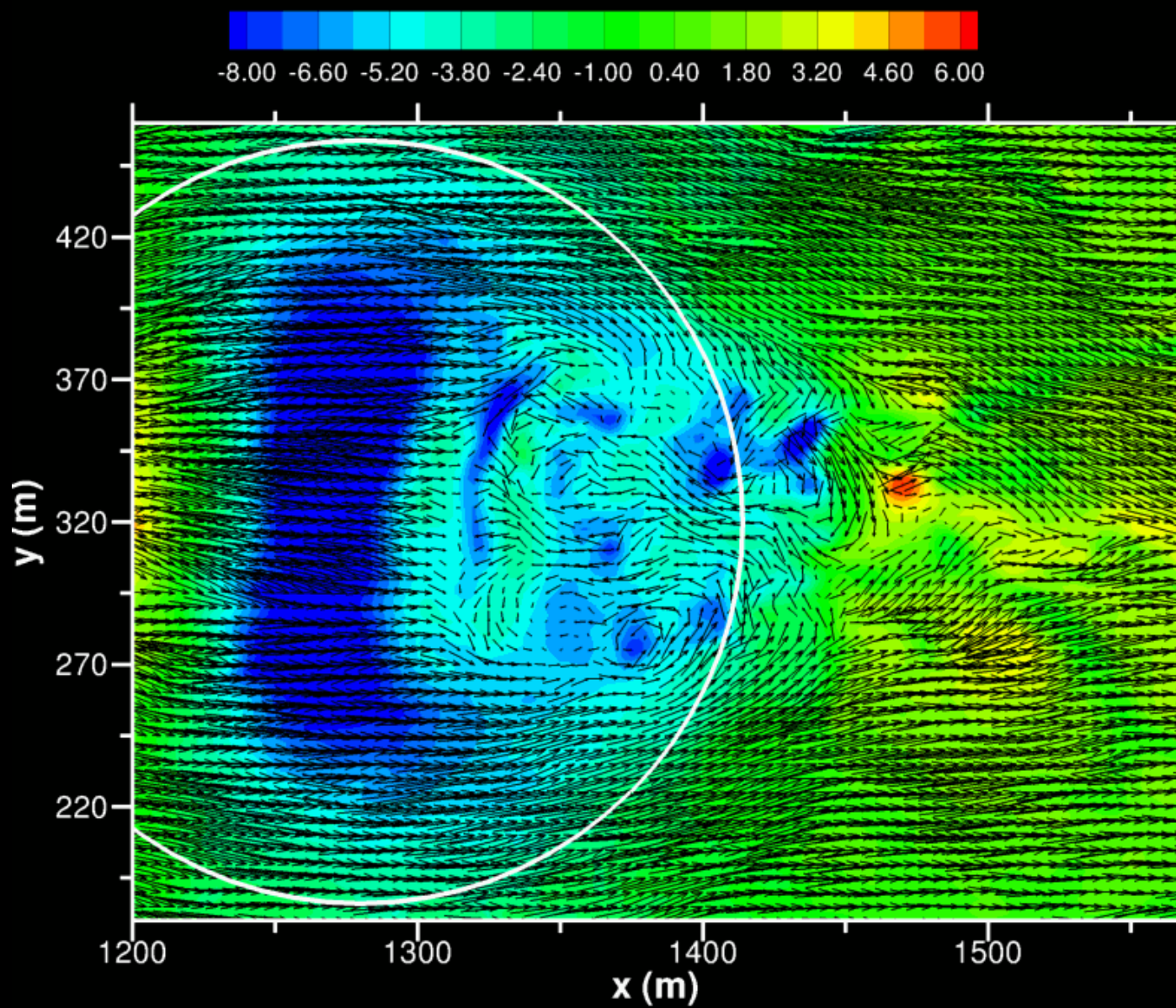


$$h = 50 \text{ m}$$

$$\mathcal{L} = 67 \text{ m}$$

$$\zeta \sim 5.6m$$

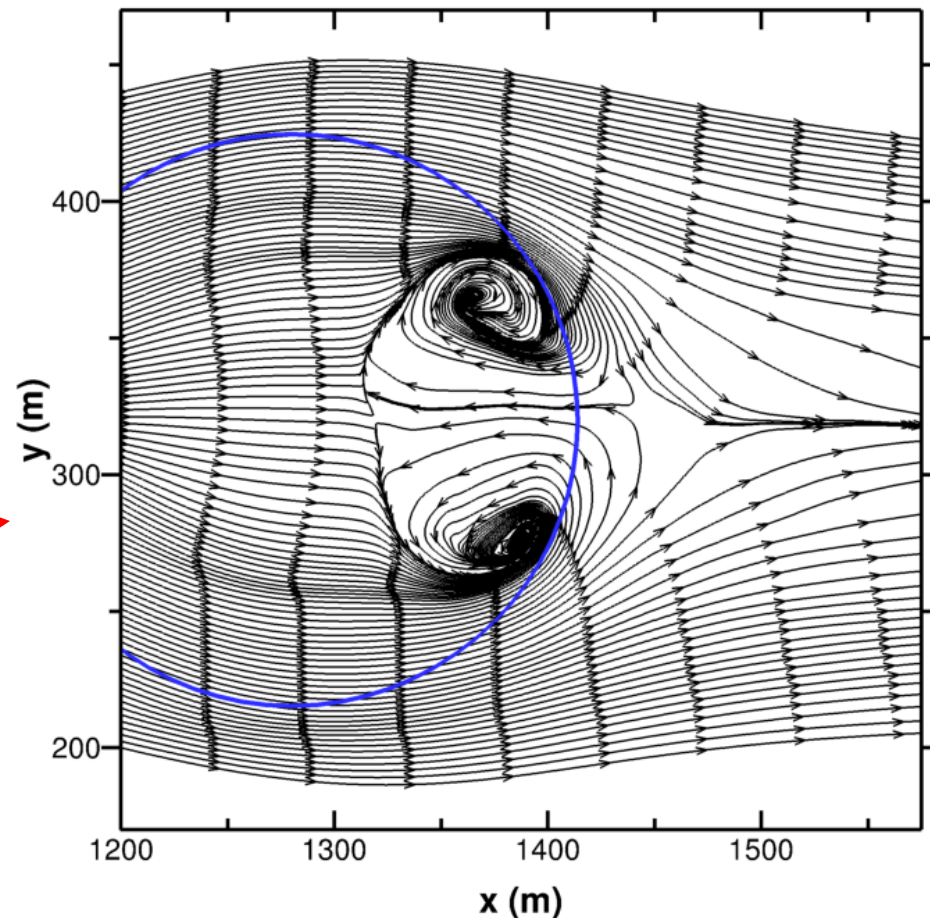
$$p' / \rho$$



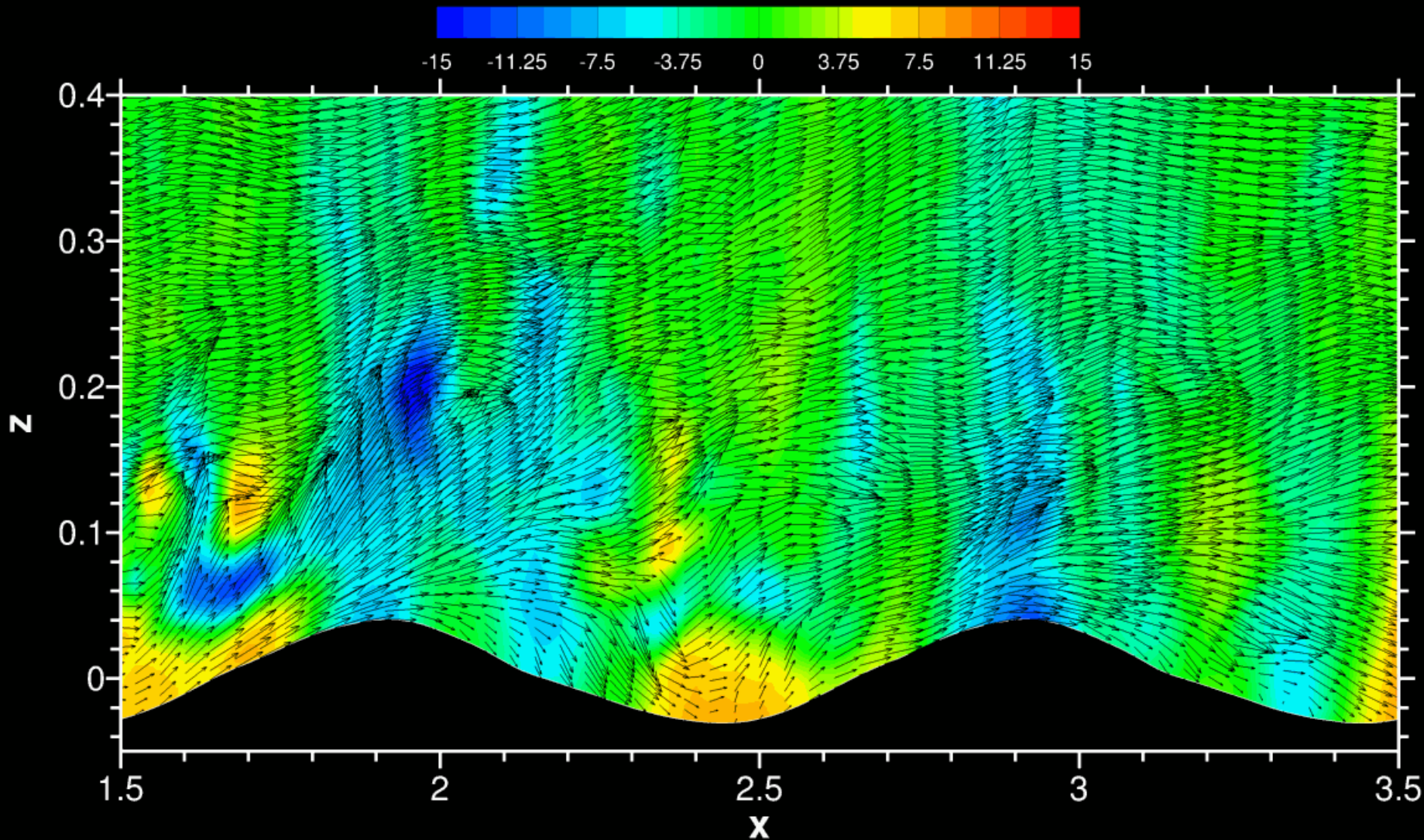
TURBULENT FLOW PAST A STEEP 3D HILL

- Multi-scale vortical wake flow
- Intermittent pair of vortices near hill base
- Complex separation over hill crest and flanks
- 3D flow patterns distinct from 2D

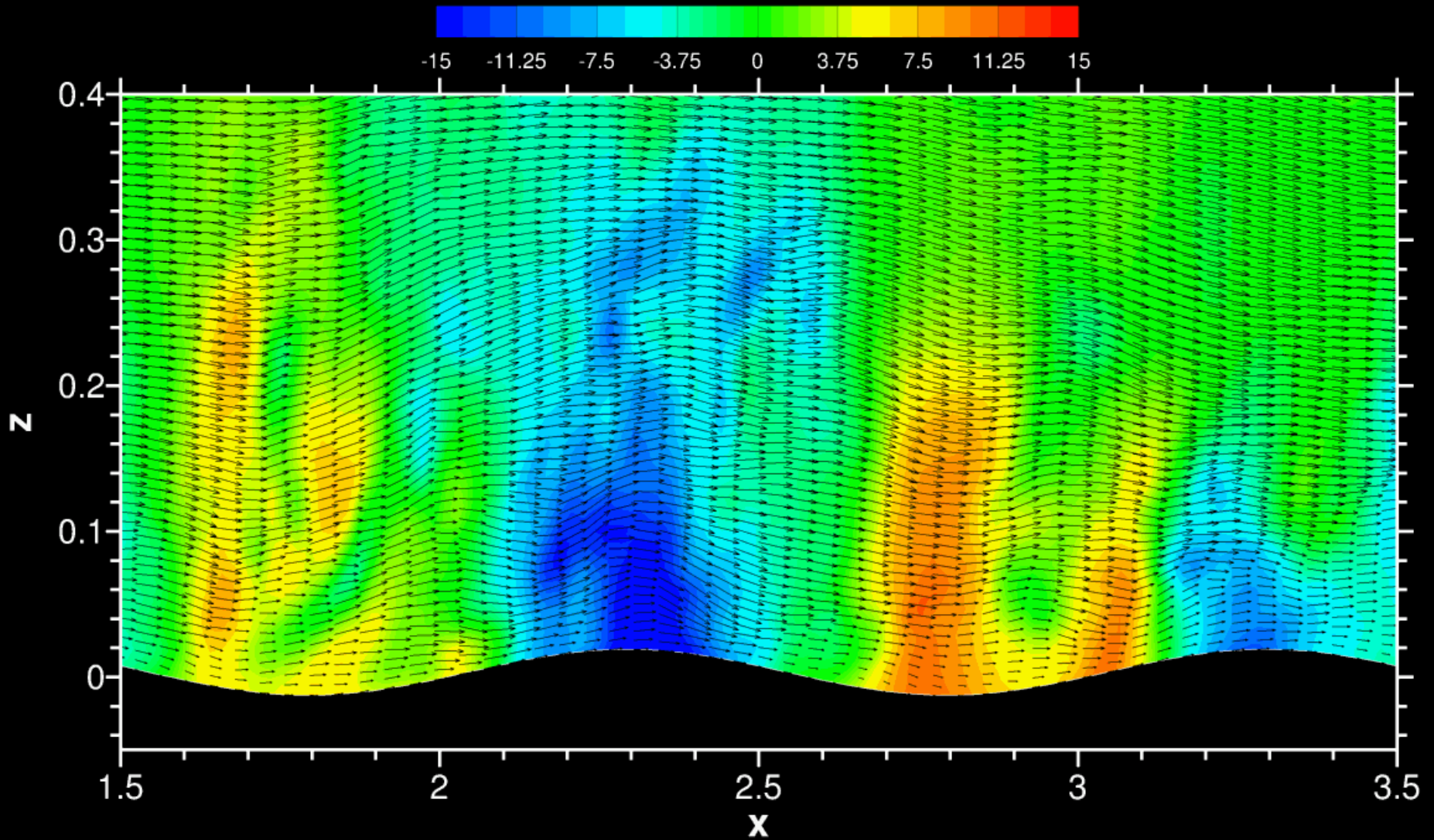
150 s time
averaged
streamlines



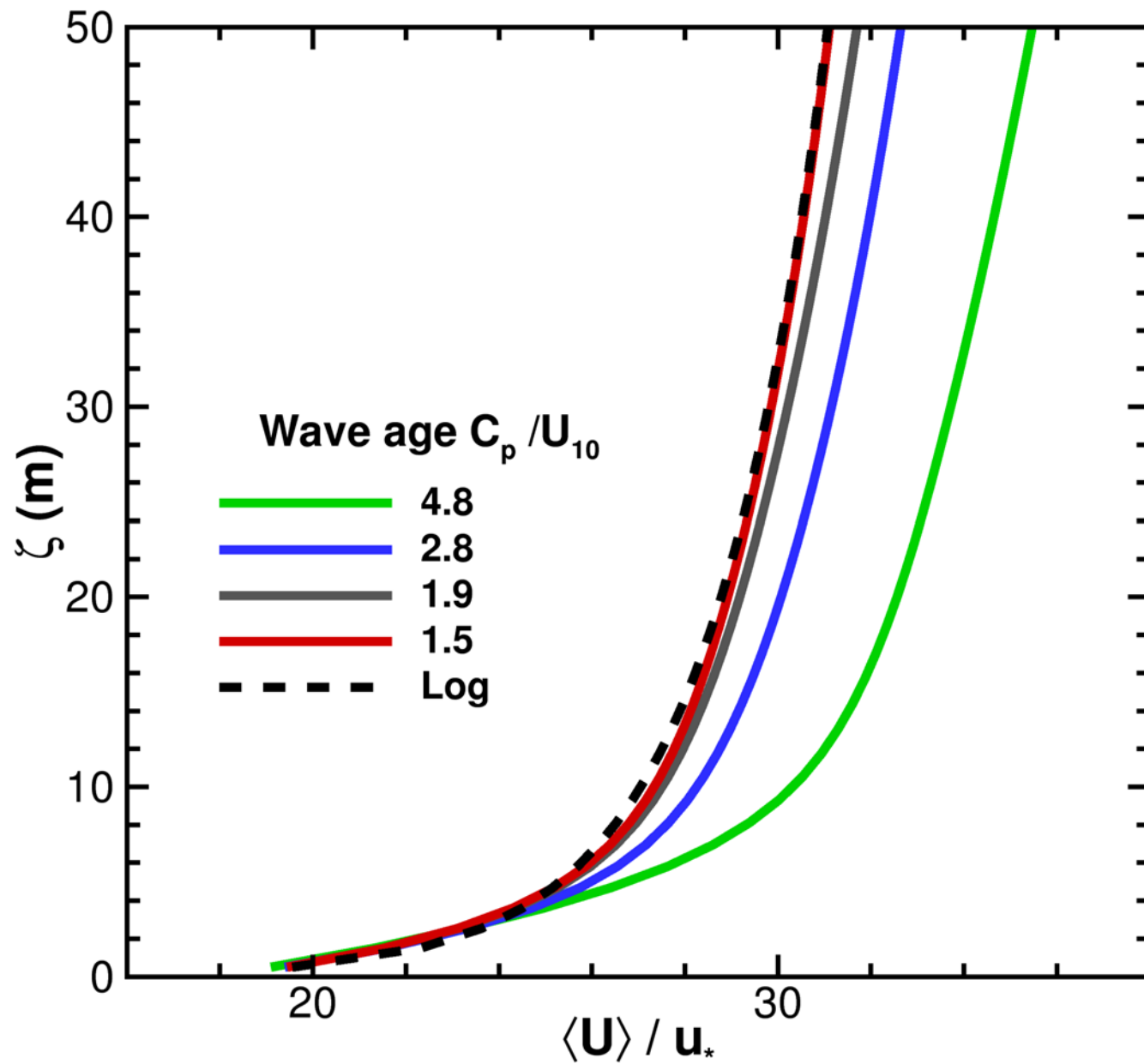
(U,W) Vectors and Pressure over Incipient Breakers



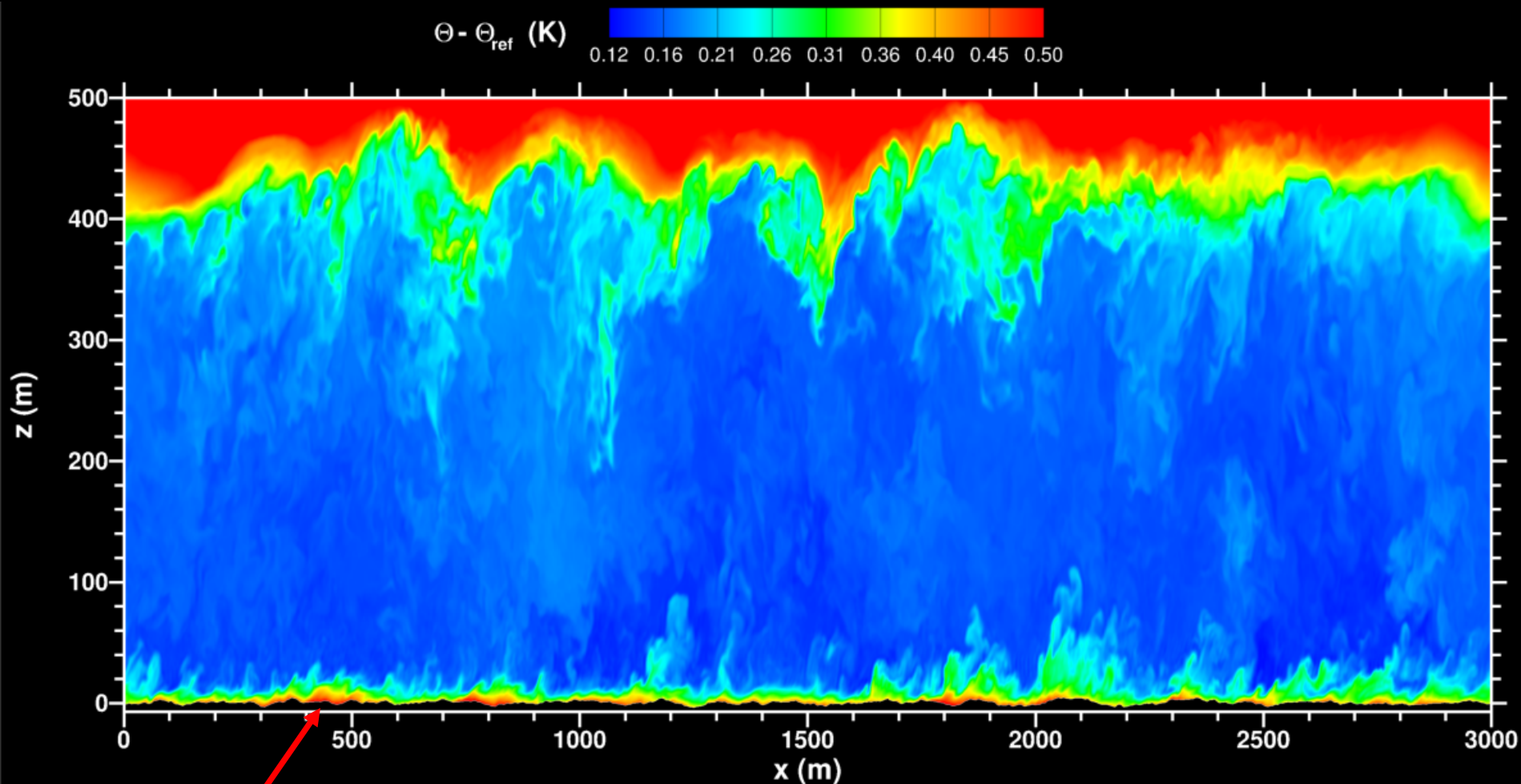
(U,W) Vectors and Pressure over Lowslope Waves, $ak = 0.1$



VERTICAL PROFILE OF MEAN WIND



θ Contours in xz-plane, $U_g = 10$ m/s, $Q^* = 0.01$ K m/s



Wavy boundary

MABL + PHASE RESOLVED WAVES

- LES of a full marine atmospheric boundary layer
 - Rotation, stratification, geostrophic pressure gradients, surface heating (cooling)
- 3D time varying surface wave field
 - Donelan *et al.*(1985) spectrum
 - Measured spectrum (WAMOS vs ATM)?
 - Need z_o for unresolved waves (rough wall boundary condition)
- Funded computational proposal 12 million core hours on “Yellowstone”
 - $1024^2 \times 512$ gridpoints, $(\Delta x, \Delta y, \Delta z) = (1.17, 1.17, 0.5)$ m
 - 4096 or 8192 processors

MABL + PHASE RESOLVED WAVES

- Discussion points:
 - Drag at high winds, viscous and pressure contributions, separation
 - Wave age regime, is wind-wave equilibrium the most interesting, non-equilibrium regimes where waves may play more of a role, or growing waves
 - Estimate of wind input for spectral models
 - Dynamics of wind-wave coupling
 - Comparison with measured data
 - ...

LES MODEL EQUATIONS

FOR PBL FLOW OVER 3D WAVES $h(x, y, t)$

$$\frac{\partial U_i}{\partial \xi_i} = 0 \quad \leftarrow \text{Continuity}$$

$$\frac{\partial}{\partial t} \left(\frac{1}{J} \right) = \frac{\partial}{\partial \zeta} \left(\frac{\partial z}{\partial t} \right) \quad \leftarrow \text{Geometric conservation}$$

$$\frac{\partial}{\partial t} \left(\frac{\bar{u}_i}{J} \right) + \frac{\partial}{\partial \xi_j} [(U_j - \delta_{3j} z_t) \bar{u}_i] = \mathcal{F}_i \quad \leftarrow \text{Momentum}$$

$$\frac{\partial}{\partial t} \left(\frac{\bar{\theta}}{J} \right) + \frac{\partial}{\partial \xi_j} [(U_j - \delta_{3j} z_t) \bar{\theta}] = \mathcal{M} \quad \leftarrow \text{Scalar (temperature)}$$

$$\frac{\partial}{\partial t} \left(\frac{e}{J} \right) + \frac{\partial}{\partial \xi_j} [(U_j - \delta_{3j} z_t) e] = \mathcal{R} \quad \leftarrow \text{SGS energy}$$

$$\frac{\partial}{\partial \xi_i} \left[\frac{1}{J} \frac{\partial \xi_i}{\partial x_j} \frac{\partial \xi_m}{\partial x_j} \frac{\partial p^*}{\partial \xi_m} \right] = \mathcal{S} \quad \leftarrow \text{Pressure equation}$$

*Plus rough wall boundary conditions and
matching to orbital velocity of wavefield*

SCALING OF FLAT LES CODE

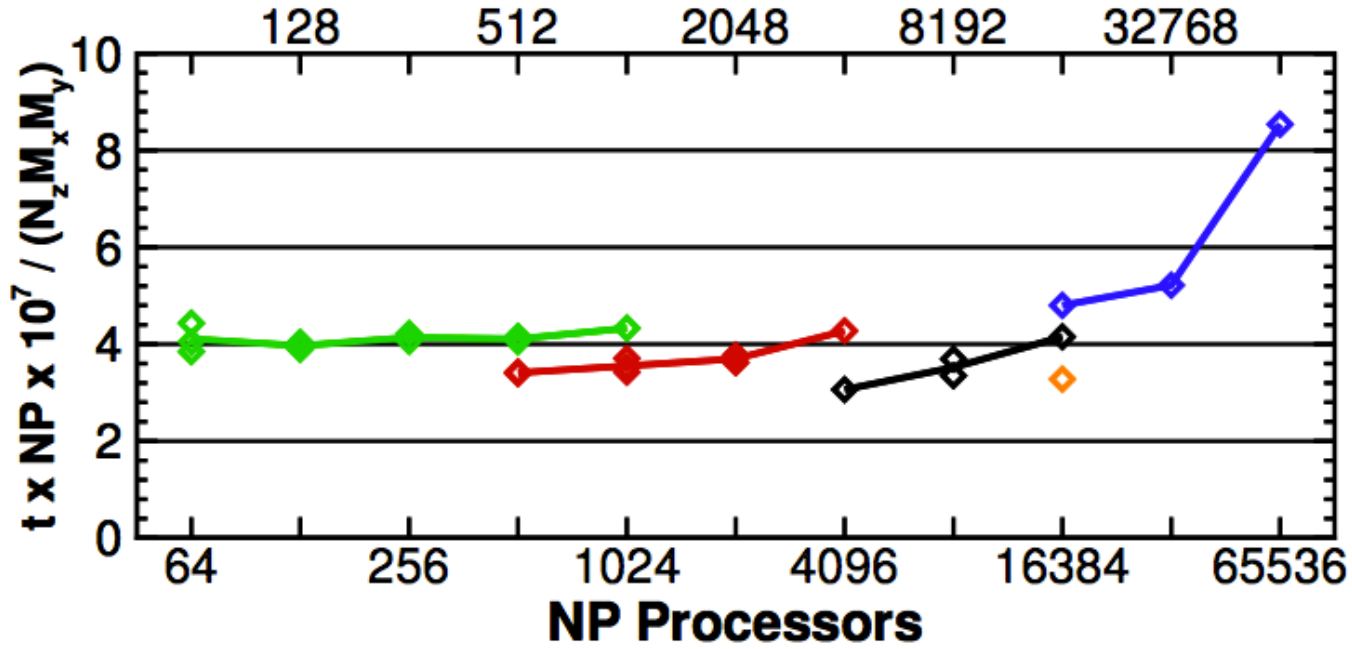


Figure 6: Performance of the NCAR parallel LES code on the NERSC Cray supercomputers, Franklin and Hopper. NP is the total number of processors and the vertical axis is total computational time $t \times NP$ divided by total work. N_z is the number of vertical levels and $M_{x,y}$ is proportional to the FFT work, i.e., $M_{x,y} = N_{x,y} \log N_{x,y}$ with $N_{x,y}$ the number of gridpoints in the x and y directions. Ideal scaling corresponds to a flat line with increasing number of processors. This figure illustrates that the LES code exhibits strong scaling for different combinations of problem size and 2D domain decompositions. a) Green \blacklozenge problem size 512^3 ; b) Red \blacklozenge 1024^3 ; c) Black \blacklozenge 2048^3 ; d) Orange \blacklozenge 3072^3 ; and e) Blue \blacklozenge 3072^3 . Cases [a) - d)] are timing tests performed on Franklin while case e) is a timing test on Hopper. For a given number of total processors NP the symbols are different vertical and horizontal decompositions, i.e., different combinations of (NP_z, NP_{xy}) as depicted in Fig. 5.

**A large eddy simulation model of turbulent atmospheric
boundary layers with moving wavy lower boundaries**

PETER P. SULLIVAN^{1*}, JAMES C. McWILLIAMS²

AND EDWARD G. PATTON¹

¹National Center for Atmospheric Research, Boulder, CO 80307-3000

²Department of Atmospheric and Oceanic Science, UCLA, Los Angeles, CA

**Corresponding author address:* Peter P. Sullivan, MMM Division, NCAR, Boulder, CO 80307-3000.

E-mail: pps@ucar.edu

6 A massively parallel large-eddy simulation (LES) code for atmospheric planetary bound-
7 ary layers (PBLs) above moving and stationary waves is described.

1. Introduction

Large-eddy simulation (LES) is a powerful computational tool for modeling the atmospheric and oceanic planetary boundary layers (PBLs) as simulations permit a systematic study of stratified 3-D turbulence and its coupling with numerous small and large scale processes. Also, a key use of simulation output is as a virtual database to test, design and build simpler 1-D single-column boundary-layer parameterizations for larger scale models (*e.g.*, Large et al. 1994; Ayotte et al. 1995; Beare et al. 2006; Moeng et al. 2010; McWilliams et al. 2012). Given this growing importance of LES in studying boundary-layer dynamics it is then critical to improve its subgrid-scale parameterizations as advocated by Wyngaard (1998, 2004), but also advance LES as a computational method and further its ability to couple atmospheric (or oceanic) turbulence with other processes; the work outlined here focuses on the latter.

In the past, LES of atmospheric boundary-layer flows was primarily restricted to idealized flows with flat stationary upper and lower boundaries owing to limitations in numerical schemes and computer power. Recent algorithmic advances such as development of efficient elliptic solvers, use of non-staggered variable layouts, and refinements to immersed boundary techniques (*e.g.*, Zang et al. 1994; Ferziger and Perić 2002; Mittal and Iaccarino 2005; Lundquist et al. 2010) along with the advent of massively parallel computing architectures have broadened the landscape of turbulent flows within reach of simulations to include atmospheric PBLs with boundary shapes of varying complexity. Boundary-layer flows over hills and moving water waves continue to be usefully modeled with second-order (or RANS) closure technologies despite their restrictive assumptions (*e.g.*, Gent and Taylor 1976; Gent 1977; Chalikov 1978; Li 1995; Gong et al. 1996; Taylor 1998; Belcher and Hunt 1998; Ayotte and Hughes 2004; Chalikov and Rainchik 2011). Past experience has shown that the predictive capabilities of these models are dependent on their turbulence closures, and in many circumstances the models are linearized and thus only applicable to hills and waves of small waveslope ak ; the mean flow remains steady and fully attached under these conditions. The

shortcomings of RANS closure models can in principle be overcome by LES.

The present work follows similar paths as previous LES for turbulent flow over idealized rough stationary hills (*e.g.*, Gong et al. 1996; Brown et al. 2001) but is new in that our scheme couples a turbulence-resolving large-eddy simulation of the atmospheric boundary layer assuming a Boussinesq flow model (Sullivan and Patton 2011) to a three-dimensional time-dependent resolved surface gravity wavefield, *i.e.*, it is applicable to moving wavy boundaries. The numerical scheme is based on a curvilinear coordinate transformation from physical to computational space with a moving grid. A main motivation for constructing and applying this enhanced LES model is to improve our understanding of air-sea interaction dynamics at time and space scales commensurate with the winds, waves, and currents that exchange momentum and scalar fluxes in the lower atmosphere and upper ocean (Sullivan and McWilliams 2010). Process level understanding of the coupling between turbulent winds and waves in equilibrium and non-equilibrium situations is also needed to further develop the next generation of climate, weather, and wave forecast models. For example, coupled wind-wave-ocean models (Chen et al. 2007; Black et al. 2007) are viewed as critical tools for accurate prediction of tropical cyclone intensity and track forecasts, but these modeling systems employ a suite of parameterizations that are largely statistical descriptions of the wind-wave interactions that generate the critical momentum and scalar fluxes. These forecast models do not account for the important phase relationships between winds, waves and currents, *e.g.*, the spatial and temporal intermittency of wave breaking that occurs in moderate to high winds. Also, there is a growing appreciation that wave-current interactions are important for the upper ocean boundary layer at the time-scale of weather events (Sullivan et al. 2012), and for climate predictions (Belcher et al. 2012), and that remotely generated swell and non-equilibrium wave states can play an important and critical role in the surface-layer dynamics of the atmospheric boundary layer (Hanley et al. 2010; Sullivan and McWilliams 2010).

Our work continues past efforts which coupled a turbulent boundary-layer flow with a

single monochromatic wave (Sullivan et al. 2000; Sullivan and McWilliams 2002; Sullivan et al. 2008; Nilsson et al. 2012), but is an advance over these earlier developments. The computational method described here allows for nearly arbitrary 3-D wavefields, *i.e.*, the sea surface elevation $h = h(x, y, t)$, as a surface boundary condition where $h(x, y, t)$ is assumed to be a single-valued function. The spatial scales of the resolved turbulence and waves are $\mathcal{O}(\text{m})$ up to the height of the atmospheric PBL $z_i \sim \mathcal{O}(500 \text{ m})$ or more. To cover this broad range of scales requires a large number of mesh points and significant computational power. High resolution simulations of atmospheric turbulence in the presence of surface waves has the potential to provide new insight into the dynamics of air-sea coupling at small scales. Also, posing LES simulations in the presence of both resolved and SGS waves (Nakayama et al. 2009) touches on similar parameterization issues in large-scale atmospheric models. In the current problem posing, the surface waves are externally imposed based on existing empirical wave spectra. These spectra contain no information about the phase of individual waves or wave groups over a horizontal patch of the ocean surface that might typically be covered by an atmospheric LES model (*e.g.*, an area of say $3 \text{ km} \times 3 \text{ km}$). Theoretical work by Sajjadi et al. (2013) suggests that wave groupiness is potentially important for wave growth; this can be partly accounted for in simulations by using direct observations of the sea surface from field campaigns (Romero and Melville 2010). Although our main computational target is building a turbulence resolving LES model for studying wind-wave interactions, with minor changes the algorithm is easily adapted to atmospheric PBLs with undulating (stationary) landscapes (*e.g.*, Sullivan et al. 2010).

The outline of the paper is as follows: Section 2 is an introduction to the LES equations appropriate for a high-Reynolds number atmospheric PBL and their transformation to time-dependent curvilinear coordinates; Section 3 outlines the numerical method; Sections 4 and 5 describe typical applications; and Section 6 provides a summary of the findings.

2. Governing equations

In the description of the model equations, given below, the following notation is used: $\bar{\mathbf{u}} = (\bar{u}, \bar{v}, \bar{w})$ denote the Cartesian velocity components, $\bar{\theta}$ is virtual potential temperature, \bar{p}^* is the pressure variable normalized by density ρ , and e is the subgrid-scale (SGS) energy. Quantities with an overbar $(\bar{})$ are interpreted as LES spatially filtered variables.

a. Atmospheric LES model equations

The set of spatially filtered LES equations applicable to turbulent flow in the atmospheric boundary layer under the Boussinesq assumption is (*e.g.*, see Moeng 1984; McWilliams et al. 1999)

$$\frac{\partial \bar{u}_i}{\partial x_i} = 0 \quad (1a)$$

$$\frac{\partial \bar{u}_i}{\partial t} = -\frac{\partial \bar{u}_j \bar{u}_i}{\partial x_j} - \frac{\partial \bar{p}^*}{\partial x_j} - 2\epsilon_{ijk}\Omega_j \bar{u}_k + \delta_{i3}\beta(\bar{\theta} - \theta_o) - \frac{\partial \tau_{ij}}{\partial x_j} - \frac{\partial \mathcal{P}}{\partial x_i} \quad (1b)$$

$$\frac{\partial \bar{\theta}}{\partial t} = -\frac{\partial \bar{u}_i \bar{\theta}}{\partial x_i} - \frac{\partial \tau_{i\theta}}{\partial x_i} \quad (1c)$$

$$\frac{\partial e}{\partial t} = -\frac{\partial \bar{u}_i e}{\partial x_i} - \tau_{ij} S_{ij} + \beta \tau_{3\theta} + \frac{\partial}{\partial x_j} \left(2\nu_t \frac{\partial e}{\partial x_j} \right) - \mathcal{E} . \quad (1d)$$

In the above, $\Omega_i = (0, 0, \Omega \sin \Phi)$, with the Earth's (rotation, latitude) denoted (Ω, Φ) , the buoyancy parameter $\beta = g/\theta_o$ where the gravitational acceleration is g , the reference (still air) virtual potential temperature is θ_o , and the large-scale external pressure gradients normalized by density $\partial \mathcal{P} / \partial x_i$ drive the boundary-layer winds. A Boussinesq flow model requires that \bar{p}^* , the pressure variable, be determined from an elliptic Poisson pressure equation to enforce mass conservation; this has significant impact on the solution algorithm (see Section 3d). Ultimately, the SGS momentum and temperature (or scalar) fluxes $(\tau_{ij}, \tau_{i\theta})$, respectively, require modeling in the interior of the flow and at the lower boundary (see Section 3f) to close the system of equations. In the SGS turbulence kinetic energy (TKE) equation (1d), the time evolution of e depends on right-hand-side terms (in order): advection by the resolved field; energy transfer between resolved and SGS motions where the resolved scale

111 strain rate $S_{ij} = 1/2 (\partial \bar{u}_i / \partial x_j + \partial \bar{u}_j / \partial x_i)$; SGS buoyancy flux; Laplacian diffusion with tur-
 112 bulent eddy viscosity ν_t ; and viscous dissipation \mathcal{E} . Molecular diffusion terms are neglected
 113 assuming the molecular Reynolds number is high. A discussion of the modeling of the SGS
 114 fluxes is postponed to Section 2d.

115 *b. Coordinate transformation*

116 We adapt our LES model with a flat bottom to the situation with a three-dimensional
 117 time-dependent boundary shape $h = h(x, y, t)$ by applying a transformation to the physical
 118 space coordinates (x, y, z) that maps them onto computational coordinates (ξ, η, ζ) . The
 119 computational mesh in physical space is surface following, non-orthogonal, and time varying.
 120 Vertical gridlines are held fixed at a particular (x, y) location on the surface but the lines
 121 undergo vertical translation as a function of time t , *i.e.*, vertical gridlines are wave following.
 122 The transformation which obeys these constraints and maps the physical domain to a flat
 123 computational domain $\mathbf{x} \Rightarrow \boldsymbol{\xi}$ is the rule:

$$124 \quad \tau = t \quad , \quad \xi = \xi(x) = x \quad , \quad \eta = \eta(y) = y \quad , \quad \zeta = \zeta(t, x, y, z) \quad . \quad (2)$$

125 The differential metrics $\partial x_i / \partial \xi_j$ and $\partial \xi_i / \partial x_j$, which are needed in formulating the LES model
 126 in curvilinear coordinates, are connected through the mapping transformation. This can be
 127 done for general transformations (*e.g.*, see Anderson et al. 1984, p. 252-253), but here we
 128 take advantage of our simplified terrain following grid (2). This leads to the reduced set of
 129 non-zero metric relationships:

$$130 \quad \zeta_t = -z_t J \quad , \quad \xi_x = \eta_y = 1 \quad ,$$

$$131 \quad \zeta_x = -z_\xi J \quad , \quad \zeta_y = -z_\eta J \quad , \quad \zeta_z = 1/z_\zeta = J \quad (3)$$

132 where J is the Jacobian. The time dependence of the mapping appears in (3) where $\partial z / \partial t =$
 133 z_t is the grid speed, *i.e.*, the vertical velocity of individual gridpoints. Since our specific
 134 interest is flows with wavy lower boundaries we define the rule in (2) that maps physical

space onto flat computational space at any time t according to the prescription

$$z = \zeta + h(x, y, t) \left(1 - \frac{\zeta}{Z_L}\right)^\varpi \quad (4)$$

where Z_L is the top of the computational domain and ϖ controls how rapidly the horizontal gridlines become level surfaces in physical space. Typically we use $\varpi = 3$ which represents an acceptable balance of vertical (squeezing, stretching) of near surface grid cells at the wave (crests, troughs), respectively. Note for $\varpi = 1$, (4) reduces to $\zeta = (z - h)/(1 - h/Z_L)$ which is commonly used to map stationary terrain onto flat computational coordinates (*e.g.*, Henn and Sykes 1999). (4) is a single valued mapping which produces smooth continuous metric derivatives $(\partial\xi_i/\partial x_j, \partial\xi_i/\partial t)$ in the interior of the computational domain depending on the smoothness of the boundary shape derivatives (h_t, h_x, h_y) .

c. LES equations in time-dependent curvilinear coordinates

The transformation of the LES equations to curvilinear coordinates is carried out in straightforward fashion by applying the chain rule for differentiation and making frequent use of the metric identity (*e.g.*, see Anderson et al. 1984, p. 254)

$$\frac{\partial}{\partial\xi_j} \left(\frac{1}{J} \frac{\partial\xi_j}{\partial x_i} \right) = 0. \quad (5)$$

However, to cast the equations in fully conservative form requires care in treating the time derivative. For example, the time derivative of the density transforms as

$$\left. \frac{\partial\rho}{\partial t} \right|_{\mathbf{x}} = J \left[\frac{\partial}{\partial t} \left(\frac{\rho}{J} \right) + \frac{\partial}{\partial\xi_i} \left(\frac{\rho}{J} \frac{\partial\xi_i}{\partial t} \right) \right]_{\boldsymbol{\xi}} = 0, \quad (6)$$

provided the grid movement obeys

$$\frac{\partial}{\partial t} \left(\frac{1}{J} \right) + \frac{\partial}{\partial\xi_i} \left(\frac{1}{J} \frac{\partial\xi_i}{\partial t} \right) = 0. \quad (7)$$

(7) is a re-statement of the so-called geometric (or space) conservation law (GCL) and needs to be satisfied by the numerical discretization in order for the scheme to be conservative

(Thomas and Lombard 1979; Demirdžić and Perić 1990)¹. For our surface following grid the GCL simply reduces to (8b) since $\partial \xi_i / \partial t = (0, 0, -z_t J)$. Section 3c describes how (7) is used to track the motion of the grid.

The complete set of LES equations in computational coordinates under the time-dependent surface-following transformation (2) and (3) is then:

$$\frac{\partial U_i}{\partial \xi_i} = 0 \quad (8a)$$

$$\frac{\partial}{\partial t} \left(\frac{1}{J} \right) - \frac{\partial z_t}{\partial \zeta} = 0 \quad (8b)$$

$$\frac{\partial}{\partial t} \left(\frac{\bar{u}_i}{J} \right) + \frac{\partial}{\partial \xi_j} [(U_j - \delta_{3j} z_t) \bar{u}_i] = \frac{\mathcal{F}_i}{J} \quad (8c)$$

$$\frac{\partial}{\partial t} \left(\frac{\bar{\theta}}{J} \right) + \frac{\partial}{\partial \xi_j} [(U_j - \delta_{3j} z_t) \bar{\theta}] = \frac{\mathcal{M}}{J} \quad (8d)$$

$$\frac{\partial}{\partial t} \left(\frac{e}{J} \right) + \frac{\partial}{\partial \xi_j} [(U_j - \delta_{3j} z_t) e] = \frac{\mathcal{R}}{J} \quad (8e)$$

$$\frac{\partial}{\partial \xi_i} \left[\frac{1}{J} \frac{\partial \xi_i}{\partial x_j} \frac{\partial \xi_m}{\partial x_j} \frac{\partial \bar{p}^*}{\partial \xi_m} \right] = \mathcal{S} \quad (8f)$$

(8a) is the mass conservation (continuity) equation, (8c) is the momentum transport equation, (8d) is the transport equation for potential temperature, (8e) is the subgrid-scale energy transport equation, and (8f) is the pressure Poisson equation. The right hand sides of (8c, 8d, 8e) model physical processes in the atmospheric boundary layer, *viz.*, pressure gradients, Coriolis rotation, divergence of subgrid-scale fluxes, buoyancy, and in the case of the SGS e equation also turbulent diffusion and viscous dissipation. For completeness these terms are

¹Thomas and Lombard (1979, see p. 1032) develop the geometric conservation law using an integral formulation but note that it can equally be derived from the differential form of the governing equations by setting $\rho = 1$ and $u_i = 0$, which is the procedure used here.

174 gathered here:

$$\begin{aligned}
175 \quad \frac{\mathcal{F}_i}{J} = & -\frac{\partial}{\partial \xi_j} \left(\frac{\bar{p}^*}{J} \frac{\partial \xi_j}{\partial x_i} \right) + \delta_{3i} \frac{g}{J \theta_o} (\bar{\theta} - \theta_o) - \frac{\partial}{\partial \xi_j} \left(\frac{\tau_{ik}}{J} \frac{\partial \xi_j}{\partial x_k} \right) \\
176 & - 2\epsilon_{ijk} \Omega_j \frac{\bar{u}_k}{J} - \frac{1}{J} \frac{\partial \mathcal{P}}{\partial x_i} \quad (9a)
\end{aligned}$$

$$177 \quad \frac{\mathcal{M}}{J} = -\frac{\partial}{\partial \xi_j} \left(\frac{\tau_{i\theta}}{J} \frac{\partial \xi_j}{\partial x_i} \right) \quad (9b)$$

$$178 \quad \frac{\mathcal{R}}{J} = -\frac{\tau_{ij} S_{ij}}{J} + \frac{\beta \tau_{3\theta}}{J} + \frac{\partial}{\partial \xi_j} \left(\frac{2\nu_t}{J} \frac{\partial e}{\partial \xi_m} \frac{\partial \xi_m}{\partial x_k} \frac{\partial \xi_j}{\partial x_k} \right) - \frac{\mathcal{E}}{J} \quad (9c)$$

179 Momentum and scalar advection are compactly written in strong flux-conservation form
180 using the volume flux or “contravariant flux” velocity (Rhie and Chow 1983; Zang et al.
181 1994)

$$182 \quad U_i = \frac{\bar{u}_j}{J} \frac{\partial \xi_i}{\partial x_j}, \quad (10)$$

183 where U_i is normal to the surface of constant ξ_i .

184 The time dependence of the grid modifies the LES equations: the Jacobian appears
185 inside the time tendency of each transport equation and as anticipated vertical advection
186 contains a contribution from the vertical grid movement, *i.e.*, the total vertical flux of variable
187 ψ depends on the difference between the contravariant flux velocity and the grid speed
188 $(W - z_t)\psi$. Examination of (8) shows that if the velocity and scalar fields are set to constant
189 values then the left hand sides of (8c-e) reduce to (8b). Hence the numerical method needs
190 to satisfy the reduced form of the GCL discretely in order to prevent artificial sources and
191 sinks from developing in the computational domain, see Section 3c.

192 *d. Parameterization of SGS motions*

193 Formally, the LES equations are obtained by applying a spatial filter, term-by-term, to
194 the full governing equations (*e.g.*, Wyngaard 2004). The filter is assumed to be homogeneous
195 in space and time, and as a result the operation order of differentiation and filtering can
196 be interchanged. For boundary layer flows this assumption is violated and a commutation
197 error occurs near walls (Ghosal and Moin 1995) - but the error is almost always ignored

198 in LES implementations as the inaccuracies in SGS wall modeling are viewed as of greater
 199 importance (Sullivan et al. 2003). The parameterization problem is even more pronounced
 200 with a multi-mode moving lower boundary because of filtered products of fluctuating metric
 201 coefficients and velocity (Chalikov 1978), and extra stress-like terms arise from filtering the
 202 boundary shape (Nakayama et al. 2009). The parameterization problem is then similar in
 203 character to representing SGS topography and canopy turbulence in atmospheric models;
 204 most often their impact is accounted for by a bulk drag parameterization (*e.g.*, Wilson
 205 2002). In the present application, like our flat-bottom LES, the flow is assumed to be
 206 laterally periodic and our wave-following grid transformation results in $x = \xi$ and $y = \eta$.
 207 Thus we adopt the simplest approach and employ the filtering operation and standard SGS
 208 models as in our flat LES code, but account for the varying filter width. The LES equations
 209 are closed using the SGS parameterizations outlined by Deardorff (1972) and analyzed by
 210 Moeng and Wyngaard (1988). Also, the solutions are explicitly filtered, *i.e.*, dealiased, in
 211 $\xi - \eta$ planes at the end of each timestep. The parameterization utilizes an eddy viscosity for
 212 SGS momentum and temperature fluxes, and the classic Lilly-model for viscous dissipation:

$$\begin{aligned}
 & \tau_{ij} = 2\nu_t S_{ij}, \quad \tau_{i\theta} = \nu_h \frac{\partial \bar{\theta}}{\partial x_i}, \quad \mathcal{E} = C_\mathcal{E} \frac{e^{3/2}}{\Delta}. \quad (11)
 \end{aligned}$$

215 The turbulent eddy viscosity $\nu_t = C_k \Delta \sqrt{e}$ and turbulent diffusivity $\nu_h = (1 + 2\ell/\Delta)\nu_t$ evolve
 216 under the action of the transport equation for SGS TKE (8e). The constants $(C_k, C_\mathcal{E}) =$
 217 $(0.1, 0.93)$ and corrections to the stability corrected length scale ℓ are found in Moeng (1984);
 218 Moeng and Wyngaard (1988). The filter length scale Δ accounts for the varying averaging
 219 volume $\Delta^3 = (3/2)^2(\Delta\xi\Delta\eta\Delta\zeta/J)$ with the “3/2” factor accounting for dealiasing. Because
 220 of movement and stretching-squeezing of vertical gridlines Δ varies with position and time.
 221 To reduce the reliance on the SGS model we use fine resolution near the surface (Section
 222 4). Since the large wave motions are fully resolved the total TKE at the surface is often
 223 elevated and dominated by resolved variances further reducing the impact of the SGS model
 224 compared to the situation with flat stationary walls.

e. *Wavefield prescription*

To complete our LES model for the marine atmospheric PBL we need to prescribe the height of the surface wavefield $h(x, y, t)$ in physical space over a typical horizontal domain of the LES; this observational data is generally unknown. In the absence of a full description of the wavefield kinematics and dynamics (*e.g.*, Romero and Melville 2010), we adopt simplifications that allow us to use existing information. We construct time and space maps of $h(x, y, t)$ based on typical empirical fits of measured two-dimensional wave spectra

$$E(k, \phi) = S(k) D(k, \phi) \quad (12)$$

where the amplitude $S(k)$ and directional $D(k, \phi)$ spectra depend on the magnitude of the horizontal wavenumber $k = |\mathbf{k}| = |k_x \hat{\mathbf{i}} + k_y \hat{\mathbf{j}}|$ and wave direction ϕ . Note these spectra are statistical averages that contain no phase information about the wavefield. For the amplitude and directional spectra we choose the well accepted functional forms proposed by Donelan et al. (1985) (see also p. 187 of Komen et al. (1994)) which are applicable to both equilibrium and non-equilibrium wind-wave states. These empirical fits depend on bulk environmental parameters, *viz.*, the reference surface wind speed at 10 m, U_{10} , the phase speed of the peak in the wave height spectrum C_p , their ratio, the wave age C_p/U_{10} , and the mean wave propagation direction $\langle \phi \rangle$. To use these measured spectra, which are expressed in terms of radial frequency ω , in the LES they are transformed into wavenumber space using the linear dispersion relation $k = \omega^2/g$ and properly weighted so that the resulting wavenumber spectra are variance preserving (Phillips 1977, p. 105). In physical space, the rule for constructing the synthetic wavefield $h(x, y, t)$ is as a sum of linear plane waves each with random phase φ

$$h(\mathbf{x}, t) = \sum_{\mathbf{k}} A(k) \exp [i(\mathbf{k} \cdot \mathbf{x} - \omega(k) t + \varphi)] ; \quad (13)$$

the amplitude $A^2(k) = S(k)D(k, \phi)dk_x dk_y$. (13) is implemented in the LES code. Given an initial state $h(x, y, t_o)$, future values of $h(x, y, t)$ are then efficiently obtained by using

250 2-D Fast Fourier Transforms (FFTs). Time and space derivatives of the boundary shape
 251 (h_t, h_x, h_y) , which are needed to construct the moving mesh and the surface boundary con-
 252 ditions, are also computed in straightforward fashion from (13) using FFTs. We anticipate
 253 future LES applications will directly ingest measured maps of $h(x, y, t)$ from airborne im-
 254 agery (*e.g.*, Romero and Melville 2010) or ship mounted X-band radars.

255 *f. Velocity boundary condition*

256 We need to specify boundary conditions on the winds that are consistent with the imposed
 257 surface wavefield. First, both the wind and wave fields are assumed to be spatially periodic
 258 in computational $\xi - \eta$ planes and thus the important boundary conditions that need to be
 259 set are at the bottom and top of the computational domain. At the wave surface, the total
 260 time rate of change of the wave height is

$$261 \quad \frac{dh}{dt} = w_o = h_t + u_o h_x + v_o h_y \quad (14)$$

262 where (u_o, v_o, w_o) are the water motions. Initially we assume these water motions are domi-
 263 nated by the wave orbital velocities (*e.g.*, Lighthill 1978), *i.e.*, there is no net surface drift.
 264 The importance of surface drift for wave breaking is discussed by Banner and Melville (1976);
 265 Banner (1990). The contravariant velocity component normal to the water surface is given
 266 by (10):

$$267 \quad W = u \frac{\zeta_x}{J} + v \frac{\zeta_y}{J} + w . \quad (15)$$

268 Matching (14) and (15) and requiring no flow normal (across) the wavy boundary leads to

$$269 \quad W - h_t = 0 \text{ at } \zeta = 0 . \quad (16)$$

270 (16) effectively implies that spray and bubbles do not pass through the interface. At the
 271 upper boundary of the computational domain the horizontal gridlines are level surfaces in
 272 physical space with $z_\xi = z_\eta = 0$. Then

$$273 \quad W = w = z_t \text{ at } \zeta = Z_L , \quad (17)$$

so that the resolved vertical flux of momentum and scalars is zero across the top boundary. The specification of the surface fluxes appropriate for a high Reynolds number rough wall LES model taking into account the wave motion is described in Section 3f with additional details provided in the Appendix.

3. Numerical method

a. Spatial discretization and variable layout

The LES set of equations (8) is discretized using the well-developed techniques in our flat bottom boundary codes (Moeng 1984; Sullivan et al. 1996). Spatial derivatives in the (ξ, η) computational coordinates are estimated using pseudospectral approximations while centered second-order accurate finite difference approximations are employed for ζ derivatives. In order to be compliant with (8b), the spatial differencing evaluates the advective terms in (8c-e) in flux form as opposed to the rotational form used by Moeng (1984) or skew-symmetric form used by Sullivan et al. (2000).

The variable layout in the computational mesh uses a co-located arrangement for the fundamental solution variables $(\bar{u}_i, \bar{p}^*, \bar{\theta}, e)$ which is advantageous as it results in a compact differencing stencil and is also applicable to meshes with large bends in the coordinate lines (Demirdžić and Perić 1990; Zang et al. 1994). The fundamental difficulty of tightly coupling the velocity and pressure in a co-located mesh is circumvented by locating the contravariant flux velocities at cell faces mimicking the usual arrangement in a staggered mesh. To satisfy (8a), written for contravariant velocities, with our mixed pseudospectral finite-difference scheme results in a novel layout of flow variables with (U, V) also located at cell centers and W naturally located at the upper and lower cell faces as shown in Fig. 1. Furthermore, with a surface-following non-orthogonal grid $(U, V) = (\bar{u}, \bar{v})/J$ are simply scaled versions of their Cartesian counterparts, see (10). Other mesh types and differencing schemes, *e.g.*, orthogonal meshes and finite difference methods, result in different couplings between the

Cartesian and contravariant velocities (*e.g.*, Zang et al. 1994; Sullivan et al. 2000). Lastly, the flow is assumed to be spatially periodic in horizontal $\xi - \eta$ planes so as to be consistent with a Fourier representation.

b. Time advancement

Time integration is a fully explicit third-order Runge-Kutta (RK3) scheme (Spalart et al. 1991; Sullivan et al. 1996, 2008) that uses dynamic time stepping with a fixed Courant-Fredrichs-Lewy (CFL) number and employs a fractional step method to enforce the divergence free condition. As the scheme is completely explicit it is equivalent to the so-called “pressure correction” method of Armfield and Street (2002). The general rule for advancing a cell-centered Cartesian velocity variable to a new time level n over a timestep Δt is

$$\left. \frac{u_i}{J} \right|^n = \left. \frac{\hat{u}_i}{J} \right|^{n-1} - \Delta t \alpha_n \frac{\partial}{\partial \xi_j} \left(\frac{p^*}{J} \frac{\partial \xi_j}{\partial x_i} \right)^n, \quad (18)$$

where the pressure gradient is written in conservative form. The intermediate velocity

$$\left. \frac{\hat{u}_i}{J} \right|^{n-1} = \left. \frac{u_i}{J} \right|^{n-1} + \Delta t \alpha_n \left. \frac{q_i}{J} \right|^{n-1} + \Delta t \beta_n \left. \frac{Q_i}{J} \right|^{n-2} \quad (19)$$

is the discrete sum of the full right hand side Q_i/J from the previous time (or stage) step $(n-2)$ and the partial right hand side q_i/J from the current time $(n-1)$ minus the pressure contributions; (α_n, β_n) are weights associated with the RK3 scheme (see Sullivan et al. 2000). The time integration rule for scalar fields is identical to (18) and (19) in the absence of pressure gradients. In our LES equation set, the divergence free condition is satisfied at every RK3 stage as opposed to the method advocated by Le and Moin (1991) (see also Zheng and Petzold 2006) which projects the velocity onto a divergence free field only at the final stage. The latter scheme is computationally more efficient since it reduces pressure iterations over a full timestep, but both flux and skew-symmetric forms of the advection term in our scalar equations are based on satisfying (8a) at all stages of the RK3 time advancement. Attempts to use the method of Le and Moin (1991) resulted in numerical instabilities.

The geometric conservation law (8b) needs to be satisfied using the same time advancement scheme as for velocity and scalar fields (see (18)). Given an externally imposed wavefield, $h(x, y, t)$ is known at current and future time steps $(n-1, n)$ and we can then construct the distribution of vertical grid points at “ W -points”, *viz.*, $z(x, y)|^{(n-1, n)}$ according to the map (4). Jacobians $J|^{(n-1, n)}$ are then naturally built from the transformation rule (3). Since we choose to specify the grid point locations at future timesteps, we must then find matching grid speeds $z_t(x, y)$ so that (8b) is obeyed discretely. The companion to (18), appropriately inverted, for determining grid speeds is the semi-discrete relationship

$$\left. \frac{\partial z_t}{\partial \zeta} \right|^{n-1} = \frac{1}{\alpha_n \Delta t} \left[\left. \frac{1}{J} \right|^n - \left. \frac{1}{J} \right|^{n-1} - \Delta t \beta_n \left(\frac{\partial z_t}{\partial \zeta} \right)^{n-2} \right]. \quad (20)$$

This first-order equation is integrated vertically from the surface to the top of the domain with the boundary condition $z_t = h_t$ at $\zeta = 0$. We emphasize that the upper boundary of our computational domain is far from the lower surface and the wave-following gridlines in the interior of the domain quickly asymptote to flat level surfaces with increasing ζ . As a result, z_t at a particular $x - y$ gridpoint must vary with distance from the wave surface. This is different than the scheme proposed by Chalikov (1998) where the grid speeds at all ζ are equal to the vertical motion of the wavefield, *i.e.*, z_t is constant with height. The latter scheme also implies that the computational mesh at any ζ , including the upper boundary, mimics the shape of the lower surface which complicates posing upper boundary conditions. There is a subtlety in the implementation of (20). Since our time stepping is explicit the value of z_t diagnosed from (20) is at time level $n-1$ but uses information at time level n . In other words, if the wavefield is imposed, to diagnose the grid speed at time n requires knowledge about the wave shape at a future time $n+1$. The end result is that the grid must be stored at three time levels in the LES code. Information about the wavefield at each RK3 stage is used in two-ways in the grid generation: $h(x, y, t)$ is used to position the grid nodes in the mesh and $h_t(x, y, t)$ is used to determine how rapidly the grid nodes in the mesh move

349 to their new locations.

350 *d. Pressure Poisson equation*

351 The crux of the numerical scheme is the formulation and solution of a pressure Poisson
 352 equation that results in a flow field consistent with our incompressible Boussinesq flow model.
 353 Compared to a flat wall LES code, the solution of the elliptic pressure equation with a wavy
 354 boundary is computationally more expensive, a consequence of the variable coefficients and
 355 mixed spatial derivatives in (8f). As is standard practice we develop a pressure equation by
 356 combining the continuity equation and our time stepping scheme. Substitution of (18) into
 357 (10) leads to the time advance for the contravariant velocity

$$358 \quad U_i|^n = \hat{U}_i|^{n-1} - \frac{\Delta t \psi_n}{J} \frac{\partial \xi_i}{\partial x_j} \frac{\partial \xi_m}{\partial x_j} \frac{\partial \bar{p}^*}{\partial \xi_m} \Big|_I^n \quad (21)$$

359 where now the pressure gradient is expanded in non-conservative form. (21) is designed to
 360 mimic the usual staggered arrangement of flow variables (in our flat LES code) with the
 361 pressure located at a cell center for all three velocity components. The key step in imple-
 362 menting (21) is the construction of the intermediate velocity field \hat{U}_i . We use momentum
 363 interpolation of the Cartesian velocity components to build the right hand side of the con-
 364 travariant flux velocities as proposed by Zang et al. (1994) and Sullivan et al. (2000, 2008).
 365 Essentially, we interpolate \hat{u}_i/J to the same (staggered) locations as U_i and thus

$$366 \quad \hat{U}_i = \frac{\hat{u}_j}{J} \Big|_I \frac{\partial \xi_i}{\partial x_j}, \quad (22)$$

367 where $(\)|_I$ denotes an interpolated value. As mentioned previously, because of the spatial
 368 differencing scheme only $\hat{W}|^{n-1}$, located at the upper and lower cell faces is obtained by
 369 interpolation, see Section 3a. The divergence of (21) leads to the pressure Poisson equation

$$370 \quad \frac{\partial}{\partial \xi_i} \left[\frac{1}{J} \frac{\partial \xi_i}{\partial x_j} \frac{\partial \xi_m}{\partial x_j} \frac{\partial \bar{p}^*}{\partial \xi_m} \right]^n = \frac{1}{\Delta t \psi_n} \frac{\partial \hat{U}_i}{\partial \xi_i} \Big|_I^{n-1}. \quad (23)$$

371 Our strategy for finding the pressure utilizes an iterative method that avoids directly
 372 forming the complicated left hand side of (23). Instead, examination of (18), (21), and (23)

373 suggests the equivalent stationary iteration scheme to find $\overline{p^*}^n$:

$$374 \quad \mathcal{L}(\overline{p^*}^{i+1}) = \mathcal{L}(\overline{p^*}^i) - \frac{1}{\Delta t \alpha_n} \frac{\partial U_k(\overline{p^*}^i)}{\partial \xi_k} \quad (24)$$

375 where the source term is the divergence free condition, superscript i denotes the iteration
376 index, and the linear preconditioning operator

$$377 \quad \mathcal{L}(\overline{p^*}) = \frac{1}{\langle J \rangle} \left(\frac{\partial^2 \overline{p^*}}{\partial \xi^2} + \frac{\partial^2 \overline{p^*}}{\partial \eta^2} \right) + \frac{\partial}{\partial \zeta} \left(\langle J \rangle \frac{\partial \overline{p^*}}{\partial \zeta} \right). \quad (25)$$

378 Note U_k , not \hat{U}_k , appears in the source term of (24). At each iteration we update U_k using
379 the latest $\overline{p^*}^i$ field according to (21) and then compute the new right hand side of (24). \mathcal{L} is
380 designed to be an easily invertible diagonal approximation of the left hand side of (23) with
381 the spatially averaged Jacobian

$$382 \quad \langle J \rangle(\zeta) = \int_{\eta} \int_{\xi} J(\xi, \eta, \zeta) d\xi d\eta. \quad (26)$$

383 Since $\langle J \rangle$ is solely a function of ζ this allows (24) to be solved for $\overline{p^*}^{i+1}$ using standard meth-
384 ods, *viz.*, 2-D Fourier de-composition in $\xi - \eta$ planes followed by tridiagonal matrix inversion
385 in the ζ direction. At convergence $\mathcal{L}(\overline{p^*}^{i+1}) = \mathcal{L}(\overline{p^*}^i)$ and the divergence free condition (8a)
386 is then satisfied at the new time step n . Inversion of (24) for $\overline{p^*}^{i+1}$ is straightforward and can
387 be done in place, but is expensive since its computational steps require global communication
388 in a parallel algorithm (Sullivan and Patton 2011). Solving for pressure in the presence of
389 wavy boundaries increases the overall computational cost of simulations by $\sim 50\%$ compared
390 to simulations with flat lower boundaries where the pressure is solved for directly.

391 *e. Pressure boundary conditions at a wavy boundary*

392 Compatible velocity and pressure boundary conditions are naturally built into the it-
393 eration scheme given by (24). First, the appropriate surface boundary condition on the
394 diagonal preconditioner \mathcal{L} is simply $\partial \overline{p^*} / \partial \zeta = 0$, which is the condition most often used in
395 flat wall LES. The pressure boundary condition used in the source term $\partial U_k(\overline{p^*}) / \partial \xi_k$ of (24)

is exposed by examining the update for (U, V, W) in advancing from $n - 1$ to n given by (21):

$$U|_n = \hat{U}|^{n-1} - \Delta t \alpha_n \left[\frac{1}{J} \frac{\partial \bar{p}^*}{\partial \xi} + \frac{\zeta_x}{J} \frac{\partial \bar{p}^*}{\partial \zeta} \right]^n, \quad (27a)$$

$$V|_n = \hat{V}|^{n-1} - \Delta t \alpha_n \left[\frac{1}{J} \frac{\partial \bar{p}^*}{\partial \eta} + \frac{\zeta_y}{J} \frac{\partial \bar{p}^*}{\partial \zeta} \right]^n, \quad (27b)$$

$$W|_n = \hat{W}|^{n-1} - \Delta t \alpha_n \left[\frac{\zeta_x^2 + \zeta_y^2 + \zeta_z^2}{J} \frac{\partial \bar{p}^*}{\partial \zeta} + \frac{\zeta_x}{J} \frac{\partial \bar{p}^*}{\partial \xi} + \frac{\zeta_y}{J} \frac{\partial \bar{p}^*}{\partial \eta} \right]^n. \quad (27c)$$

In the interior of the computational domain the pressure gradient $\partial \bar{p}^* / \partial \zeta$, which appears in all three equations, is evaluated using standard second-order centered finite-difference formulas, while the pressure gradients $(\partial \bar{p}^* / \partial \xi, \partial \bar{p}^* / \partial \eta)$ are evaluated using pseudospectral differencing. Inspection of (27a,b) shows that to update (U, V) using a centered formula for $\partial \bar{p}^* / \partial \zeta$ at the first level $\zeta = \Delta \zeta / 2$ above the wavy boundary requires the pressure field at $\zeta = 3\Delta \zeta / 2$ and at the ghost point $\zeta = -\Delta \zeta / 2$ below the wavy boundary, assuming equally spaced points in ζ , see Fig. 2. Furthermore at $\zeta = -\Delta \zeta / 2$, U and V , are globally connected to an entire plane of ghost point pressures $\bar{p}^*(x, y, -\Delta \zeta / 2)$ through the gradients $(\partial \bar{p}^* / \partial \xi, \partial \bar{p}^* / \partial \eta)$.

In order to find the proper ghost point pressures we use the W equation, its surface boundary condition, and our iteration scheme. At $\zeta = 0$, (27c) is rearranged to yield

$$\left[\frac{\zeta_x^2 + \zeta_y^2 + \zeta_z^2}{J} \frac{\bar{p}^*(\xi, \eta, \Delta \zeta / 2) - \bar{p}^*(\xi, \eta, -\Delta \zeta / 2)}{\Delta \zeta} \right]^i = \frac{\hat{W} - h_t}{\Delta t \alpha_n} - \left[\frac{\zeta_x}{J} \frac{\partial \bar{p}^*}{\partial \xi} + \frac{\zeta_y}{J} \frac{\partial \bar{p}^*}{\partial \eta} \right]^{i-1} \quad (28)$$

where we impose the boundary condition (16). The superscript i in (28) is again the iteration index, and for clarity we drop the superscripts n and $n - 1$ denoting the time step. At each iteration with a known field $\bar{p}^*(\xi, \eta, \Delta \zeta / 2)^i$, (28) is rearranged to solve for the ghost point pressure $\bar{p}^*(\xi, \eta, -\Delta \zeta / 2)^i$ with the right hand side (centered on $\zeta = 0$) lagged from the previous iteration. Subsequently, (27a,b) are updated at all interior nodes and a pressure iteration is completed by sweeping through (24) with a new right hand side. $\hat{W}(\zeta = 0)$, which appears in (28), is constant during pressure iterations and is obtained from interior node interpolations.

Preliminary tests indicated that extrapolation of the interior pressures to $\zeta = 0$ or use of $\partial \bar{p}^* / \partial \zeta = 0$ at the wave surface resulted in spoiled solutions with oscillations in the pressure and vertical velocity fields propagating from the wavy surface into the interior of the computational domain. The magnitude of the oscillations increased with finer resolution and with the number of wave modes in the boundary shape. The use of (28) permits us to impose the maximum number of wave modes in $h(x, y, t)$ allowed by the horizontal grid resolution in our pseudospectral differencing scheme, *i.e.*, $2/3(NX, NY)$ where (NX, NY) are the number of gridpoints in the (ξ, η) directions, respectively. For simulations with flat boundaries the updates for (U, V) are independent of the ghost point pressures, while in a fully coupled air-water simulation the surface pressure would be consistently determined by matching with the water motions.

f. Surface fluxes

In high winds, the ocean surface is assumed to be in a fully rough regime with negligible contributions from the thin molecular viscous sublayer (Donelan 1998). This assumption however needs to be re-considered at low winds with very small scale waves (*e.g.*, Harris et al. 1996; Meirink and Makin 2001) where the roughness Reynolds number can be in a smooth or transitional regime. Here, we follow the approach of second-order closure modeling for turbulent flow over hills and waves and assume the water surface is fully rough so that the surface fluxes of momentum and scalars can be represented in terms of standard law-of-the-wall relationships (*e.g.*, Gent and Taylor 1976; Makin et al. 1995; Belcher and Hunt 1998). This approach is less certain in LES modeling where surface undulations (or waves) are partially resolved, *i.e.*, the velocity and pressure fields induced by the large energetic components of the wavefield are resolved and the smaller scale less energetic waves are unresolved (*i.e.*, subgrid-scale). How to parameterize surface fluxes in a mixed resolved-SGS regime for stationary waves is a current research topic (*e.g.*, Nakayama et al. 2004; Anderson and Meneveau 2010), and is unexplored for moving waves. To make progress, we adopt a

simplified approach that applies the bulk aerodynamic formulas point-by-point along the wave surface in a local Cartesian coordinate system:

$$\tau_o = -u_*^2 = -C_d |\mathbf{u}_s|^2 \quad (29a)$$

$$Q_* = -C_h |\mathbf{u}_s| (\theta_s - \theta_{surf}) . \quad (29b)$$

where (C_d, C_h) are bulk transfer coefficients for momentum and temperature, u_* is the friction velocity, θ_s is the potential temperature at the first grid point $\zeta = \Delta\zeta/2$ off the surface, θ_{surf} is the temperature of the water surface, and Q_* is the surface temperature (heat) flux. \mathbf{u}_s is the vector difference between the surface following winds at $\zeta = \Delta\zeta/2$ and the water motions at $\zeta = 0$. The total stress τ_o in surface following coordinates is converted into a surface flux matrix in the LES Cartesian frame of reference using the transformation:

$$\tau_{ij} \equiv \boldsymbol{\tau} = \tau_o b_{ij} , \quad (30)$$

where the transformation matrix b_{ij} varies with each surface grid point. The lengthy details of defining the local wave-fitted Cartesian coordinate system, computing (C_d, C_h) , and generating b_{ij} are confined to the Appendix.

4. Simulations with wavy lower boundaries

To demonstrate the capabilities of our LES method, a series of simulations with varying geostrophic wind $U_g = (5, 10, 20, 25)$ m s⁻¹ are carried out for a weakly unstable marine PBL in a domain $(X_L, Y_L, Z_L) = (3000, 3000, 800)$ m using $(N_x, N_y, N_z) = (1024, 1024, 512)$ gridpoints; thus the horizontal grid spacing $\Delta x = \Delta y = 2.93$ m with the first vertical level nominally located 1 m above the water surface. A slice of the computational mesh is given in figure 5. The initial temperature sounding $\bar{\theta} = 300$ K up to the inversion height $z_i = 400$ m, beyond this height $\bar{\theta}$ increases linearly at 3×10^{-3} K m⁻¹. The surface heating $Q_* = 0.03$ K m s⁻¹, the surface roughness $z_o = 0.0002$ m, and the Coriolis parameter $f = 10^{-4}$ s⁻¹. The wavefield is built, as discussed in Section e, based on a wind speed of 15 m s⁻¹ and the

phase speed of the peak in the spectrum $C_p \sim 18 \text{ m s}^{-1}$. Thus the suite of simulations allows us to examine a wide variation of wave age from swell dominated to wind-wave equilibrium. Table 1 lists bulk properties of the simulations, *viz.*, the geostrophic wind, wave age, and friction velocity u_* . U_{10} is the reference wind speed at a height of 10 m. The simulations are run for more than 50,000 timesteps using restart volumes with fully developed turbulence. The iteration count in the pressure Poisson solver set to 30 and the calculations run on 2048 computational cores.

The wave height field varies with space and time as indicated by (13), see Fig. 3. Closer inspection of the image shows a preference towards long crested waves, *i.e.*, waves with aspect ratio long in the direction perpendicular to the winds. Horizontal spectra of the wave height variance in the x and y directions are given in Fig. 4. These are obtained from the Donelan et al. (1985) empirical fits and converted into wavenumber space using the linear dispersion relation. The spectra show that there is a preference for generating long crested waves in the direction perpendicular to the mean wind direction at low wavenumber. The spectra exhibit a power law of k^{-xxx} at small scales (high wavenumbers).

5. Results

Previous field observations (Grachev and Fairall 2001; Smedman et al. 1999), turbulence closure modeling (Hanley and Belcher 2008; Makin 2008), and our own idealized LES (Sullivan et al. 2008) all show that fast moving swell can induce marked changes in the atmospheric surface layer winds, *viz.*, an upward momentum flux from the ocean to the atmosphere, a low-level wind maximum, and departures from law-of-the-wall scaling. The preliminary LES computations performed here over a more realistic sea surface are in good qualitative agreement with the previous studies but suggest the impact of swell on the surface layer winds is sensitive to the content of the wave spectrum.

One of the surprising results from the present simulations is the significant impact of swell

496 on the coherence and magnitude of the near-surface pressure fluctuations. This is illustrated
 497 in figure 6 where we compare p'/ρ for two levels of wind forcing $U_g = (5, 20) \text{ m s}^{-1}$, *i.e.*,
 498 a low-wind situation with swell and a high wind case approaching wind-wave equilibrium.
 499 The difference in the pressure signals is striking and even more remarkable in animations
 500 of the pressure field. In the low-wind swell case there is a very strong correlation between
 501 $p'/\rho < 0$ and wave crests and similarly between $p'/\rho > 0$ and wave troughs that extends
 502 over the depth of the surface layer. Inspection of the flow visualization and animations
 503 reveals that the strong correlation persists across the range of resolved waves, *i.e.*, both
 504 large and small scale waves appear to induce a similar pressure pattern. The coherence of
 505 the wave induced pressure field can extend to 20 m or more depending on the amplitude of
 506 the underlying wave. Also, the pressure signatures propagate at the speed of the wavefield,
 507 additional evidence that the signals are generated by surface waves and not atmospheric
 508 processes. These are clear signatures of “wave pumping” by the surface wavefield on the
 509 atmosphere. The amplitude of the wave spectrum (and hence the level of wave forcing) is
 510 held constant in our simulations but the magnitude of the turbulence, as measured by u_* ,
 511 increases substantially with increasing wind speed. The structure of the near surface pressure
 512 field is a result of these two competing effects. At low winds coherent pressure signals are
 513 generated by the wave motions when the turbulence is weak but this coherence is destroyed
 514 by strong turbulence at higher winds.

515 Figure 7 shows that the impact of wave age also appears in the vertical velocity fields.
 516 In the low-wind swell regime we observe large-amplitude large-scale fluctuations in w' . At
 517 higher winds the spatial coherence of w' is destroyed by strong turbulence. Note each panel
 518 in figure 7 is sampled at the sample height above the wavefield. Also, the fields are made
 519 dimensionless by friction velocity u_* which further illustrates the strong impact of the wave
 520 motions on the winds in the surface layer.

521 In figure 8 we compare vertical profiles of the mean wind speed and turbulence variances
 522 for the different simulations. These statistics are computed by averaging in computational

coordinates, *i.e.*, across horizontal planes at constant vertical height ζ . Similar to Sullivan et al. (2008) we find that the wind speed and turbulence variances depend on wave age. At high winds as the simulations approach wind-wave equilibrium, the non-dimensional wind profile $\langle U \rangle / u_*$ smoothly approaches the variation predicted by law-of-the-wall. Significant differences are observed for the cases dominated by swell: the surface layer winds are accelerated compared to rough wall scaling. As suggested by the flow visualization, the turbulence variances respond to the wave motion in dramatic ways. The horizontal and vertical variances are significantly enhanced by the motion of the wave surface in the low-wind cases. Even though the turbulence is relatively weak the turbulence variances are large near the wave surface due to wave pumping.

6. Summary

A large-eddy simulation (LES) model for the marine atmospheric planetary boundary layer (PBL) is coupled to a 3D time-dependent surface gravity wavefield. A coordinate transform from physical to computational space is used that accounts for vertical movement of the mesh in physical space. We use the geometric conservation law (GCL) (Thomas and Lombard 1979) to solve for the grid speeds that enter into the advection of momentum and scalars. The algorithm is used to carry out a series of simulations over a broadband moving wavefield that conforms to a Pierson-Moskowitz wave spectrum. The wave age $C_p/U_{10} = [1.5, 4.8]$ varies from near wind-wave equilibrium to a low-wind swell dominated regime. In the low wind cases we find features similar to previous observational and modeling investigations: the surface layer winds show clear departures from rough wall law-of-the-wall scaling. The coherence and magnitude of the pressure field p'/ρ depends critically on the motion of the underlying wavefield and the turbulence level.

Acknowledgments.

We thank the anonymous reviewers for their comments and suggestions that improved this work. PPS and JCM were supported by the Physical Oceanography Program through the Office of Naval Research (ONR) Departmental Research Initiative, High Resolution Air-Sea Interaction (HiRES). PPS and EGP are also supported by the National Science Foundation through the National Center for Atmospheric Research. This research used computer resources provided by NCAR and the Department of Defense High Performance Computing Modernization Program. Any opinions, findings, and conclusions or recommendations expressed in this publication are those of the author(s) and do not necessarily reflect the views of the National Science Foundation.

APPENDIX

Appendix Computation of surface fluxes

At each (x, y) or (ξ, η) surface point, surface fluxes are computed in a local wave-fitted Cartesian coordinate system \mathbf{x}' assuming law-of-the-wall formulas. These fluxes are then converted into the LES Cartesian system \mathbf{x} so that they can be used as SGS surface fluxes in (9). The sequence of the steps is:

1. Build the base vectors parallel, perpendicular, and normal to the wave surface that define the local \mathbf{x}' coordinate system. Compute the surface wind
2. Build the matrix of direction cosines \mathbf{a} that transforms $\mathbf{x}' \iff \mathbf{x}$
3. Build the surface momentum and temperature fluxes in the \mathbf{x}' system based on Monin-Obukhov (MO) similarity theory
4. Transform the momentum fluxes in the \mathbf{x}' coordinate system into the LES coordinate system \mathbf{x}

a. Surface definition and surface wind

Given the (x, y, z) surface coordinates the vectors aligned with the surface (ξ, η) gridlines for $\zeta = 0$ are

$$\mathbf{t}_1 = \mathbf{i} + \frac{\Delta z}{\Delta x} \mathbf{k} \quad (\text{constant } \eta), \quad \mathbf{t}_2 = \mathbf{j} + \frac{\Delta z}{\Delta y} \mathbf{k} \quad (\text{constant } \xi), \quad (\text{A1})$$

where $(\Delta x, \Delta y, \Delta z)$ are displacements taken along the surface gridlines. The surface normal

$$\mathbf{n} = \mathbf{t}_1 \times \mathbf{t}_2, \quad (\text{A2})$$

and the unit base vectors ($\hat{\mathbf{t}}_1 = \mathbf{t}_1/|\mathbf{t}_1|$, $\hat{\mathbf{t}}_2 = \mathbf{t}_2/|\mathbf{t}_2|$, $\hat{\mathbf{n}} = \mathbf{n}/|\mathbf{n}|$) are then easily computed.

In the simulation code, the components of the Cartesian wind vector at the first grid point off the surface are $\mathbf{u} = u\mathbf{i} + v\mathbf{j} + w\mathbf{k}$, and in the situation of moving water waves the velocity components of the surface are $\mathbf{u}_o = u_o\mathbf{i} + v_o\mathbf{j} + w_o\mathbf{k}$. Following standard practice, we assume that the surface stress acts in a direction parallel to the surface and depends on the *relative* motion between the wind and water (*e.g.*, Li 1995). The relative wind vector $\mathbf{u}_s = \delta\mathbf{u} = \mathbf{u} - \mathbf{u}_o$ is projected onto the surface, *i.e.*,

$$\mathbf{u}_s = (\delta\mathbf{u} \cdot \mathbf{t}_1)\mathbf{t}_1 + (\delta\mathbf{u} \cdot \mathbf{t}_2)\mathbf{t}_2 = u_s^{(1)}\mathbf{t}_1 + u_s^{(2)}\mathbf{t}_2, \quad (\text{A3})$$

where $(u_s^{(1)}, u_s^{(2)})$ are the relative surface wind components aligned with the vectors $(\mathbf{t}_1, \mathbf{t}_2)$, respectively.

b. Bulk transfer coefficients C_d and C_h

To compute the magnitude of the total surface stress τ_o we invoke MO similarity theory and the bulk aerodynamic formulas for momentum and heat:

$$\tau_o = -u_*^2 = -C_d|\mathbf{u}_s|^2 \quad (\text{A4a})$$

$$Q_* = -C_h|\mathbf{u}_s|(\theta_s - \theta_{surf}), \quad (\text{A4b})$$

where (C_d, C_h) are bulk transfer coefficients, u_* is the friction velocity, θ_s is the potential temperature at the first grid point off the surface, *i.e.*, at the same location as $|\mathbf{u}_s|$, θ_{surf} is the temperature of the surface, and Q_* is the surface heat (temperature) flux. Under the assumption that the surface shear stress points in the direction of the unit base vector $\hat{\mathbf{u}}_s$:

$$\boldsymbol{\tau}' = \tau_o\hat{\mathbf{u}}_s = -C_d|\mathbf{u}_s|^2 \left(\frac{u_s^{(1)}}{|\mathbf{u}_s|}\hat{\mathbf{t}}_1 + \frac{u_s^{(2)}}{|\mathbf{u}_s|}\hat{\mathbf{t}}_2 \right), \quad (\text{A5})$$

or

$$\boldsymbol{\tau}' = -C_d|\mathbf{u}_s| \left(u_s^{(1)}\hat{\mathbf{t}}_1 + u_s^{(2)}\hat{\mathbf{t}}_2 \right). \quad (\text{A6})$$

For a flat surface with $\Delta z = 0$ then (A6) becomes

$$\boldsymbol{\tau}' = -C_d|\mathbf{u}_s| \left(u_s^{(1)}\mathbf{i} + u_s^{(2)}\mathbf{j} \right) \quad (\text{A7})$$

which is the variation in flat LES codes. In the \mathbf{x}' coordinate system, the surface momentum flux $\boldsymbol{\tau}'$ is a symmetric matrix with two non-zero components

$$\tau'_{ij} = \tau_o \begin{bmatrix} 0 & 0 & 1 \\ 0 & 0 & 0 \\ 1 & 0 & 0 \end{bmatrix}. \quad (\text{A8})$$

Rules need to be formulated for the transfer coefficients. In the absence of detailed information we simply use MO similarity arguments as for a flat surface. Given the expressions

$$|\mathbf{u}_s| = \frac{u_*}{\kappa} \left[\ln \left(\frac{z_s}{z_o} \right) + \psi_m \left(\frac{z_s}{L} \right) \right] \quad (\text{A9a})$$

$$\theta_s - \theta_{surf} = -\frac{Q_*}{u_* \kappa} \left[\ln \left(\frac{z_s}{z_o} \right) + \psi_h \left(\frac{z_s}{L} \right) \right] \quad (\text{A9b})$$

where the von Kármán constant is κ , the surface roughness is z_o , the normal distance from the surface to the first gridpoint is z_s , and the MO length is L . The functions ψ_m, ψ_h are the traditional MO similarity functions (*e.g.*, Large et al. 1994). We use iteration to solve (A9a, A9b) for u_* and θ_{surf} when Q_* is given.

c. Matrix of direction cosines $[\mathbf{a}]$

The matrix of direction cosines connects the \mathbf{x}' and \mathbf{x} coordinate systems:

$$\mathbf{x}' = \mathbf{a} \mathbf{x} \quad \text{where} \quad \mathbf{a} = [\hat{\mathbf{u}}_s, \hat{\mathbf{r}}, \hat{\mathbf{n}}]. \quad (\text{A10})$$

$(\hat{\mathbf{u}}_s, \hat{\mathbf{r}}, \hat{\mathbf{n}})$ are unit base vectors with $\hat{\mathbf{r}} = \hat{\mathbf{n}} \times \hat{\mathbf{u}}_s$. Transformation of stress between two Cartesian coordinate systems obeys the transformation rules for a second-order tensor (*e.g.*, see p. 147, Goldstein 1950)

$$\boldsymbol{\tau}' = \mathbf{a} \boldsymbol{\tau} \mathbf{a}^T \quad \text{or} \quad \mathbf{a}^T \boldsymbol{\tau}' \mathbf{a} = \boldsymbol{\tau}. \quad (\text{A11})$$

Expanding the matrix multiplications in (A11) and utilizing the properties of a_{ij} the transformation of stress from the local wave-fitted Cartesian coordinate system to the LES coordinate

621 system is

$$622 \quad \boldsymbol{\tau} = \tau_o b_{ij} = \tau_o \begin{bmatrix} 2a_{11}a_{31} & a_{11}a_{32} + a_{31}a_{12} & a_{11}a_{33} + a_{13}a_{31} \\ a_{12}a_{31} + a_{11}a_{32} & 2a_{12}a_{32} & a_{12}a_{33} + a_{13}a_{32} \\ a_{11}a_{33} + a_{13}a_{31} & a_{13}a_{32} + a_{12}a_{33} & 2a_{13}a_{33} \end{bmatrix}. \quad (\text{A12})$$

623 The right hand side of (A12) is a full symmetric matrix. If the surface is 2-D, *i.e.*, no
624 variation in y (or η), the direction cosine of the \mathbf{j} -component of the surface normal vector
625 $a_{32} = 0$. Then (A12) reduces to a similar transformation matrix as described by Henn and
626 Sykes (1999) (see their equation (16)).

REFERENCES

- 629 Anderson, D. A., J. C. Tannehill, and R. H. Pletcher, 1984: *Computational Fluid Mechanics*
630 *and Heat Transfer*. McGraw-Hill, 599 pp.
- 631 Anderson, W. and C. Meneveau, 2010: A large-eddy simulation model for boundary-layer
632 flow over surfaces with horizontally resolved and vertically unresolved roughness elements.
633 *Boundary-Layer Meteorol.*, **137**, 397–415.
- 634 Armfield, S. and R. Street, 2002: An analysis and comparison of the time accuracy of
635 fractional-step methods for the Navier-Stokes equations on staggered grids. *International*
636 *Journal for Numerical Methods In Fluids*, **38**, 255–282.
- 637 Ayotte, K., et al., 1995: An evaluation of neutral and convective planetary boundary layer
638 parameterizations relative to large eddy simulation. *Boundary-Layer Meteorol.*, **79**, 131–
639 175.
- 640 Ayotte, K. W. and D. E. Hughes, 2004: Observations of boundary-layer wind-tunnel flow
641 over isolated ridges of varying steepness and roughness. *Boundary-Layer Meteorol.*, **112**,
642 525–556.
- 643 Banner, M. L., 1990: The influence of wave breaking on the surface pressure distribution in
644 wind-wave interaction. *J. Fluid Mech.*, **211**, 463–495.
- 645 Banner, M. L. and W. K. Melville, 1976: On the separation of airflow over water waves. *J.*
646 *Fluid Mech.*, **77**, 825–842.
- 647 Beare, R. J., et al., 2006: An intercomparison of large-eddy simulations of the stable bound-
648 ary layer. *Boundary-Layer Meteorol.*, **118**, 242–272.

649 Belcher, S. E. and J. C. R. Hunt, 1998: Turbulent flow over hills and waves. *Annual Review*
650 *of Fluid Mechanics*, **30**, 507–538.

651 Belcher, S. E., et al., 2012: A global perspective on Langmuir turbulence in the ocean surface
652 boundary layer. *Geophys. Res. Lett.*, **39**, L18605.

653 Black, P., et al., 2007: Air-sea exchange in hurricanes: Synthesis of observations from the
654 Coupled Boundary Layers Air-Sea Transfer experiment. *Bull. Amer. Meteorol. Soc.*, **88**,
655 357–374.

656 Brown, A. R., J. M. Hobson, and N. Wood, 2001: Large eddy simulation of neutral turbulent
657 flow over rough sinusoidal ridges. *Boundary-Layer Meteorol.*, **98**, 411–441.

658 Chalikov, D., 1998: Interactive modeling of surface waves and boundary layer. *Ocean Wave*
659 *Measurement and Analysis: Proceedings of the Third International Symposium Waves 97*,
660 B. L. Edge, J. M. Hemsley, and Y. Goda, Eds., American Society of Civil Engineers,
661 1525–1539.

662 Chalikov, D. and S. Rainchik, 2011: Coupled numerical modelling of winds and waves and
663 the theory of the wave boundary layer. *Boundary-Layer Meteorol.*, **138**, 1–41.

664 Chalikov, D. V., 1978: The numerical simulation of wind-wave interaction. *J. Fluid Mech.*,
665 **87**, 561–582.

666 Chen, S. S., J. F. Price, W. Zhao, M. A. Donelan, and E. J. Walsh, 2007: The CBLAST-
667 Hurricane program and the next-generation fully coupled atmosphere-wave-ocean models
668 for hurricane research and prediction. *Bull. Amer. Meteorol. Soc.*, **88**, 311–317.

669 Deardorff, J. W., 1972: Three-dimensional numerical modeling of the planetary boundary
670 layer. *Workshop on Micrometeorology*, D. A. Haugen, Ed., American Meteorological Soci-
671 ety, 271–311.

Demirdžić, I. and M. Perić, 1990: Finite volume method for prediction of fluid flow in arbitrarily shaped domains with moving boundaries. *International Journal for Numerical Methods in Fluids*, **10**, 771–790.

Donelan, M. A., 1998: Air-water exchange processes. *Physical Processes in Lakes and Oceans*, J. Imberger, Ed., American Geophysical Union, Coastal and Estuarine Studies, Vol. 54, 19–36.

Donelan, M. A., J. Hamilton, and W. H. Hui, 1985: Directional spectra of wind-generated waves. *Phil. Trans. Roy. Soc. London, Ser. A*, **315**, 509–562.

Ferziger, J. H. and M. Perić, 2002: *Computational Methods for Fluid Dynamics*. 3d ed., Springer-Verlag.

Gent, P. R., 1977: A numerical model of the air flow above water waves. Part 2. *J. Fluid Mech.*, **82**, 349–369.

Gent, P. R. and P. A. Taylor, 1976: A numerical model of the air flow above water waves. *J. Fluid Mech.*, **77**, 105–128.

Ghosal, S. and P. Moin, 1995: The basic equations for the large eddy simulation of turbulent flows in complex geometry. *J. Comp. Phys.*, **118**, 24–37.

Goldstein, H., 1950: *Classical Mechanics*. Addison-Wesley Publishing Company, 399 pp.

Gong, W., P. A. Taylor, and A. Dörnbrack, 1996: Turbulent boundary-layer flow over fixed aerodynamically rough two-dimensional sinusoidal waves. *J. Fluid Mech.*, **312**, 1–37.

Grachev, A. A. and C. W. Fairall, 2001: Upward momentum transfer in the marine boundary layer. *J. Phys. Oceanogr.*, **31**, 1698–1711.

Hanley, K. E. and S. E. Belcher, 2008: Wave-Driven wind jets in the marine atmospheric boundary layer. *J. Atmos. Sci.*, **65**, 2646–2660.

695 Hanley, K. E., S. E. Belcher, and P. P. Sullivan, 2010: A global climatology of wind-wave
696 interaction. *J. Phys. Oceanogr.*, **40**, 1263–1282.

697 Harris, J. A., S. E. Belcher, and R. L. Street, 1996: Linear dynamics of wind waves in
698 coupled turbulent air-water flow. Part 2. Numerical model. *J. Fluid Mech.*, **308**, 219–254.

699 Henn, D. S. and R. I. Sykes, 1999: Large-eddy simulations of flow over wavy surfaces. *J.*
700 *Fluid Mech.*, **383**, 75–112.

701 Komen, G. J., L. Cavaleri, M. Donelan, K. Hasselmann, S. Hasselmann, and P. A. E. M.
702 Janssen, 1994: *Dynamics and Modelling of Ocean Waves*. Cambridge University Press,
703 532 pp.

704 Large, W. G., J. C. McWilliams, and S. C. Doney, 1994: Oceanic vertical mixing: A review
705 and a model with a nonlocal boundary layer parameterization. *Rev. Geophys.*, **32**, 363–403.

706 Le, H. and P. Moin, 1991: An improvement of fractional step methods for the incompressible
707 Navier-Stokes equations. *J. Comp. Phys.*, **92**, 369–379.

708 Li, P. Y., 1995: A numerical study on energy transfer between turbulent air flow and finite
709 amplitude water waves. Ph.D. thesis, York University, 182 pp., North York, Ontario.

710 Lighthill, J., 1978: *Waves in Fluids*. Cambridge University Press, 504 pp.

711 Lundquist, K. A., F. K. Chow, and J. K. Lundquist, 2010: An immersed boundary method
712 for the Weather Research and Forecasting model. *Mon. Wea. Rev.*, **138**, 796–817.

713 Makin, V. K., 2008: On the possible impact of a following-swell on the atmospheric boundary
714 layer. *Boundary-Layer Meteorol.*, **129**, 469–478.

715 Makin, V. K., V. N. Kudryavtsev, and C. Mastenbroek, 1995: Drag of the sea surface.
716 *Boundary-Layer Meteorol.*, **73**, 159–182.

- 717 McWilliams, J. C., E. Huckle, J.-H. Liang, and P. P. Sullivan, 2012: The wavy Ekman layer:
718 Langmuir circulations, breakers and Reynolds stress. *J. Phys. Oceanogr.*, **42**, 1793–1816.
- 719 McWilliams, J. C., C.-H. Moeng, and P. P. Sullivan, 1999: Turbulent fluxes and coherent
720 structures in marine boundary layers: Investigations by large-eddy simulation. *Air-Sea
721 Exchange: Physics, Chemistry, Dynamics, and Statistics*, G. Geernaert, Ed., Kluwer,
722 507–538.
- 723 Meirink, J. F. and V. K. Makin, 2001: Modelling low-Reynolds-number effects in the turbu-
724 lent air flow over water waves. *J. Fluid Mech.*, **415**, 155–174.
- 725 Mittal, R. and G. Iaccarino, 2005: Immersed boundary methods. *Annual Review of Fluid
726 Mechanics*, **37**, 239–261.
- 727 Moeng, C.-H., 1984: A large-eddy simulation model for the study of planetary boundary-
728 layer turbulence. *J. Atmos. Sci.*, **41**, 2052–2062.
- 729 Moeng, C.-H., P. P. Sullivan, M. F. Khairoutdinov, and D. A. Randall, 2010: A mixed
730 scheme for subgrid-scale fluxes in cloud resolving models. *J. Atmos. Sci.*, **67**, 3692–3705.
- 731 Moeng, C. H. and J. C. Wyngaard, 1988: Spectral analysis of large-eddy simulations of the
732 convective boundary layer. *J. Atmos. Sci.*, **45**, 3573–3587.
- 733 Nakayama, A., K. Hori, and R. L. Street, 2004: Filtering and LES of flow over irregular
734 rough boundary. *Center for Turbulence Research, Proceedings of the Summer Program*,
735 Stanford University/NASA Ames Research Center, 145–156.
- 736 Nakayama, A., K. Sakio, Y. Kitano, and S. Yokojima, 2009: Direct numerical simulation
737 and filtering of turbulent flows over model rough surfaces. *Memoirs of the Graduate School
738 of Engineering Kobe University*, **1**, 9–41.
- 739 Nilsson, E. O., A. Rutgereson, A. Smedman, and P. Sullivan, 2012: Convective boundary

layer structure in the presence of wind-following swell. *Quart. J. Roy. Meteorol. Soc.*, **138**,
1476–1489.

Phillips, O. M., 1977: *Dynamics of the Upper Ocean*. Cambridge University Press, 336 pp.

Rhie, C. M. and W. L. Chow, 1983: A numerical study of the turbulent flow past an isolated
airfoil with trailing edge separation. *AIAA J.*, **21**, 1525–1532.

Romero, L. and W. K. Melville, 2010: Airborne observations of fetch-limited waves in the
Gulf of Tehuantepec. *J. Phys. Oceanogr.*, **40**, 441–465.

Sajjadi, S. G., J. C. R. Hunt, and F. Drullion, 2013: Asymptotic multi-layer analysis of wind
over unsteady monochromatic surface waves. *J. of Engineering Mathematics*, **in press**.

Smedman, A., U. Högström, H. Bergström, and A. Rutgersson, 1999: A case study of air-sea
interaction during swell conditions. *J. Geophys. Res.*, **104**, 25 833–25 851.

Spalart, P. R., R. D. Moser, and M. M. Rogers, 1991: Spectral methods for the Navier-Stokes
equations with one infinite and two periodic directions. *J. Comp. Phys.*, **96**, 297.

Sullivan, P. P., J. B. Edson, T. Hristov, and J. C. McWilliams, 2008: Large eddy simulations
and observations of atmospheric marine boundary layers above non-equilibrium surface
waves. *J. Atmos. Sci.*, **65**, 1225–1245.

Sullivan, P. P., T. W. Horst, D. H. Lenschow, C.-H. Moeng, and J. C. Weil, 2003: Structure
of subfilter-scale fluxes in the atmospheric surface layer with application to large-eddy
simulation modeling. *J. Fluid Mech.*, **482**, 101–139.

Sullivan, P. P. and J. C. McWilliams, 2002: Turbulent flow over water waves in the presence
of stratification. *Phys. Fluids*, **14**, 1182–1195.

Sullivan, P. P. and J. C. McWilliams, 2010: Dynamics of winds and currents coupled to
surface waves. *Annual Review of Fluid Mechanics*, **42**, 19–42.

763 Sullivan, P. P., J. C. McWilliams, and C.-H. Moeng, 1996: A grid nesting method for
764 large-eddy simulation of planetary boundary layer flows. *Boundary-Layer Meteorol.*, **80**,
765 167–202.

766 Sullivan, P. P., J. C. McWilliams, and C.-H. Moeng, 2000: Simulation of turbulent flow over
767 idealized water waves. *J. Fluid Mech.*, **404**, 47–85.

768 Sullivan, P. P. and E. G. Patton, 2011: The effect of mesh resolution on convective boundary-
769 layer statistics and structures generated by large-eddy simulation. *J. Atmos. Sci.*, **68**,
770 2395–2415.

771 Sullivan, P. P., E. G. Patton, and K. W. Ayotte, 2010: Turbulent flow over and around
772 sinusoidal bumps, hills, gaps and craters derived from large eddy simulations. *19th Amer.*
773 *Meteorol. Soc. Symp. on Boundary Layer and Turbulence*, Keystone, CO.

774 Sullivan, P. P., L. Romero, J. C. McWilliams, and W. K. Melville, 2012: Transient evolution
775 of Langmuir turbulence in ocean boundary layers driven by hurricane winds and waves.
776 *J. Phys. Oceanogr.*, **42**, 1959–1980.

777 Taylor, P. A., 1998: Turbulent boundary-layer flow over low and moderate slope hills. *Journal*
778 *of Wind Engr. and Industrial Aerodynamics*, **74-76**, 25–47.

779 Thomas, P. D. and C. K. Lombard, 1979: Geometric conservation law and its application to
780 flow computations on moving grids. *AIAA Journal*, **17**, 1030–1037.

781 Wilson, J. D., 2002: Representing drag on unresolved terrain as a distributed momentum
782 sink. *J. Atmos. Sci.*, **59**, 1629–1637.

783 Wyngaard, J. C., 1998: Boundary-Layer modeling: History, philosophy, and sociology. *Clear*
784 *and Cloudy Boundary Layers*, A. A. M. Holtslag and P. G. Duynkerke, Eds., Royal Nether-
785 lands Academy of Arts and Sciences.

- 786 Wyngaard, J. C., 2004: Toward numerical modeling in the Terra Incognita. *J. Atmos. Sci.*,
787 **61**, 1816–1826.
- 788 Zang, Y., R. L. Street, and J. R. Koseff, 1994: A non-staggered grid, fractional step method
789 for time-dependent incompressible Navier-Stokes equations in curvilinear coordinates. *J.*
790 *Comp. Phys.*, **114**, 18–33.
- 791 Zheng, Z. and L. Petzold, 2006: Runge-Kutta-Chebyshev projection method. *J. Comp.*
792 *Phys.*, **219**, 976–991.

793 **List of Tables**

794	1	Simulation properties	38
-----	---	-----------------------	----

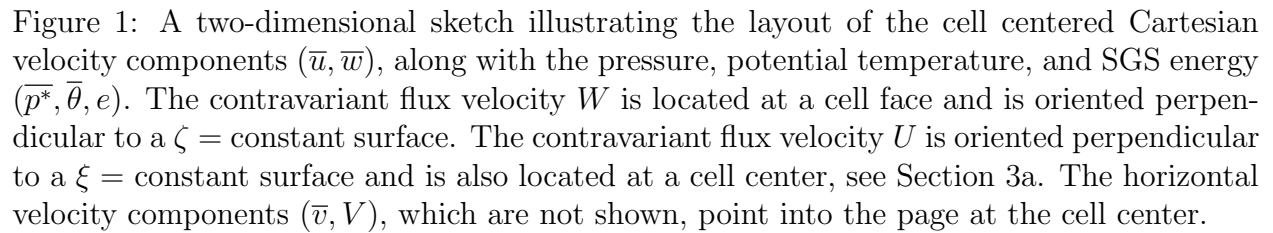
Table 1: Simulation properties

Run	U_g (m s ⁻¹)	C_p/U_{10}	u_* (m s ⁻¹)
<i>A</i>	5	4.8	0.124
<i>B</i>	7.5	3.4	0.187
<i>C</i>	10	2.8	0.228
<i>D</i>	15	1.9	0.338
<i>E</i>	20	1.5	0.452

List of Figures

- 1 A two-dimensional sketch illustrating the layout of the cell centered Cartesian velocity components (\bar{u}, \bar{w}) , along with the pressure, potential temperature, and SGS energy $(\bar{p}^*, \bar{\theta}, e)$. The contravariant flux velocity W is located at a cell face and is oriented perpendicular to a $\zeta = \text{constant}$ surface. The contravariant flux velocity U is oriented perpendicular to a $\xi = \text{constant}$ surface and is also located at a cell center, see Section 3a. The horizontal velocity components (\bar{v}, V) , which are not shown, point into the page at the cell center. 41
- 2 A two-dimensional sketch illustrating the layout of the cell centered pressure \bar{p}^* near the wavy boundary $\zeta = 0$. The pairs of indices $[(i - 1, 0), \dots, (i + 1, 2)]$ are the discrete locations of the cell centers in the (ξ, ζ) directions, respectively. Ghost point pressures are located along lines of constant $\zeta = -\Delta\zeta/2$, *i.e.*, along lines $(i, 0), i = 1, NX$. 42
- 3 A snapshot of the wavefield height $h(x, y, t)$ that is imposed at the bottom of the LES code. The horizontal grid spacing matches the LES, *i.e.*, $\Delta x = \Delta y = 2.93$ m. The color bar is in units of meters. 43
- 4 Normalized 1-D power spectra of the wave height as functions of the horizontal wavenumbers $E(k_x)$ and $E(k_y)$ normalized by the total variance $\langle h^2 \rangle$. 44
- 5 An instantaneous $x - z$ slice of the 3D time varying computational mesh in the lowest portion of the PBL. The (ξ, η) gridlines become level surfaces at about 100 m above the water. Only a fraction of the grid is displayed. 45

- 817 6 Snapshot of static pressure fluctuations p'/ρ in an $x - z$ plane near the water
818 surface. The upper panel is a swell dominated regime with wave age ~ 4.8
819 while the lower panel is a case near wind-wave equilibrium with wave age
820 ~ 1.4 . The wave spectrum is a Pierson-Moskowitz spectrum. Notice the
821 coherence between the wave field and the pressure fluctuations in the case
822 with swell. The color bar is in units of m s^{-2} and the range is different
823 between the two cases. 46
- 824 7 Snapshot of resolved vertical velocity fluctuations w'/u_* in a wave following
825 $x - y$ plane near the water surface $\zeta = 2.5$ m. The left panel is a swell
826 dominated regime with wave age ~ 4.8 while the right panel is a case near
827 wind-wave equilibrium with wave age ~ 1.4 . The wave spectrum at the bot-
828 tom of the PBLs is the same. Notice the range of the color bar is different
829 between the two cases. The (normalized) fluctuations in the wind-wave equi-
830 librium case are smaller. 47
- 831 8 Vertical profiles of wind speed (left panel) and turbulence variances (right
832 panels) for different values of wave age C_p/U_{10} . Friction velocity u_* is used
833 for normalization. The dashed black line is the rough wall formula $U/u_* =$
834 $\ln(z/z_o)/\kappa$, where $\kappa = 0.4$. Temporal and spatial averaging is used to make
835 the statistics. The spatial averaging is over $\xi - \eta$ planes, *i.e.*, at constant ζ . 48



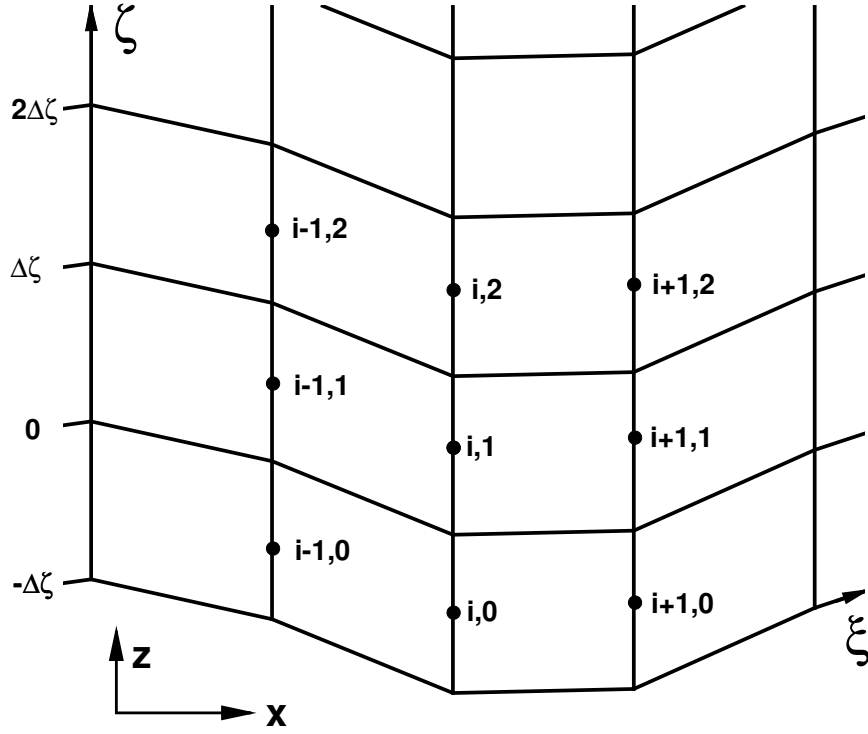


Figure 2: A two-dimensional sketch illustrating the layout of the cell centered pressure $\overline{p^*}$ near the wavy boundary $\zeta = 0$. The pairs of indices $[(i - 1, 0), \dots, (i + 1, 2)]$ are the discrete locations of the cell centers in the (ξ, ζ) directions, respectively. Ghost point pressures are located along lines of constant $\zeta = -\Delta\zeta/2$, *i.e.*, along lines $(i, 0), i = 1, NX$.

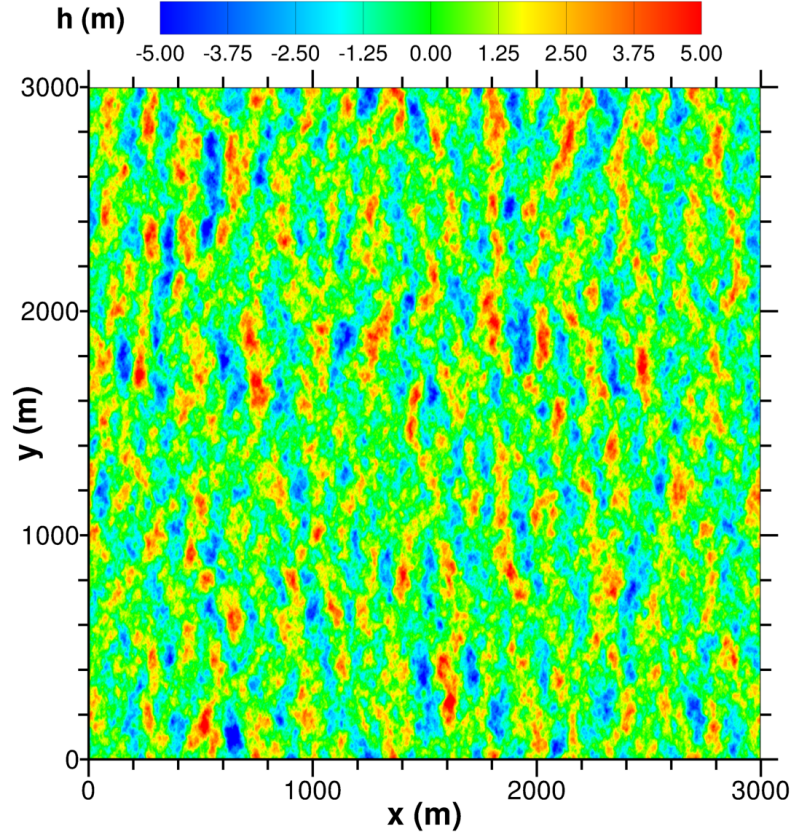


Figure 3: A snapshot of the wavefield height $h(x, y, t)$ that is imposed at the bottom of the LES code. The horizontal grid spacing matches the LES, *i.e.*, $\Delta x = \Delta y = 2.93$ m. The color bar is in units of meters.

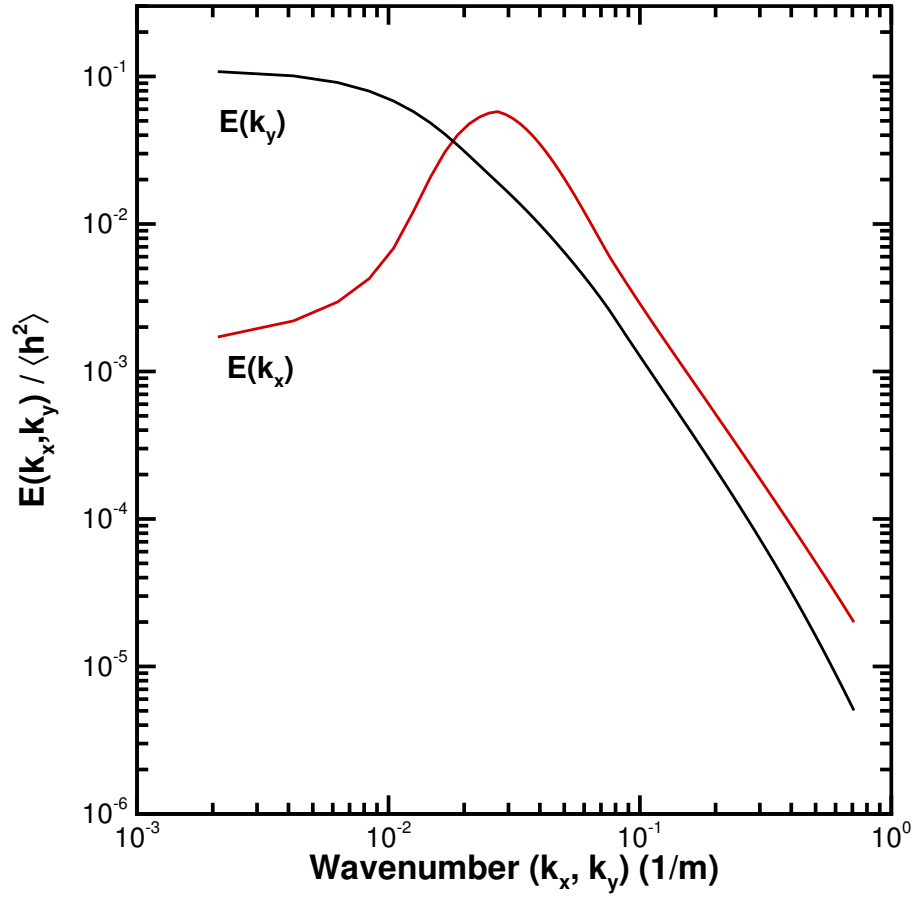


Figure 4: Normalized 1-D power spectra of the wave height as functions of the horizontal wavenumbers $E(k_x)$ and $E(k_y)$ normalized by the total variance $\langle h^2 \rangle$.

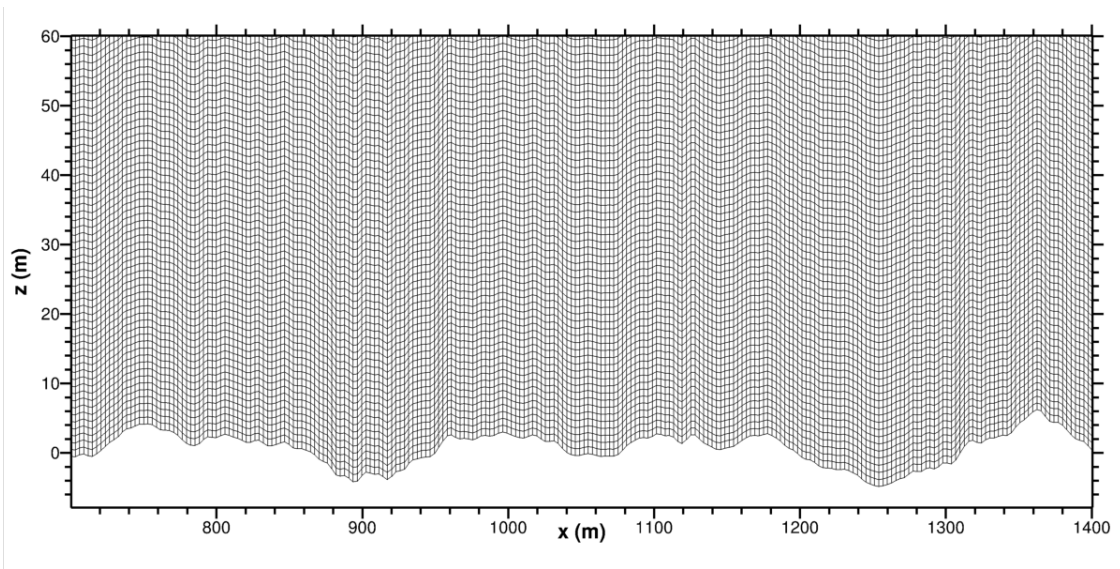


Figure 5: An instantaneous $x - z$ slice of the 3D time varying computational mesh in the lowest portion of the PBL. The (ξ, η) gridlines become level surfaces at about 100 m above the water. Only a fraction of the grid is displayed.

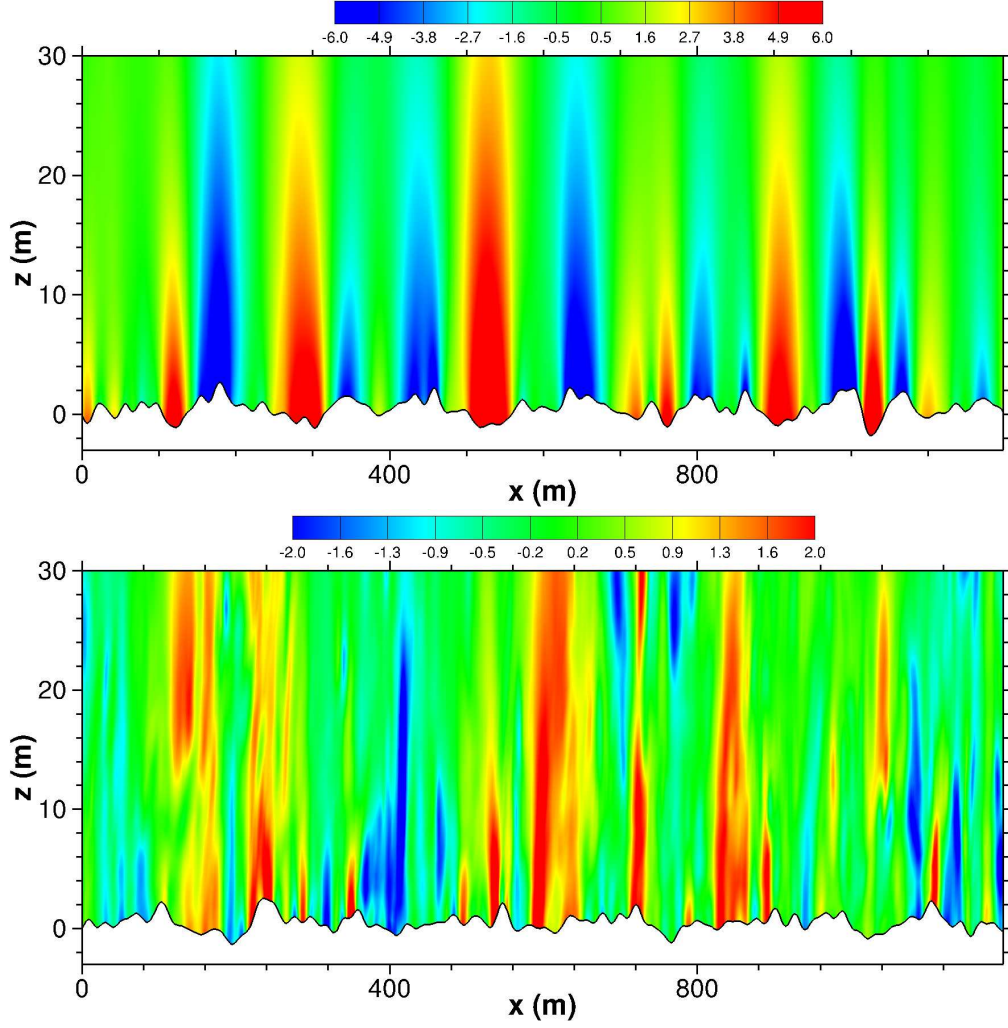


Figure 6: Snapshot of static pressure fluctuations p'/ρ in an $x - z$ plane near the water surface. The upper panel is a swell dominated regime with wave age ~ 4.8 while the lower panel is a case near wind-wave equilibrium with wave age ~ 1.4 . The wave spectrum is a Pierson-Moskowitz spectrum. Notice the coherence between the wave field and the pressure fluctuations in the case with swell. The color bar is in units of m s^{-2} and the range is different between the two cases.

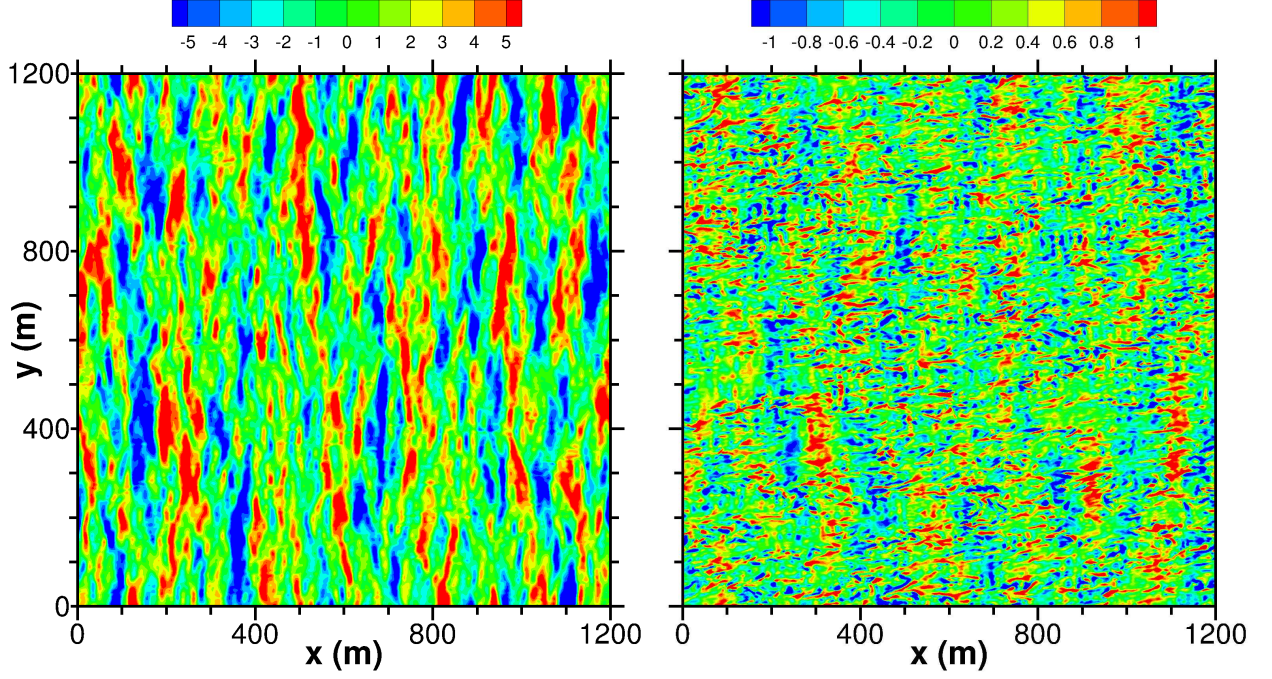


Figure 7: Snapshot of resolved vertical velocity fluctuations w'/u_* in a wave following $x - y$ plane near the water surface $\zeta = 2.5$ m. The left panel is a swell dominated regime with wave age ~ 4.8 while the right panel is a case near wind-wave equilibrium with wave age ~ 1.4 . The wave spectrum at the bottom of the PBLs is the same. Notice the range of the color bar is different between the two cases. The (normalized) fluctuations in the wind-wave equilibrium case are smaller.

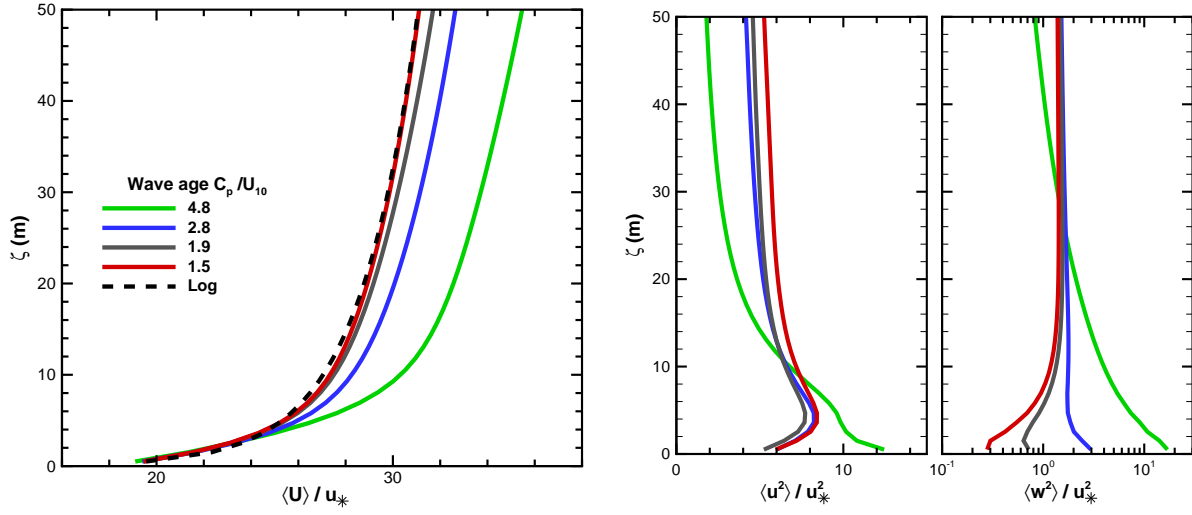


Figure 8: Vertical profiles of wind speed (left panel) and turbulence variances (right panels) for different values of wave age C_p/U_{10} . Friction velocity u_* is used for normalization. The dashed black line is the rough wall formula $U/u_* = \ln(\zeta/z_o)/\kappa$, where $\kappa = 0.4$. Temporal and spatial averaging is used to make the statistics. The spatial averaging is over $\xi - \eta$ planes, *i.e.*, at constant ζ .

4B.4 A LARGE EDDY SIMULATION MODEL OF HIGH WIND MARINE BOUNDARY LAYERS ABOVE A SPECTRUM OF RESOLVED MOVING WAVES

Peter P. Sullivan^{1*}, James C. McWilliams² and Tihomir Hristov³

¹National Center for Atmospheric Research, Boulder, CO

²Department of Atmospheric and Oceanic Sciences, UCLA, Los Angeles, CA

³Department of Mechanical Engineering, The Johns Hopkins University, Baltimore, MD

1. INTRODUCTION

An improved understanding of the interaction of winds, waves, and currents in the upper ocean at scales of individual waves and wave groups is needed to further develop the next generation of climate, weather, and wave forecast models. For example, coupled wind-wave-ocean models (Chen et al., 2007; Black et al., 2007) are viewed as critical tools for accurate prediction of tropical cyclone intensity and track forecasts, but these modeling systems employ a suite of parameterizations that are largely statistical descriptions of the wind-wave interactions that generate the critical momentum and scalar fluxes. These forecast models do not account for the important phase relationships between winds, waves and currents, *e.g.*, the spatial and temporal intermittency of wave breaking that occurs in moderate to high winds (see figure 1). Also, there is a growing appreciation that wave-current interactions are important for the upper ocean boundary layer (Sullivan and McWilliams, 2010), and thus for climate predictions, and that remotely generated swell and non-equilibrium wave states can play an important and critical role in the surface-layer dynamics of the atmospheric planetary boundary layer (PBL) (Hanley et al., 2010; Sullivan and McWilliams, 2010).

The present work describes our recent developments in coupling a turbulence-resolving large-eddy simulation (LES) of the atmospheric PBL to a three-dimensional time-dependent resolved surface wavefield. This builds on our past efforts which coupled a turbulent boundary-layer flow with a single monochromatic wave (Sullivan et al., 2000; Sullivan and McWilliams, 2002; Sullivan et al., 2008). The computational method described here allows for nearly arbitrary 3D wavefields, *i.e.*, the sea surface elevation $h = h(x, y, t)$, as a surface boundary condition. The spatial scales of the resolved turbulence and waves are $O(m)$ up to the scale of the PBL height. At present, the waves are externally imposed based on empirical wave spectra. Ultimately the wavefields will

be direct observations of the sea surface from field campaigns. High resolution simulations of PBL turbulence in the presence of surface waves has the potential to provide new insight into the dynamics of air-sea coupling at small scales. The jump in massively parallel computational resources facilitates the coupling of winds and waves in turbulence resolving simulations.

2. LES ALGORITHM WITH MOVING WAVES

An LES model for an atmospheric PBL with a stationary undulating lower boundary is described in Sullivan et al. (2010). They outline the algorithm, numerical details, code parallelization, and present results for boundary-layer flows over and around two- and three-dimensional orography. Here we build on those developments but focus on the additional complications caused by the temporal movement of the 3D lower surface. In the description of the model equations, given in Section 2.2, the following notation is used: $\rho \bar{\mathbf{u}}$ denotes the Cartesian components of momentum, θ is virtual potential temperature, e is the subgrid-scale energy, and $\bar{\Pi}$ is the pressure variable. Quantities with an overbar ($\bar{}$) are interpreted as LES spatially filtered variables.

2.1 Coordinate transformation

We follow Sullivan et al. (2010) and adapt our LES model with a flat bottom to the situation with a three-dimensional time-dependent boundary shape $h = h(x, y, t)$ by applying a transformation to the physical space coordinates (x, y, z) that maps them onto computational coordinates (ξ, η, ζ) . The computational mesh in physical space is surface following, non-orthogonal, and time varying. Also, vertical gridlines are held fixed at a particular (x, y) location on the surface but the lines are permitted to undergo vertical translation as a function of time t , *i.e.*, vertical gridlines are wave following. The transformation which obeys these constraints and maps the physical domain to a flat computational domain $\mathbf{x} \Rightarrow \xi$ is the rule:

*corresponding author address: Peter P. Sullivan, National Center for Atmospheric Research, P. O. Box 3000, Boulder, CO 80307-3000; email: pps@ucar.edu

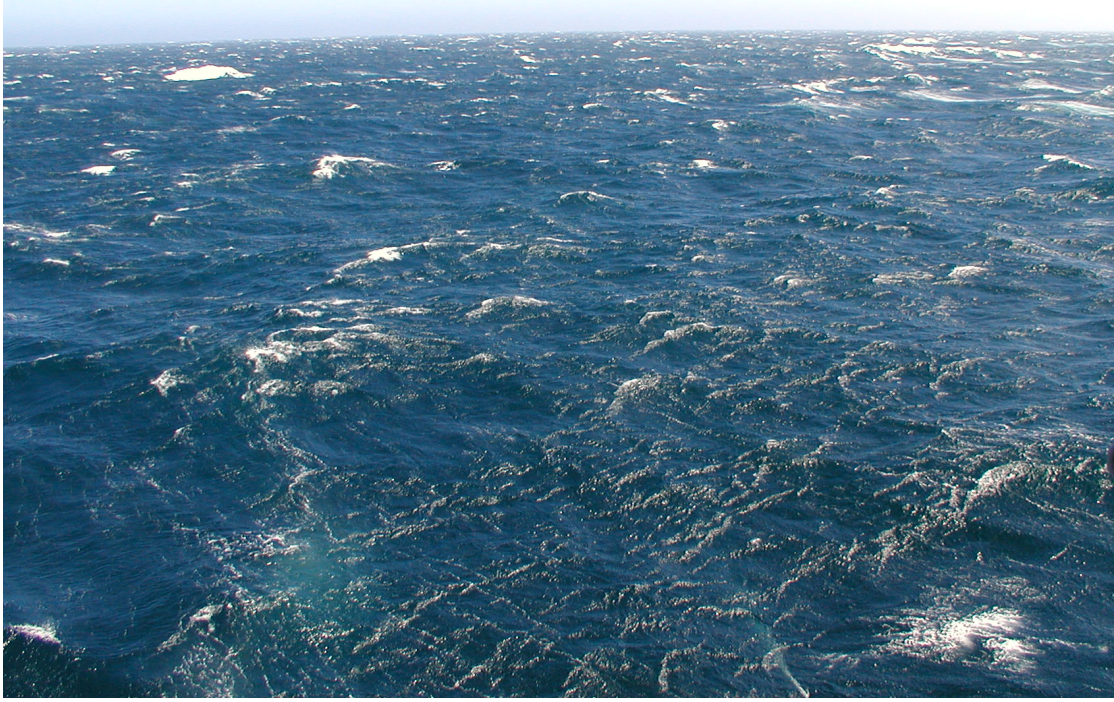


Figure 1: Photograph of the sea surface generated by winds of approximately 15 m s^{-1} during the High Resolution Air-Sea Interaction (Hi-Res) field campaign carried out in June 2010. Notice the extensive white capping generated by large-scale plunging and spilling breakers and, in the foreground, a web of small-scale breakers. The photograph is taken from the R/V Floating Instrument Platform (FLIP) courtesy of Tihomir Hristov. For a description of Hi-Res see <http://airsea.ucsd.edu/hires/>.

$$\tau = t \quad (1a)$$

$$\xi = \xi(x) = x \quad (1b)$$

$$\eta = \eta(y) = y \quad (1c)$$

$$\zeta = \zeta(t, x, y, z). \quad (1d)$$

The differential metrics $\partial x_i / \partial \xi_j$ and $\partial \xi_i / \partial x_j$, which are needed in formulating the LES model, are connected through the mapping transformation. Thus given the rules in (1) we have the reduced set of non-zero metric relationships:

$$\zeta_t = -z_t J \quad (2a)$$

$$\zeta_x = -z_\xi J \quad (2b)$$

$$\zeta_y = -z_\eta J \quad (2c)$$

$$\zeta_z = 1/z_\zeta = J \quad (2d)$$

$$\xi_x = \eta_y = 1 \quad (2e)$$

where J is the Jacobian. The time dependence of the mapping appears in (2a) where $z_t = \partial z / \partial t$ is the *grid speed*, i.e., the vertical velocity of individual gridpoints.

2.2 LES equations in curvilinear coordinates with time dependence

The LES equations in curvilinear coordinates are derived in a straightforward manner by applying the chain rule for differentiation but we pay close attention to the transformation of the material derivative $D(\cdot)/Dt$ and the mass conservation equation. The set of LES equations in computational coordinates under the transformation (1) and (2) are:

$$\frac{\partial U_i}{\partial \xi_i} = 0 \quad (3a)$$

$$\frac{\partial}{\partial t} \left(\frac{1}{J} \right) = \frac{\partial z_t}{\partial \zeta} \quad (3b)$$

$$\frac{\partial}{\partial t} \left(\frac{\bar{u}_i}{J} \right) + \frac{\partial}{\partial \xi_j} [(U_j - \delta_{3j} z_t) \bar{u}_i] = \mathcal{F}_i \quad (3c)$$

$$\frac{\partial}{\partial t} \left(\frac{\bar{\theta}}{J} \right) + \frac{\partial}{\partial \xi_j} [(U_j - \delta_{3j} z_t) \bar{\theta}] = \mathcal{M} \quad (3d)$$

$$\frac{\partial}{\partial t} \left(\frac{e}{J} \right) + \frac{\partial}{\partial \xi_j} [(U_j - \delta_{3j} z_t) e] = \mathcal{R} \quad (3e)$$

$$\frac{\partial}{\partial \xi_i} \left[\frac{1}{J} \frac{\partial \xi_i}{\partial x_j} \frac{\partial \xi_m}{\partial x_j} \frac{\partial \Pi}{\partial \xi_m} \right] = \mathcal{S} \quad (3f)$$

The equations are expressed in strong conservation form using the “contravariant flux” velocity

$$U_i = \frac{\bar{u}_j}{J} \frac{\partial \xi_i}{\partial x_j}. \quad (4)$$

(3a) is the mass conservation (continuity) equation, (3c) is the momentum transport equation, (3d) is the scalar transport equation, (3e) is the subgrid-scale energy transport equation, and (3f) is the pressure Poisson equation. The right hand sides of (3) model physical processes in the marine atmospheric PBL, *e.g.*, pressure gradients, Coriolis rotation, divergence of subgrid-scale fluxes, buoyancy, and in the case of the SGS ϵ equation also diffusion and dissipation.

The time dependence of the grid modifies the LES equations: the Jacobian appears inside the time tendency of each transport equation and as expected advection contains a contribution from the grid movement, *i.e.*, the total vertical flux of variable ψ depends on the difference between the physical velocity and grid speed $(W - z_t)\psi$. Also, as a consequence of writing the equations in strong conservation form we need to satisfy (3b) which is a simplified form of the so-called geometric or space conservation law (GCL) first discussed by Thomas and Lombard (1979). In our derivation, (3b) follows directly from considering the unsteady form of the mass conservation equation written in differential form. Thomas and Lombard (1979) and also Demirdžić and Perić (1990) derive the GCL by considering an integral form of the equations of motion. Inspection of (3) shows that if the velocity and scalar fields are set to constant values then the left hand sides of (3c-e) reduce to (3b). Hence our numerical method needs to satisfy our reduced form of the GCL discretely in order to prevent artificial sources and sinks from developing in the computational domain. Thus, the mixed pseudospectral finite-differencing spatial differencing evaluates the advective terms in (3c-e) in flux form and not the rotational form used by Moeng (1984) or skew-symmetric form used by Sullivan et al. (2000).

We use (3b) with our Runge-Kutta time stepping scheme in the following way: Given the wave height distribution at any future timestep, say t^{n+1} , we first pick the vertical distribution of gridpoints $z(\xi, \eta, \zeta, t^{n+1})$ based on the computational domain height and $h(\xi, \eta, t^{n+1})$. We then insert the Runge-Kutta time stepping discretization in (3b) and solve for the required matching grid speed z_t . Since our time stepping is explicit the value of z_t diagnosed applies at the time level t^n . In other words, if the wavefield is imposed knowledge of its future shape is needed to diagnose the grid speed at an earlier time. This is analogous to our grid nesting scheme where the vertical velocity at a future time is imposed on a nested boundary (Sullivan et al., 1996).

We emphasize that the upper boundary of our computational domain is far from the lower surface and asymptotes to a flat level surface. As a result z_t varies with distance from the wave surface. This is different than the scheme proposed by Chalikov (1998) where the grid speed is equal to the vertical motion of the wavefield for all z . This implies that the computational mesh at any ζ , including the upper boundary, mimics the shape of the lower surface. At the lower boundary $z = h$, the time rate of change of the wavy surface is

$$z_t \equiv h_t = w_o - h_\xi u_o - h_\eta v_o \quad (5)$$

where (u_o, v_o, w_o) are the orbital motions of the wavefield. The kinematical boundary condition is then $W - z_t = 0$ so that there is no flow through the boundary. Notice the definition of $W(z = h)$ given by (4) is consistent with (5). The surface grid movement also leads to subtleties in formulating the pressure Poisson equation and its boundary conditions.

2.3 Wavefield prescription

To complete our marine PBL LES we need to prescribe the surface wavefield. For the present computations we use empirical two-dimensional statistical wave spectra (*e.g.*, see Komen et al., 1994, p. 187)

$$E(k, \phi) = S(k) D(k, \phi) \quad (6)$$

where the amplitude $S(k)$ and directional $D(k, \phi)$ spectra depend on the wavenumber $k = |\mathbf{k}| = |k_x \hat{\mathbf{i}} + k_y \hat{\mathbf{j}}|$, wave direction ϕ and surface wind speed U_{10} . For the amplitude spectrum we choose the classic Pierson-Moskowitz shape (Pierson and Moskowitz, 1964; Alves et al., 2003) while a simple directional spectrum is designed to emphasize long-crested waves with their spanwise axis oriented perpendicular to the wind direction $D(k, \phi) = (\mathbf{k} \cdot \mathbf{U})^n$. In physical space, the synthetic wavefield $h(x, y, t)$ is constructed from a sum of plane waves

$$h(\mathbf{x}, t) = \sum_{\mathbf{k}} \hat{h}(\mathbf{k}) \exp[i(\mathbf{k} \cdot \mathbf{x} - \omega t)] \quad (7)$$

with the wave amplitudes $\hat{h}(\mathbf{k})$ picked to match $E(k, \phi)$. The phases are chosen from a Gaussian distribution. Inside the LES, the wavefield is advanced in time using the linear dispersion relation $\omega^2 = gk$ once the initial distribution of amplitudes is specified. (7) is efficiently evaluated using 2D Fast Fourier Transforms. Figure 2 shows a typical instantaneous 3D wavefield that is input at the bottom of the LES. Future computations will use the detailed phase-resolved wave measurements collected in the Hi-Res field campaign.

3. SIMULATIONS

A series of simulations with varying geostrophic wind $U_g = (5, 7.5, 10, 15, 20)$ m s⁻¹ are carried out for a neutrally-stratified marine PBL in a domain $(X_L, Y_L, Z_L) = (1200, 1200, 800)$ m using $(N_x, N_y, N_z) = (512, 512, 128)$ gridpoints; thus the horizontal grid spacing $\Delta x = \Delta y = 2.34$ m and the first vertical level is 1 m above the water. A slice of the computational mesh is given in figure 3. The initial temperature sounding $\bar{\theta} = 300$ K up to the inversion height $z_i = 400$ m, beyond this height $\bar{\theta}$ increases linearly at 3×10^{-3} K m⁻¹. The surface heating $Q_* = 0$, the surface roughness $z_o = 0.0002$ m, and the Coriolis parameter $f = 10^{-4}$ s⁻¹. The wavefield is built, as discussed in Section 2.3, based on a wind speed of 15 m s⁻¹ and the phase speed of the peak in the spectrum $C_p \sim 18$ m s⁻¹. Thus the suite of simulations allows us to examine a wide variation of wave age from swell dominated to near wind-wave equilibrium. Table 1 lists bulk properties of the simulations, *viz.*, the geostrophic wind, wave age, and friction velocity u_* . U_{10} is the reference wind speed at a height of 10 m. The simulations are run for more than 50,000 timesteps using restart volumes with fully developed turbulence. The iteration count in the pressure Poisson solver is typically set to 30 and the calculations run on either 512 or 1024 computational cores.

Table 1: Simulation properties

Run	U_g (m s ⁻¹)	C_p/U_{10}	u_* (m s ⁻¹)
A	5	4.8	0.124
B	7.5	3.4	0.187
C	10	2.8	0.228
D	15	1.9	0.338
E	20	1.5	0.452

4. RESULTS

Previous field observations (Grachev and Fairall, 2001; Smedman et al., 1999), turbulence closure modeling (Hanley and Belcher, 2008; Makin, 2008), and our own idealized LES (Sullivan et al., 2008) all show that fast moving swell can induce marked changes in the atmospheric surface layer winds, *viz.*, an upward momentum flux from the ocean to the atmosphere, a low-level wind maximum, and departures from law-of-the-wall scaling. The preliminary LES computations performed here over a more realistic sea surface are in good qualitative agreement with the previous studies but suggest the impact of swell on the surface layer winds is sensitive to the content of the wave spectrum.

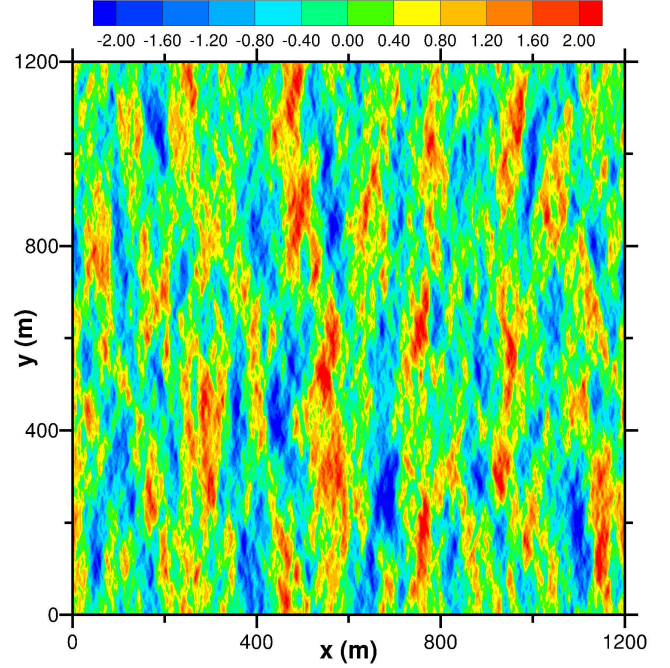


Figure 2: A snapshot of the wavefield height $h(x, y, t)$ that is imposed at the bottom of the LES code. h is built from a sum of linear plane waves (7). Waves propagate left to right according to the dispersion relationship. The horizontal grid spacing matches the LES, *i.e.*, $\Delta x = \Delta y = 2.5$ m. The color bar is in units of meters.

One of the surprising results from the present simulations is the significant impact of swell on the coherence and magnitude of the near-surface pressure fluctuations. This is illustrated in figure 4 where we compare p'/ρ for two levels of wind forcing $U_g = (5, 20)$ m s⁻¹, *i.e.*, a low-wind situation with swell and a high wind case approaching wind-wave equilibrium. The difference in the pressure signals is striking and even more remarkable in animations of the pressure field. In the low-wind swell case there is a very strong correlation between $p'/\rho < 0$ and wave crests and similarly between $p'/\rho > 0$ and wave troughs that extends over the depth of the surface layer. Inspection of the flow visualization and animations reveals that the strong correlation persists across the range of resolved waves, *i.e.*, both large and small scale waves appear to induce a similar pressure pattern. The coherence of the wave induced pressure field can extend to 20 m or more depending on the amplitude of the underlying wave. Also, the pressure signatures propagate at the speed of the wavefield, additional evidence that the signals are generated by surface waves and not atmospheric processes. These are clear signatures of “wave pumping” by the surface wavefield on the atmosphere. The ampli-

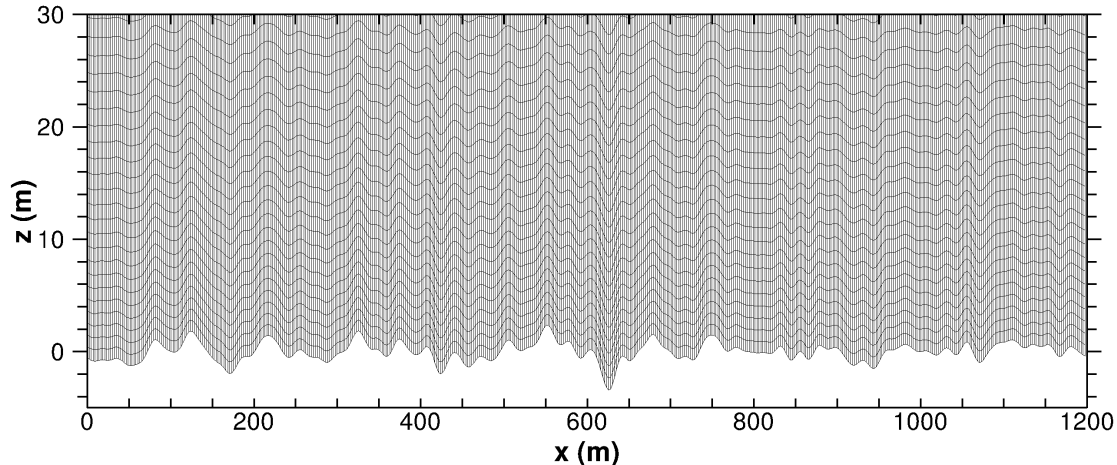


Figure 3: An instantaneous $x - z$ slice of the 3D time varying computational mesh in the lowest portion of the PBL. The (ξ, η) gridlines become level surfaces at about 100 m above the water. Only a fraction of the grid is displayed.

tude of the wave spectrum (and hence the level of wave forcing) is held constant in our simulations but the magnitude of the turbulence, as measured by u_* , increases substantially with increasing wind speed. The structure of the near surface pressure field is a result of these two competing effects. At low winds coherent pressure signals are generated by the wave motions when the turbulence is weak but this coherence is destroyed by strong turbulence at higher winds.

Figure 5 shows that the impact of wave age also appears in the vertical velocity fields. In the low-wind swell regime we observe large-amplitude large-scale fluctuations in w' . At higher winds the spatial coherence of w' is destroyed by strong turbulence. Note each panel in figure 5 is sampled at the sample height above the wavefield. Also, the fields are made dimensionless by friction velocity u_* which further illustrates the strong impact of the wave motions on the winds in the surface layer.

In figure 6 we compare vertical profiles of the mean wind speed and turbulence variances for the different simulations. These statistics are computed by averaging in computational coordinates, *i.e.*, across horizontal planes at constant vertical height ζ . Similar to Sullivan et al. (2008) we find that the wind speed and turbulence variances depend on wave age. At high winds as the simulations approach wind-wave equilibrium, the non-dimensional wind profile $\langle U \rangle / u_*$ smoothly approaches the variation predicted by law-of-the-wall. Significant differences are observed for the cases dominated by swell: the surface layer winds are accelerated compared to rough wall scaling. As suggested by the flow visualization, the turbulence variances respond to the wave motion in dramatic ways. The horizontal and vertical variances are significantly enhanced by the motion of the

wave surface in the low-wind cases. Even though the turbulence is relatively weak the turbulence variances are large near the wave surface due to wave pumping.

5. SUMMARY

A large-eddy simulation (LES) model for the marine atmospheric planetary boundary layer (PBL) is coupled to a 3D time-dependent surface gravity wavefield. A coordinate transform from physical to computational space is used that accounts for vertical movement of the mesh in physical space. We use the geometric conservation law (GCL) (Thomas and Lombard, 1979) to solve for the grid speeds that enter into the advection of momentum and scalars. The algorithm is used to carry out a series of simulations over a broadband moving wavefield that conforms to a Pierson-Moskowitz wave spectrum. The wave age $C_p / U_{10} = [1.5, 4.8]$ varies from near wind-wave equilibrium to a low-wind swell dominated regime. In the low wind cases we find features similar to previous observational and modeling investigations: the surface layer winds show clear departures from rough wall law-of-the-wall scaling. The coherence and magnitude of the pressure field p' / ρ depends critically on the motion of the underlying wavefield and the turbulence level.

Acknowledgments: The authors and their research are supported by the Office of Naval Research, Physical Oceanography program. P. Sullivan is also supported by the National Science Foundation through the National Center for Atmospheric Research. Computational resources were supplied by NCAR and the Department of Defense High Performance Computing. NCAR is spon-

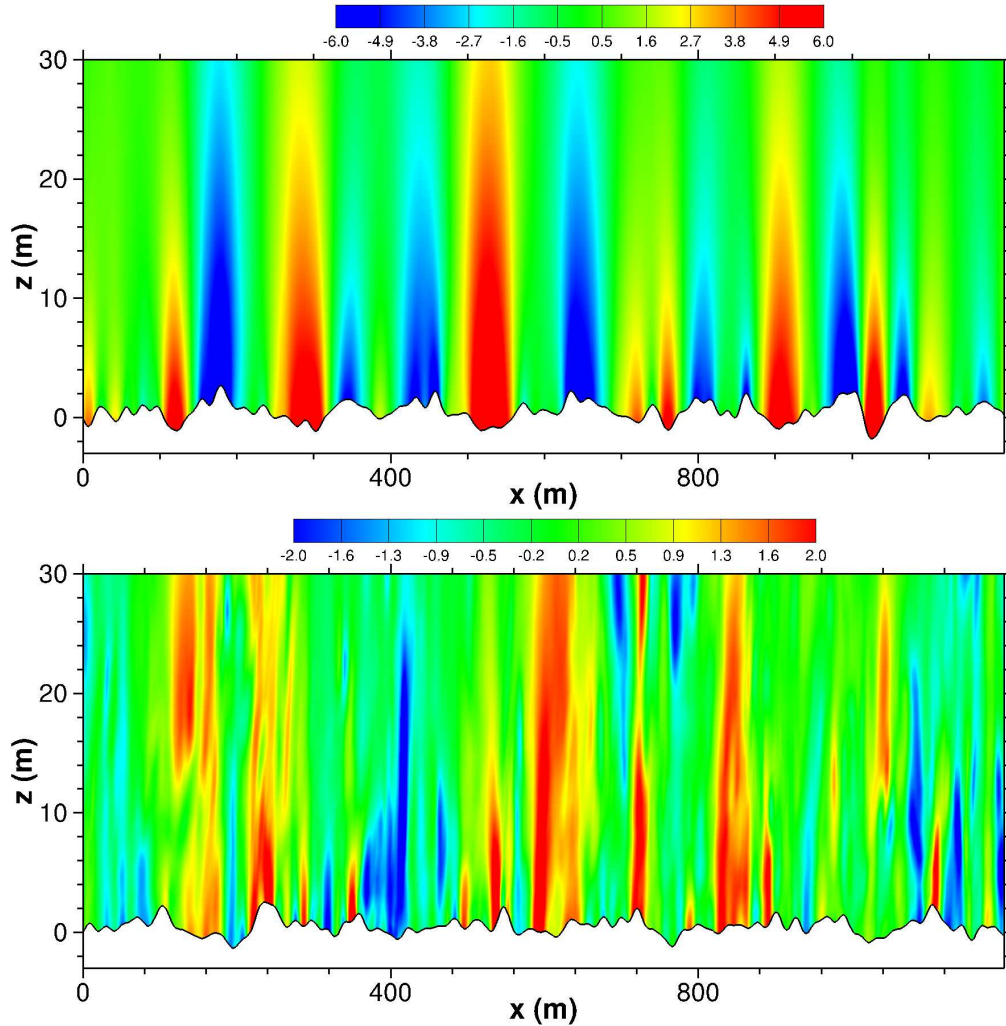


Figure 4: Snapshot of static pressure fluctuations p'/ρ in an $x-z$ plane near the water surface. The upper panel is a swell dominated regime with wave age ~ 4.8 while the lower panel is a case near wind-wave equilibrium with wave age ~ 1.4 . The wave spectrum is a Pierson-Moskowitz spectrum. Notice the coherence between the wave field and the pressure fluctuations in the case with swell. The color bar is in units of m s^{-2} and the range is different between the two cases.

sored by the National Science Foundation. Any opinions, findings, and conclusions or recommendations expressed in this publication are those of the author(s) and do not necessarily reflect the views of the National Science Foundation.

REFERENCES

- Alves, J. G. M., M. L. Banner, and I. R. Young, 2003: Revisiting the Pierson-Moskowitz asymptotic limits for fully developed wind waves, *J. Phys. Oceanogr.*, **33**, 1301–1323.
- Black, P., E. D'Asaro, W. Drennan, J. French, P. Niiler, T. Sanford, E. Terrill, E. Walsh, and J. Zhang, 2007: Air-sea exchange in hurricanes: Synthesis of observations from the Coupled Boundary Layers Air-Sea Transfer experiment, *Bull. Amer. Meteorol. Soc.*, **88**, 357–374.
- Chalikov, D., 1998: Interactive modeling of surface waves and boundary layer, in *Ocean Wave Measurement and Analysis: Proceedings of the Third International Symposium Waves 97*, edited by B. L. Edge, J. M. Hemsley, and Y. Goda, pp. 1525–1539, American Society of Civil Engineers.
- Chen, S. S., J. F. Price, W. Zhao, M. A. Donelan, and E. J. Walsh, 2007: The CBLAST-Hurricane program and the next-generation fully coupled atmosphere-wave-

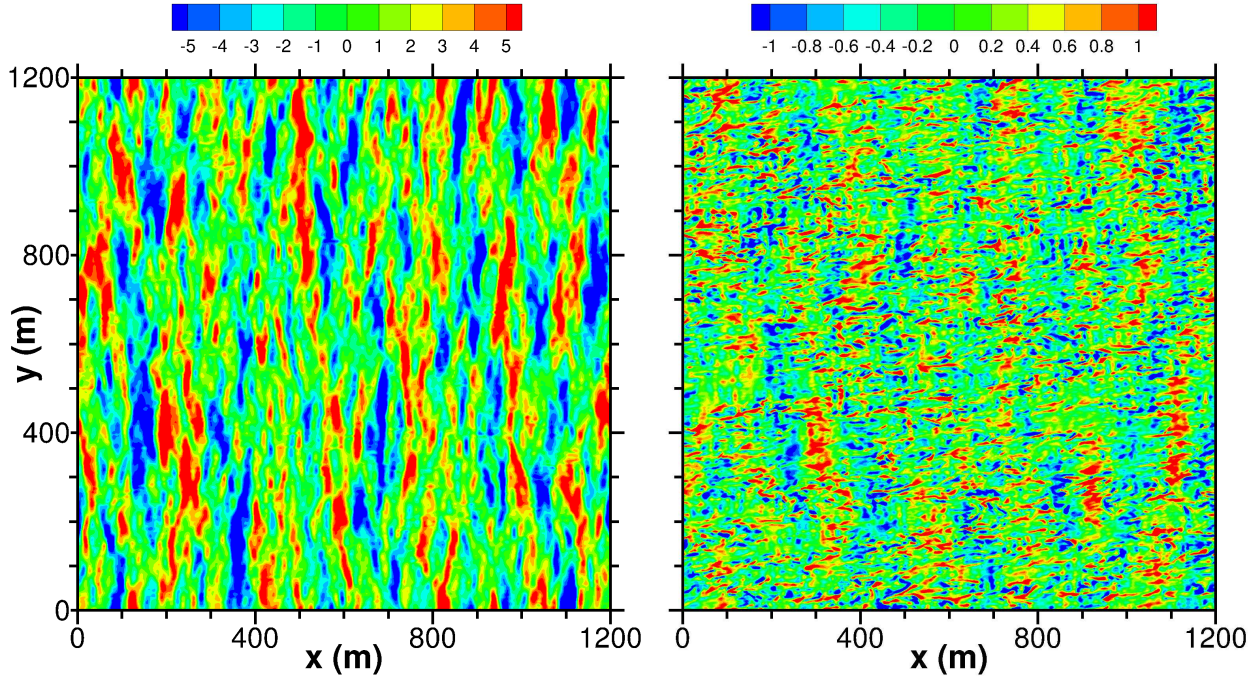


Figure 5: Snapshot of resolved vertical velocity fluctuations w'/u_* in a wave following $x-y$ plane near the water surface $\zeta = 2.5$ m. The left panel is a swell dominated regime with wave age ~ 4.8 while the right panel is a case near wind-wave equilibrium with wave age ~ 1.4 . The wave spectrum at the bottom of the PBLs is the same. Notice the range of the color bar is different between the two cases. The (normalized) fluctuations in the wind-wave equilibrium case are smaller.

- ocean models for hurricane research and prediction, *Bull. Amer. Meteorol. Soc.*, **88**, 311–317.
- Demirdžić, I. and M. Perić, 1990: Finite volume method for prediction of fluid flow in arbitrarily shaped domains with moving boundaries, *International Journal for Numerical Methods in Fluids*, **10**, 771–790.
- Grachev, A. A. and C. W. Fairall, 2001: Upward momentum transfer in the marine boundary layer, *J. Phys. Oceanogr.*, **31**, 1698–1711.
- Hanley, K. E. and S. E. Belcher, 2008: Wave-Driven wind jets in the marine atmospheric boundary layer, *J. Atmos. Sci.*, **65**, 2646–2660.
- Hanley, K. E., S. E. Belcher, and P. P. Sullivan, 2010: A global climatology of wind-wave interaction, *J. Phys. Oceanogr.*, **40**, 1263–1282.
- Komen, G. J., L. Cavaleri, M. Donelan, K. Hasselmann, S. Hasselmann, and P. A. E. M. Janssen, 1994: *Dynamics and Modelling of Ocean Waves*, Cambridge University Press, 532 pp.
- Makin, V. K., 2008: On the possible impact of a following-swell on the atmospheric boundary layer, *Boundary-Layer Meteorol.*, **129**, 469–478.
- Moeng, C.-H., 1984: A large-eddy simulation model for the study of planetary boundary-layer turbulence, *J. Atmos. Sci.*, **41**, 2052–2062.
- Pierson, W. J. and L. Moskowitz, 1964: A proposed spectral form for fully developed wind seas based on the similarity theory of S. A. Kitaigorodskii, *J. Geophys. Res.*, **69**, 5181–5190.
- Smedman, A., U. Höglström, H. Bergström, and A. Rutgersson, 1999: A case study of air-sea interaction during swell conditions, *J. Geophys. Res.*, **104**, 25833–25851.
- Sullivan, P. P., J. B. Edson, T. Hristov, and J. C. McWilliams, 2008: Large eddy simulations and observations of atmospheric marine boundary layers above non-equilibrium surface waves, *J. Atmos. Sci.*, **65**, 1225–1245.
- Sullivan, P. P. and J. C. McWilliams, 2002: Turbulent flow over water waves in the presence of stratification, *Phys. Fluids*, **14**, 1182–1195.

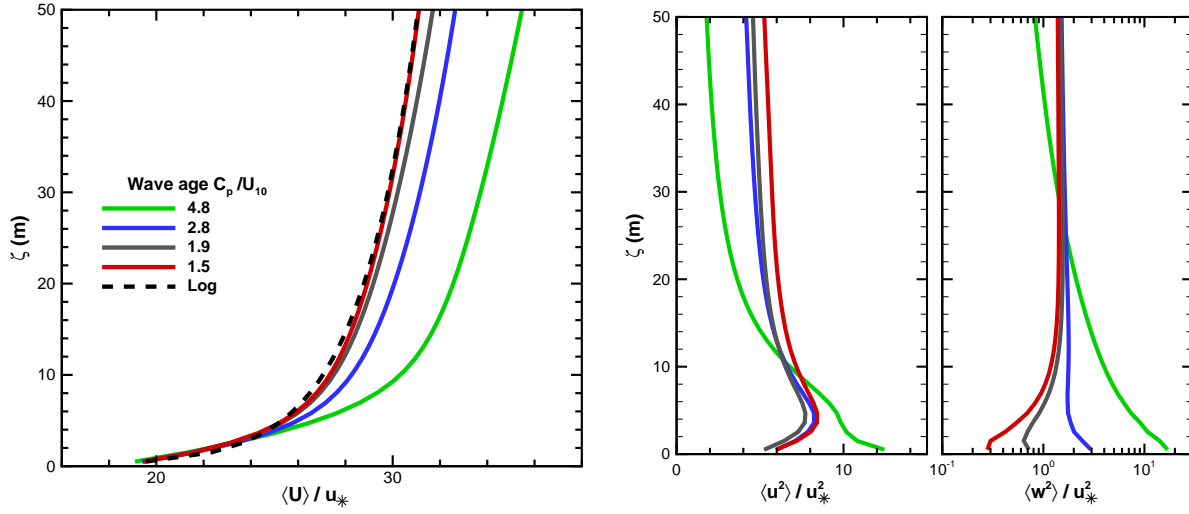


Figure 6: Vertical profiles of wind speed (left panel) and turbulence variances (right panels) for different values of wave age C_p/U_{10} . Friction velocity u_* is used for normalization. The dashed black line is the rough wall formula $U/u_* = \ln(\zeta/z_o)/\kappa$, where $\kappa = 0.4$. Temporal and spatial averaging is used to make the statistics. The spatial averaging is over $\xi - \eta$ planes, *i.e.*, at constant ζ .

—, 2010: Dynamics of winds and currents coupled to surface waves, *Ann. Rev. Fluid Mech.*, **42**, 19–42.

Sullivan, P. P., J. C. McWilliams, and C.-H. Moeng, 1996: A grid nesting method for large-eddy simulation of planetary boundary layer flows, *Boundary-Layer Meteorol.*, **80**, 167–202.

—, 2000: Simulation of turbulent flow over idealized water waves, *J. Fluid Mech.*, **404**, 47–85.

Sullivan, P. P., E. G. Patton, and K. W. Ayotte, 2010: Turbulent flow over and around sinusoidal bumps, hills, gaps and craters derived from large eddy simulations, in *19th Amer. Meteorol. Soc. Symp. on Boundary Layer and Turbulence*, Keystone, CO.

Thomas, P. D. and C. K. Lombard, 1979: Geometric conservation law and its application to flow computations on moving grids, *AIAA Journal*, **17**, 1030–1037.

1B.5 TURBULENT FLOW OVER AND AROUND SINUSOIDAL BUMPS, HILLS, GAPS AND CRATERS DERIVED FROM LARGE EDDY SIMULATIONS

Peter P. Sullivan^{1*}, Edward G. Patton¹ and Keith W. Ayotte²

¹National Center for Atmospheric Research, Boulder, CO

²Windlab Systems, Canberra, AU

1. INTRODUCTION

A wide spectrum of atmospheric motions impacts the flow environment in and around wind farms. The important time and space scales span an enormous range, large-scale long-time decadal climate down to rapidly evolving thin boundary layers that grow on an individual turbine blade (Schreck et al., 2008). In this scale hierarchy, the atmospheric planetary boundary layer (PBL), where the important scales range from $O(m)$ or less to $O(km)$ or more, plays a critical if not dominant role in setting the performance of an individual turbine as well as the power output of an entire wind park. PBL motions are turbulent (three-dimensional and time dependent) and couple to larger-scale atmospheric motions and land use, *e.g.*, weather events diurnal heating and cooling, thermal stratification, surface roughness, vegetative canopies, wind waves and local orography all influence wind turbine performance to varying degrees. For example, the afternoon collapse of the heated daytime PBL over the Great Plains followed by surface cooling can lead to a windy weakly stratified boundary layer with a nocturnal jet positioned near hub height $z \sim 100$ m (Beare et al., 2006; Banta et al., 2008). Turbulence in this regime is episodic, non-Gaussian, and can interact with gravity waves and trigger Kelvin-Helmholtz instabilities leading to intermittent loads that fatigue turbine components (Kelley et al., 2003).

The objective of the present work is to describe our recent developments in constructing and utilizing a large-eddy simulation (LES) model for the atmospheric PBL where the lower boundary shape is modestly complex, *i.e.*, we define modestly complex as orography of height h to be a single valued function of the horizontal coordinates $h = h(x, y)$. This enhanced simulation capability will allow us to examine basic interactions between stratified PBL turbulence and landscape features, but also provide information about the winds turbines might be exposed to in a local undulating environment. Understanding the flow environment created by complex small-



Figure 1: Cathedral Rocks wind farm located above an escarpment on the Eyre Peninsula South Australia adapted from http://www.yorkcivil.com.au/projects/projects/49/cathedral_rocks_wind_farm.

scale topography, as in figure 1, is of particular importance because steep slopes often generate high levels of turbulence in zones of intermittent flow separation. Coupled with background PBL turbulence this orographically generated turbulence can significantly restrict the area available for turbine placement, in which the flow conforms to turbine design standards (IEC, 2005; Ayotte, 2008). We emphasize that a complete simulation of all the turbulence length and time scales generated by the terrain in figure 1 far exceeds current computational capabilities.

2. LES ALGORITHM WITH SURFACE TERRAIN

2.1 LES with a flat lower boundary

Typical LES model equations for a dry Boussinesq PBL include at a minimum: a) transport equations for momentum $\rho \mathbf{u}$; b) a transport equation for a conserved buoyancy variable (*e.g.*, virtual potential temperature $\bar{\theta}$); c) a discrete Poisson equation for a pressure variable Π to enforce incompressibility; and closure expressions for subgrid-scale (SGS) variables, *e.g.*, a subgrid-scale

*corresponding author address: Peter P. Sullivan, National Center for Atmospheric Research, P. O. Box 3000, Boulder, CO 80307-3000; email: pps@ucar.edu

equation for turbulent kinetic energy e . Our notation denotes a resolved scale variable by an overbar ($\bar{\cdot}$) and thus $\bar{\mathbf{u}}$ are spatially filtered Cartesian velocity components. In our LES code with a flat boundary the spatial discretization is second-order finite difference in the vertical z direction and pseudospectral in horizontal $x-y$ planes. Thus a staggered arrangement of variables is used with $(\bar{u}, \bar{v}, \Pi, \bar{\theta})$ stored at cell centers and (\bar{w}, e) located at cell faces; this variable layout is advantageous because it tightly couples velocity and pressure in our incompressible formulation. The equations are integrated forward in time using a fractional step method utilizing dynamic time stepping with a fixed Courant-Fredrichs-Lewy (CFL) number (Sullivan et al., 1996; Spalart et al., 1991). The code parallelization is accomplished using the Message Passing Interface (MPI) and a 2D domain decomposition. Simulations have used as many as 16,384 computational cores for meshes with 3072^3 gridpoints (Sullivan and Patton, 2010).

2.2 Coordinate transformation

In order to adapt the LES model with a flat lower bottom, outlined in Section 2.1, to an atmospheric PBL flow with a varying boundary shape we apply a conventional grid transformation to the LES equations. The transformation maps the surface following non-orthogonal mesh onto a flat computational space $\mathbf{x} \Rightarrow \boldsymbol{\xi}$ according to the rule:

$$x = x(\boldsymbol{\xi}) = \xi \quad (1a)$$

$$y = y(\boldsymbol{\eta}) = \eta \quad (1b)$$

$$z = z(\boldsymbol{\xi}, \boldsymbol{\eta}, \zeta). \quad (1c)$$

The Jacobian, which is needed to move between physical and computational spaces, is (Anderson et al., 1984, see Eq. 5-234)

$$J = \det \begin{vmatrix} \xi_x & 0 & 0 \\ 0 & \eta_y & 0 \\ \zeta_x & \zeta_y & \zeta_z \end{vmatrix} = \xi_x \eta_y \zeta_z = \zeta_z. \quad (2)$$

Several strategies are available for building the computational mesh in physical space. Most often we employ simple algebraic stretching (e.g., Anderson et al., 1984, see page 358). This technique builds a smoothly varying mesh along each vertical coordinate line. The stretching factor $K = \Delta z_{k+1} / \Delta z_k$ is the grid spacing ratio between neighboring k and $k+1$ vertical gridpoints. A typical value is $K \sim 1.03$ or less when $\Delta z_1 = 1$ m and the top of the domain is 1000 m and the number of vertical gridpoints $N_z = 256$.

2.3 LES equations in curvilinear coordinates

The LES equations in curvilinear coordinates can be derived in a straightforward fashion by applying the chain rule for differentiation. The set of LES equations written in computational coordinates under the transformation (1) and (2) are:

$$\frac{\partial U_i}{\partial \xi_i} = 0 \quad (3a)$$

$$\frac{1}{J} \frac{\partial \bar{u}_i}{\partial t} + \frac{\partial}{\partial \xi_j} U_j \bar{u}_i = \mathcal{F}_i \quad (3b)$$

$$\frac{1}{J} \frac{\partial \bar{\theta}}{\partial t} + \frac{\partial}{\partial \xi_j} U_j \bar{\theta} = \mathcal{M} \quad (3c)$$

$$\frac{1}{J} \frac{\partial e}{\partial t} + \frac{\partial}{\partial \xi_j} U_j e = \mathcal{R} \quad (3d)$$

$$\frac{\partial}{\partial \xi_i} \left[\frac{1}{J} \frac{\partial \xi_i}{\partial x_j} \frac{\partial \xi_m}{\partial x_j} \frac{\partial \Pi}{\partial \xi_m} \right] = \mathcal{S} \quad (3e)$$

The equations are expressed in strong conservation form using the “contravariant flux” velocity

$$U_i = \frac{\bar{u}_j}{J} \frac{\partial \xi_i}{\partial x_j}. \quad (4)$$

(3a) is the mass conservation (continuity) equation, (3b) is the momentum transport equation, (3c) is the scalar transport equation, (3d) is the subgrid-scale energy transport equation, and (3e) is the pressure Poisson equation. The right hand sides of (3) model physical processes in the atmospheric PBL, e.g., pressure gradients, Coriolis rotation, divergence of subgrid-scale fluxes, buoyancy, and in the case of the SGS e equation also diffusion and dissipation.

A key step in this formulation is co-locating the solution variables $(\bar{\mathbf{u}}, \Pi, \bar{\theta}, e)$ at cell centers (Sullivan et al., 2000, 2008) which leads to a simple compact differencing stencil. In order to maintain tight velocity-pressure coupling the flux velocities (U, V) are located at cell centers while W is located at a cell face. This mimics the variable layout in our usual staggered code with a flat bottom. As in Sullivan et al. (2008) we use momentum interpolation to construct the intermediate right hand sides for the flux velocities. Formally, the equation set (3) has the same structure as in the case with a flat lower boundary and thus similar spatial and temporal discretizations are used to advance them forward in time. Thus the spatial differencing is pseudospectral in the horizontal computational directions (ξ, η) and second-order finite differences in the ζ -coordinate.

The major algorithmic change, compared to the flat LES code, is the pressure formulation. As a consequence of the incompressible flow assumption and the non-orthogonal mesh we are forced to solve a general

Poisson equation (3e) for pressure. A direct solution of (3e) is not possible. Inspection of (3a) and (3e) suggests the stationary iteration scheme

$$\mathcal{D}(\Pi^{i+1}) = \mathcal{D}(\Pi^i) - \frac{1}{\Delta t} \frac{\partial}{\partial \xi_j} U_j(\Pi^i) \quad (5)$$

for Π where Δt is the timestep the superscript i is an iteration index and the operator \mathcal{D} is an approximate diagonalization of the operator \mathcal{A} : \mathcal{A} is the complete left hand side of (3e). At convergence $\mathcal{D}(\Pi^i) = \mathcal{D}(\Pi^{i+1})$ and (5) numerically satisfies mass conservation. (5) is designed so that it can be easily inverted using a combination of 2D Fast Fourier Transforms and tridiagonal matrix inversions. Furthermore it nicely maps onto our 2D MPI parallelization.

The algorithm outlined above is a significant advance over our previous scheme (Sullivan et al., 2000, 2008). It uses a more general grid transformation that permits 3D lower boundary shapes, it has a more general and robust pressure solver, and it has an improved treatment of the surface boundary conditions. We have used as many as 4096 computational cores for high resolution simulations, $(1024 \times 384 \times 256)$ gridpoints, with the above scheme. Further details of the algorithm including the posing of the rough wall boundary conditions will be described in a future publication.

3. SIMULATION STRATEGY

A series of LES are performed to highlight the interactions between small-scale terrain and PBL turbulence and to exercise the code for both two-dimensional and three-dimensional surface shapes. In these computations, we simplify the external forcing compared to an atmospheric PBL, *i.e.*, we drive the flows with a constant large-scale pressure gradient \mathcal{P}_x/ρ oriented along the x -direction and turn off buoyancy influences. Hence the simulations are similar in spirit to a wind tunnel configuration. The lower surface is assumed to be fully rough and we impose z_o boundary conditions based on the winds at the first gridpoint off the surface (*e.g.*, Møeng, 1984).

The simulations with terrain are computationally expensive compared to flat wall LES especially when the slopes of the boundary shape are steep. In these simulations, 20 to 30 iterations of (3e) are required to reduce the residual of the continuity equation (3a) to near machine accuracy. This increases the computational time by a factor of two or more compared to a flat wall simulation. In addition, we use fine mesh resolution $O(m)$ (see below) and thus the timesteps are pushed to small values by the CFL constraint in our shear driven computations. Le and Moin (1991) and Zheng and Petzold (2006) propose fractional step schemes that require only a single

pressure projection step in their multi-stage Runge-Kutta time stepping schemes which would potentially lower the cost of including terrain in an incompressible LES.

To allow efficient simulations of the various flows described in Section 4.2 we adopt the following strategy: 1) the simulations are first carried forward with a flat bottom until the turbulence is fully developed and the horizontally averaged momentum flux profile is linear in z over the computational domain; 2) we then restart the simulation with the curved lower bottom using a data volume archived at late time from the flat wall case. These simulations are then advanced in time until the turbulence is nearly re-cycled through the computational box. Thus our strategy mimics the conditions in a wind tunnel where a boundary-layer first develops over a flat wall and then encounters an obstacle far downstream of the inlet. This simulation technique is hinted at by Gong et al. (1996, see discussion starting on page 24) and allows both spatial averaging over homogeneous directions (*e.g.*, the y -direction) and over a set of realizations. Multiple realizations can be created by simply restarting the terrain simulations using different initial volumes from the flat wall case. The transient induced by inserting the bottom terrain is short lived and not analyzed. The pressure solver is able to generate incompressible flow in a single timestep after inserting the terrain since it is developed from the discrete version of the continuity equation.

4. SAMPLE RESULTS

4.1 Turbulent flow past two-dimensional shapes

Taylor (1998) provides the variation of form (pressure) drag versus waveslope ak for linearized mean flow models with different turbulent closures. The bumps are two-dimensional (no y variation) with shape $h = a \cos 2\pi x/\lambda$: the wavelength λ and wavenumber k are related by $\lambda = 2\pi/k$. We re-plot their results in figure 2. At low waveslope, $ak < 0.17$, the theoretical results are nearly independent of the closure. Above $ak > 0.3$ the bumps are steep and the linearized calculations tend to breakdown.

We perform 3D LES of a similar turbulent boundary-layer flow over 2D sinusoidal bumps using a modest grid mesh of $(256, 256, 128)$ gridpoints with a relatively small surface roughness $\lambda/z_o = 5 \times 10^5$. The computations are carried out for four different waveslopes $ak = (0.1, 0.25, 0.35, 0.5)$. At low ak the LES values closely match the linearized calculations. The LES continues to work smoothly for waveslopes as large as 0.5 (this is the largest value tested). An additional LES with a relatively large surface roughness $\lambda/z_o = 1 \times 10^3$ is also shown in figure 2. This value of roughness causes large flow separation with flow reattachment on the forward

face of the upstream wave. This is clearly observed in the visualization of the pressure contours and flow vectors. It is interesting that the pressure drag for the small and large roughness are almost identical. We find that in the large roughness case the flow above the bumps tends to skip from crest-to-crest with relatively slow recirculating flow in the wave troughs. In the small roughness (non-separated) case the wave signature is clearly visible in the vertical velocity field but is destroyed by vigorous turbulence generated by flow separation in the large roughness case (see figure 2).

4.2 Turbulent flow past three-dimensional shapes

Hills, ridges, bluffs, land-sea escarpments, *etc.* tend to generate a local speedup in the boundary-layer winds and thus are potential targets for wind turbine sites (see figure 1). Often these orographic features are geometrically complex and 3D, *i.e.*, with their characteristic horizontal lengths and widths of similar scale. Thus it is important to examine the structure of the boundary-layer winds in the presence of 3D obstacles.

We compute turbulent flow over and around three canonical shapes, *viz.*, a hill, gap, and crater. This demonstrates the LES code's ability to handle modestly complex 3D orography and further illustrates the rich level of fluid dynamical phenomenon generated by the interactions between boundary-layer turbulence and small-scale landscape features. In the following sections, the boundary-layer flows are created using the strategy described in Section 3. The simulation with a flat wall is first run for about 130,000 timesteps which is ~ 7 large eddy turnover times. Each simulation uses a unique lower-bottom shape and generates a terrain following grid using smooth vertical grid stretching. The computational box $(L_x, L_y, L_z) = (2560, 640, 1000)$ m the number of gridpoints in the three coordinate directions $(N_x, N_y, N_z) = (1024, 256, 256)$ and the horizontal spacing $(\Delta x, \Delta y) = (2.5, 2.5)$ m. The vertical spacing is 1 m at the surface and smoothly increases to the top of the box. Approximately 40 gridpoints are located in the first 50 m above the surface. The large-scale pressure gradient is set to $\mathcal{P}_x/\rho = 1.63 \cdot 10^{-4} \text{ m s}^{-2}$ which generates winds of about 10.5 m s^{-1} at the top of the box. The surface roughness $z_o = 0.05$ m. The flow blockage is small since $h/L_z < 0.05$ everywhere.

4.2.1 Isolated hill

An isolated 3D hill (see figure 3) is positioned in the simulation with its summit located at $(x_c, y_c) = (1280, 320)$ m. Geometrical properties of the cosine shaped hill are: summit height of 50 m, maximum slope of 0.6, characteristic length scale $\mathcal{L} = 67$ m, and the max-

imum $x - y$ planform is approximately a circle of diameter equal to $4\mathcal{L} = 268$ m. The shape of the hill is

$$h(x', y') = \frac{b}{2} \left(1 + \cos \frac{2\pi x'}{4\mathcal{L}} \right) \left(1 + \cos \frac{2\pi y'}{4\mathcal{L}} \right) \quad (6)$$

where $b = 25$ m, $\mathbf{x}' = \mathbf{x} - \mathbf{x}_c$, and $(|x'|, |y'|) < 2\mathcal{L}$.

Figure 3 shows an instantaneous snapshot of typical flow features that develop around the steep isolated hill. The overall impression is that these flow patterns are unique compared to a 2D case with similar characteristic length scale \mathcal{L} and maximum slope. First, a complex flow separation pattern is generated – there is flow separation over the hill crest as in the 2D case but separation also occurs along the flanks of the hill. The region of intense low pressure along the hill crest is confined to a distance of about $2.5\mathcal{L}$ in the y -direction. Animations show that the spanwise pressure pattern along the line $x' = 0$ is occasionally interrupted by tongues of low pressure that arc around the hill sides in a crescent shape.

The most striking feature of this simulation however is the complex multi-scale wake flow that develops aft of the hill. It is a collection of temporally evolving vortices with their primary axis aligned with z . At any time there can be multiple vortices of various scales present but often two larger vortices dominate the wake as shown in figure 3. There is a strong return flow along the line $y' = 0$ separating the two vortices. Notice also that the location of the vortices is well downstream of the hill summit near the boundary where the hill flattens out and blends into the flat surface; this is clearly downwind of the region of maximum hill slope. Note we are using low pressure as a criterion for vortex identification, see Lin et al. (1996) for a comparison of methods. The coherent rotation of the surface velocity vectors is additional evidence that the regions of low pressure are indeed vortical cores. Broadly, the mean flow patterns shown in figure 3 are similar to the early stage of a flow around a barchan sand dune described by Ortiz and Smolarkiewicz (2009), and the flow measurements around an axisymmetric bump reported by Byun and Simpson (2006).

4.2.2 Gap flow

Flows in gaps separating ridges and hills are a common landscape feature. The ability of the LES to simulate this type of turbulent flow is shown in figure 4. The shape of the terrain is

$$h(x', y') = \begin{cases} \frac{b}{2} \left(1 + \cos \frac{2\pi x'}{4\mathcal{L}} \right) F(y') & : |x'| < 2\mathcal{L} \\ 0 & : |x'| > 2\mathcal{L} \end{cases} \quad (7)$$

where the spanwise extent and depth of the gap are controlled by the function

$$F(y') = \begin{cases} \frac{1}{2} \left(1 - \cos \frac{2\pi y'}{4\mathcal{L}}\right) & : |y'| < 2\mathcal{L} \\ 1 & : |y'| > 2\mathcal{L} \end{cases} \quad (8)$$

Figure 4 illustrates the speedup of the u -component of the horizontal wind in a narrow gap. Notice the speedup is largest in the region where the ridge begins to blend into the gap floor, *i.e.*, along the sides of the gap. Visualization of the pressure field shows a similar feature where the low pressure contours are most negative on the slope approaching the valley and then become less negative away from the gap. The pattern is asymmetric in time shifting from side-to-side in the gap. This is slightly surprising since the initial expectation is that the winds along the gap centerline would be highest. The vertical $y-z$ planes illustrate the vigorous flow separation aft of the two ridges.

4.2.3 Crater flow

Boundary-layer flows in and above open and closed basins are of importance for a variety of applications, *e.g.*, diffusion of pollutants. The recent METCRAX field campaign (Whiteman and CoAuthors, 2008) focused on the complex flow patterns generated by stably-stratified flow in a closed basin. In figure 5 we show an example of the LES code's capability to simulate neutrally stratified flow in an idealized closed crater whose shape h is given by the negative of (6). The nominal diameter is $4\mathcal{L} = 400$ m, the depth equals 50 m, and the maximum slope equals 0.39. The crater center $(x_c, y_c) = (1280, 320)$ m.

The instantaneous snapshot of the flowfield in figure 5 shows several interesting and complex features. The negative (low) pressure contours are indicators of small-scale vortices located near the crater. Animations show a rapid evolution of these vortical structures in the crater interior. The high pressure contours are indicators of the fluctuating re-attachment along the crater backwall and the very negative pressure contours around the crater rim are due to flow accelerations around the crater lip. Visualization in $x-z$ planes along the crater centerline show intermittent ejections of fluid into the overlying boundary-layer flow. We mention that strong convergence of surface streamlines, *e.g.*, as observed at $(x, y) = (1350, 250)$ m in figure 5, is often an indicator of 3D flow separation (*e.g.*, Byun and Simpson, 2006). The flow patterns inside the crater are clearly distinct from those generated behind an isolated hill in figure 3.

5. SUMMARY

A massively parallel algorithm and code for large-eddy simulation (LES) of atmospheric planetary bound-

ary layers (PBLs) with modestly complex orography is described. Our LES model equations adopt an incompressible Boussinesq flow model with high Reynolds number rough wall boundary conditions along the lower boundary. A co-located variable layout and a conventional coordinate transformation from physical to computational space are used. The grid mesh in physical space is terrain following and non-orthogonal, a more general formulation can be incorporated into the scheme. The key new step compared to a flat wall code is the formulation of the pressure equation and designing an algorithm for the solution of the pressure Poisson equation. The algorithm is sufficiently general to allow simulations of PBLs over a spectrum of time dependent moving water waves (Sullivan et al., 2010). We present several sample calculations of neutrally-stratified turbulent flow, (similar to a wind-tunnel setup) past 2D sinusoidal bumps and 3D obstacles, *viz.*, a hill, gap, and crater. These calculations highlight the importance of flow separation and coupling with background PBL turbulence, and the ability of the algorithm to simulate turbulent flows with an undulating lower boundary.

In the future we plan to implement an algebraic stress closure model for subgrid-scale fluxes and variances (Wyngaard, 2004) and validate the code against the wind-tunnel measurements of Ayotte and Hughes (2004), and Gong et al. (1996), and field observations. Also, PBL simulations will be carried out with unstable and stable stratification. The fine mesh large-eddy simulations described here can be used in two ways: 1) they provide insight about the fundamental interactions between turbulence and terrain which can impact isolated wind turbines and wind parks; and 2) the detailed datasets can be used for building parameterizations of separated flows.

Acknowledgments: We thank Jeff Weil for his contributions to this work. P. Sullivan is partially supported by the Office of Naval Research, Physical Oceanography program and by the National Science Foundation through the National Center for Atmospheric Research. E. Patton is supported by the Army Research Office and NCAR. This research used resources of the National Energy Research Scientific Computing Center, which is supported by the Office of Science of the U.S. Department of Energy under Contract No. DE-AC02-05CH11231, NCAR and the Department of Defense High Performance Computing. Any opinions, findings, and conclusions or recommendations expressed in this publication are those of the author(s) and do not necessarily reflect the views of the National Science Foundation.

REFERENCES

- Anderson, D. A., J. C. Tannehill, and R. H. Pletcher, 1984: *Computational Fluid Mechanics and Heat Transfer*, McGraw-Hill, 599 pp.
- Ayotte, K. W., 2008: Computational modeling for wind energy assessment, *Journal of Wind Engr. and Industrial Aerodynamics*, **96**, 1571–1590.
- Ayotte, K. W. and D. E. Hughes, 2004: Observations of boundary-layer wind-tunnel flow over isolated ridges of varying steepness and roughness, *Boundary-Layer Meteorol.*, **112**, 525–556.
- Banta, R. M., Y. L. Pichugina, N. D. Kelley, B. Jonkman, and W. A. Brewer, 2008: Doppler lidar measurements of the Great Plains low-level jet: Applications to wind energy, in *14th International Symposium for the Advancement of Boundary Layer Remote Sensing*, volume 1 of *IOP Conf. Series: Earth and Environmental Science*, pp. 1–5, IOP Publishing.
- Beare, R. J., M. K. Macvean, A. A. M. Holtslag, J. Cuxart, I. Esau, J.-C. Golaz, M. A. Jimenez, M. Khairoutdinov, B. Kosovic, D. Lewellen, T. S. Lund, J. K. Lundquist, A. McCabe, A. F. Moene, Y. Noh, S. Raasch, and P. P. Sullivan, 2006: An intercomparison of large-eddy simulations of the stable boundary layer, *Boundary-Layer Meteorol.*, **118**, 242–272.
- Byun, G. and R. L. Simpson, 2006: Structure of three-dimensional separated flow on an axisymmetric bump, *AIAA Journal*, **44**, 5, 999–1008.
- Gong, W., P. A. Taylor, and A. Dörnbrack, 1996: Turbulent boundary-layer flow over fixed aerodynamically rough two-dimensional sinusoidal waves, *J. Fluid Mech.*, **312**, 1–37.
- IEC, 2005: Wind turbines - Part 1 design requirements, Technical Report IEC 61400-1, third edition, International Electromechanical Commission, Geneva, Switzerland.
- Kelley, N., M. Shirazi, M. Buhl, D. Jager, S. Wilde, J. Adams, J. Bianchi, P. Sullivan, and E. Patton, 2003: Lamar low-level jet project interim report, Technical Report NREL/TP-500-34593, National Renewable Energy Laboratory, Golden, CO.
- Le, H. and P. Moin, 1991: An improvement of fractional step methods for the incompressible Navier-Stokes equations, *J. Comp. Phys.*, **92**, 369–379.
- Lin, C.-L., J. C. McWilliams, C.-H. Moeng, and P. P. Sullivan, 1996: Coherent structures and dynamics in a neutrally stratified planetary boundary layer flow, *Phys. Fluids*, **8**, 2626–2639.
- Moeng, C.-H., 1984: A large-eddy simulation model for the study of planetary boundary-layer turbulence, *J. Atmos. Sci.*, **41**, 2052–2062.
- Ortiz, P. and P. K. Smolarkiewicz, 2009: Coupling the dynamics of boundary layers and evolutionary dunes, *Physical Review E*, **79**, 041307, 1–11.
- Schreck, S., J. Lundquist, and W. Shaw, 2008: U.S. Department of energy workshop report: Research needs for wind resource characterization, Technical Report NREL/TP-500-43521, National Renewable Energy Laboratory, Golden, CO.
- Spalart, P. R., R. D. Moser, and M. M. Rogers, 1991: Spectral methods for the Navier-Stokes equations with one infinite and two periodic directions, *J. Comp. Phys.*, **96**, 297.
- Sullivan, P. P., J. B. Edson, T. Hristov, and J. C. McWilliams, 2008: Large eddy simulations and observations of atmospheric marine boundary layers above non-equilibrium surface waves, *J. Atmos. Sci.*, **65**, 1225–1245.
- Sullivan, P. P., J. C. McWilliams, and T. Hristov, 2010: A large eddy simulation model of high wind marine boundary layers above a spectrum of resolved moving waves, in *19th Amer. Meteorol. Soc. Symp. on Boundary Layer and Turbulence*, Keystone, CO.
- Sullivan, P. P., J. C. McWilliams, and C.-H. Moeng, 1996: A grid nesting method for large-eddy simulation of planetary boundary layer flows, *Boundary-Layer Meteorol.*, **80**, 167–202.
- , 2000: Simulation of turbulent flow over idealized water waves, *J. Fluid Mech.*, **404**, 47–85.
- Sullivan, P. P. and E. G. Patton, 2010: The effect of mesh resolution on convective boundary-layer statistics and structures generated by large-eddy simulation, *J. Atmos. Sci.*, **submitted**.
- Taylor, P. A., 1998: Turbulent boundary-layer flow over low and moderate slope hills, *Journal of Wind Engr. and Industrial Aerodynamics*, **74–76**, 25–47.
- Whiteman, C. D. and CoAuthors, 2008: METRCRAX 2006: Meteorological experiments in Arizona’s meteor crater, *Bull. Amer. Meteorol. Soc.*, **89**, 127–150.
- Wyngaard, J. C., 2004: Toward numerical modeling in the Terra Incognita, *J. Atmos. Sci.*, **61**, 1816–1826.

Zheng, Z. and L. Petzold, 2006: Runge-Kutta-Chebyshev projection method, *J. Comp. Phys.*, **219**, 976–991.

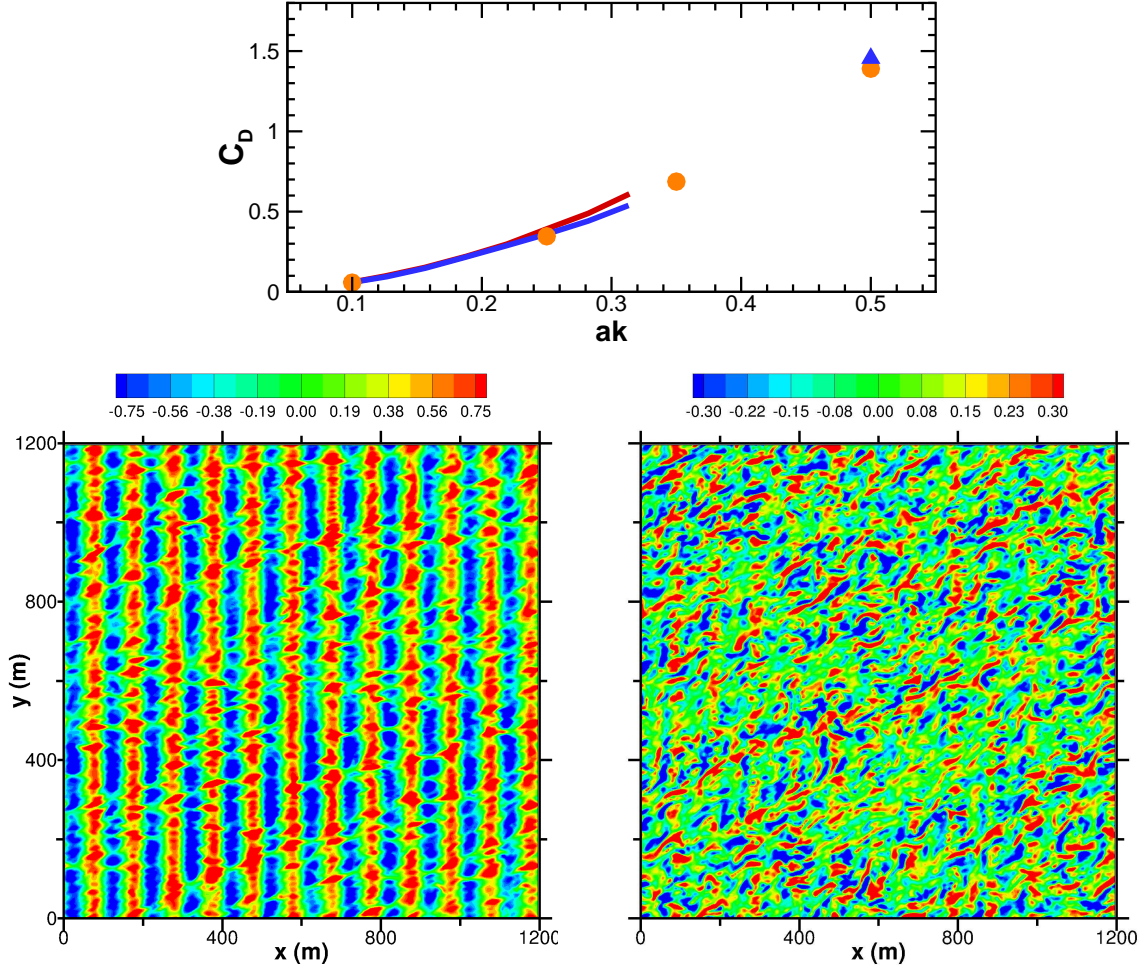


Figure 2: Turbulent flow over 2D sinusoidal bumps. The upper panel shows the pressure drag coefficient C_D as function of waveslope. C_D is obtained from integration of the pressure-waveslope correlation and is normalized by the friction velocity squared u_*^2 . The lines are theoretical predictions from linearized calculations with different turbulence closures at a small roughness $\lambda/z_o = 10^4$ from Taylor (1998). The orange solid bullets are results from LES with a similar small surface roughness $\lambda/z_o = 5 \times 10^5$. The blue triangle is an LES with large surface roughness $\lambda/z_o = 1 \times 10^3$ which leads to extensive flow separation between the wave crests. The lower panels are visualization of vertical velocity w at a nominal height of $z = 10$ m above the bumps at waveslope $ak = 0.5$ from LES. The left and right panels are small and large roughness $\lambda/z_o = (5 \times 10^5, 1 \times 10^3)$, respectively. The color bar is in units of m s^{-1} and is different between the two plots.

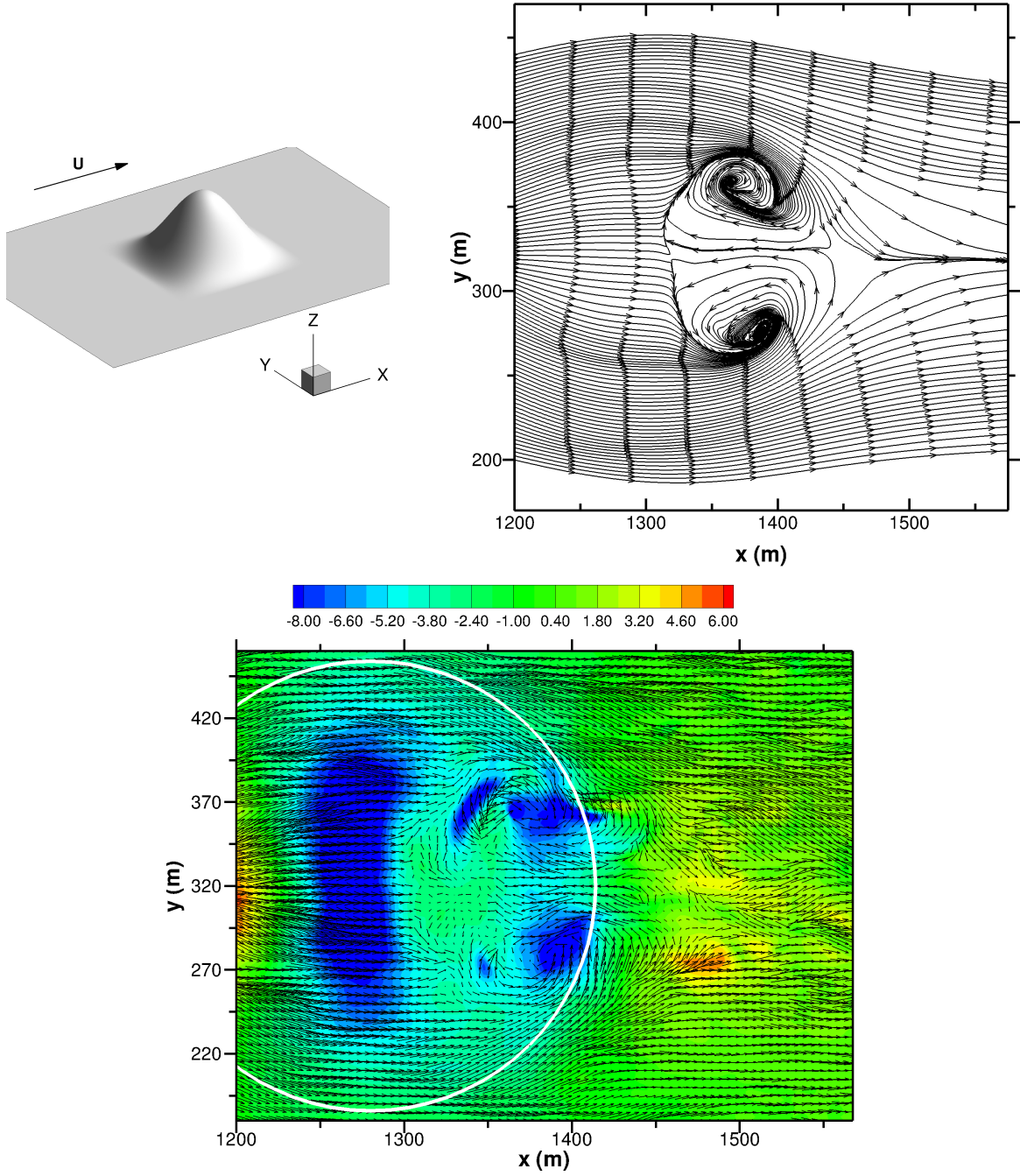


Figure 3: Turbulent flow around a steep 3D hill. The upper left panel shows an oblique view of the hill with the primary flow direction parallel to the x -direction. In the upper right panel we show the time averaged streamline patterns around the hill at the height $z = 5.6$ m. In the lower panel we show color contours of fluctuating pressure p'/ρ overlaid with horizontal flow vectors at a nominal height of $z = 5.6$ m above the hill surface. The color bar is in units of m s^{-2} . The planform of the hill (*i.e.*, the location where the cosine shaped hill blends into the flat bottom boundary) is approximately indicated by the circular white line. The hill summit $h = 50$ m is located at $(x_c, y_c) = (1280, 320)$ m.

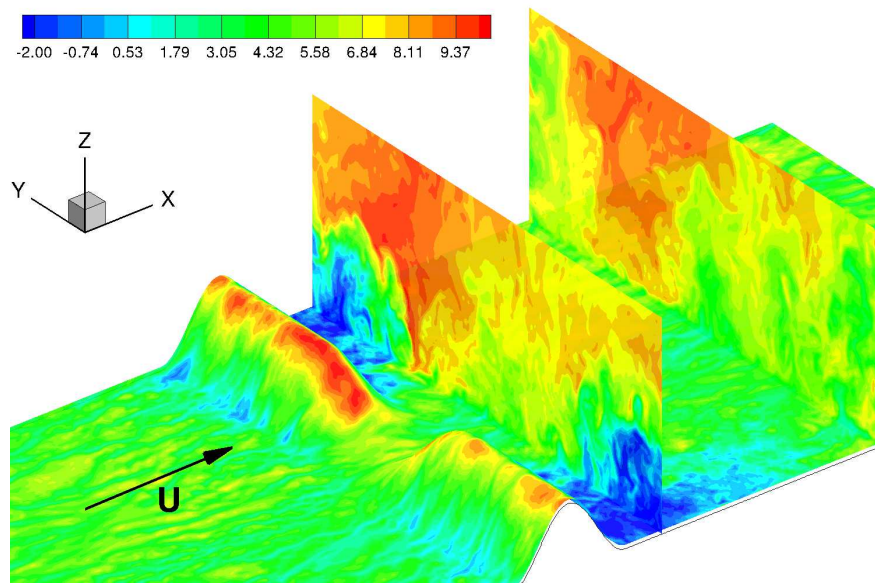


Figure 4: Turbulent flow in a gap between two steep ridges. The primary flow direction is parallel to the x -direction. Contours of the instantaneous u -velocity component are shown and the color bar is in units of m s^{-1} . The two $y-z$ planes are located at $x = (1500, 2000)$ m, and the ridgeline is located at $x = 1280$ m. The horizontal plane is about 4 m off the surface. The lower 150 m of the boundary layer is depicted.

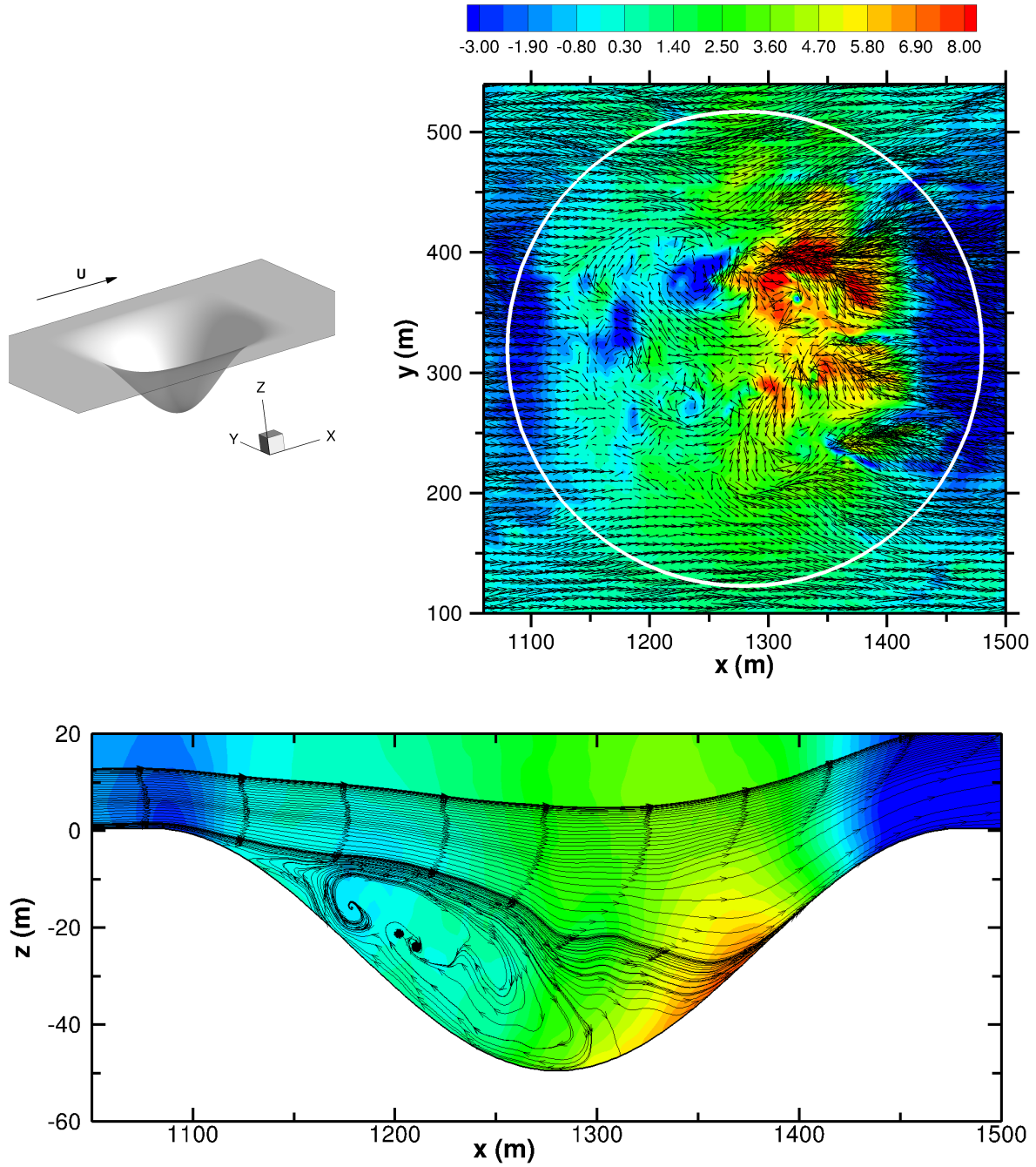


Figure 5: Neutrally stratified turbulent flow in a crater: The upper left panel is an oblique view of the crater geometry. The upper right panel shows instantaneous static pressure contours p'/ρ and horizontal velocity vectors at a nominal height of $z = 2.5$ m above the surface. The white circle is approximately the outline of the crater rim. The color bar is in units of m s^{-2} . The bottom panel is a 150 s time average of the streamlines and pressure field in an $x - z$ plane along the crater centerline.

Large Eddy Simulations of High Wind Atmospheric Boundary Layers Above a Spectrum of Resolved Moving Wind Waves

Peter P. Sullivan* and Edward G. Patton

Mesoscale & Microscale Meteorology Division, National Center for Atmospheric Research

A computational proposal to the NCAR Strategic Capability (NSC) program

Total Computational Hours Requested: 12.0×10^6 core hours

B. Scientific objectives

Momentum and scalar fluxes at the air-sea interface depend on numerous small and large scale processes that couple atmospheric turbulence and the underlying surface gravity wave field (Sullivan and McWilliams, 2010). The surface wave field moves randomly, propagates rapidly, breaks intermittently, and supports wind stress. Wind-wave coupling determines the sea surface drag, and at high winds provides $\mathcal{O}(1)$ control on hurricane intensity. Despite intense study, the present understanding of wind-wave coupling is incomplete and hence our ability to predict high wind storm dynamics, such as hurricanes, is limited (Emanuel, 2004; Sanford et al., 2011). A fundamental unresolved observational challenge is determining the correlation between surface pressure and wave slope (form drag) near an undulating air-water interface with breaking waves.

Our past modeling using direct numerical and large-eddy simulations (DNS and LES) over an idealized monochromatic surface wave have provided insight about wind-wave coupling processes, *e.g.*, critical layer dynamics, wave driven winds, the transport of fluxes in non-equilibrium wind-wave conditions and the impact of wave state on the marine boundary layer (Sullivan et al., 2000; Sullivan and McWilliams, 2002; Sullivan et al., 2008). These simulation results have also aided the interpretation of observations. The computational project proposed here builds on these past efforts but is a significant advancement as it seeks to examine the coupling between stratified atmospheric turbulence in a high wind marine boundary layer and a spectrum of phase-resolved surface waves using newly developed large-eddy simulation technology. The high-wind flow regime of interest represents a severe computational challenge as it couples atmospheric turbulence and 3D moving surface wave fields over a wide range of scales, $\mathcal{O}(1 - 1000)$ m. The very high spatial and temporal resolution of the proposed simulations will provide information about the impacts of the wave field on drag, turbulence fluxes and variances, mean wind profiles, and coherent structures. The proposed project is an integral component of the High Resolution Air-Sea Interaction (Hi-Res) observational study shown in Fig. 1. Hi-Res sampled the spatial and temporal evolution of the wave fields and near surface boundary layer extensively at wind speeds varying from 10-20 ms^{-1} . A longer term objective of the proposed project is to use simulation data to compare with and more fully interpret observations collected in Hi-Res.

Our computational project supports ongoing research funded by the Physical Oceanography Program at the Office of Naval Research and the Department of Energy. Also, the proposed project addresses the NCAR Imperative and Frontiers on prediction of severe weather and winds for renewable energy[†], and the NCAR Wyoming Supercomputer Community Science Objectives “... representation of detailed processes at the air-water interface”, and “... boundary layer modeling for studies of wind energy.”

*Corresponding author address: Peter P. Sullivan, MMM Division, NCAR, Boulder, CO 80307-3000. E-mail: pps@ucar.edu Phone: 303-497-8953

[†]see <http://ncar.ucar.edu/documents/strategic-plan/2009/imperatives-and-frontiers-for-ncar>

C. Computational plan

1. Numerical method

We briefly outline the important aspects of our numerical scheme with moving waves. The governing equations which describe three-dimensional time-dependent turbulent winds in a dry incompressible Boussinesq atmospheric boundary layer include: a) three transport equations for momentum $\rho \bar{\mathbf{u}}$; b) a transport equation for a conserved buoyancy variable (*e.g.*, virtual potential temperature $\bar{\theta}$); c) a discrete Poisson equation for a pressure variable Π to enforce incompressibility; and closure expressions for subgrid-scale (SGS) variables, *e.g.*, a subgrid-scale equation for turbulent kinetic energy e , *e.g.*, see Sullivan and Patton (2011). The physical processes included in the LES boundary-layer equations include, temporal time tendencies, advection, pressure gradients, Coriolis rotation, divergence of subgrid-scale fluxes, buoyancy, resolved turbulence, and in the case of the SGS e equation also diffusion and dissipation.

In order to simulate turbulent flow over a multi-component propagating surface wave field, we have adapted our LES model with a *flat* bottom to the situation with a three-dimensional time-dependent boundary shape $h = h(x, y, t)$ by applying a transformation to the physical space coordinates (x, y, z) that maps them onto computational coordinates (ξ, η, ζ) . The computational mesh in physical space is surface following, non-orthogonal, and time varying. Vertical gridlines are held fixed at a particular (x, y) location on the surface but the lines undergo vertical translation as a function of time t , *i.e.*, vertical gridlines are wave following, see Figs. 2 and 3. The LES equations are expressed in strong conservation form using the “contravariant flux” velocity

$$U_i = \frac{\bar{u}_j}{J} \frac{\partial \xi_i}{\partial x_j} \quad (1)$$

with the advective term for variable ψ evaluated in flux form, *i.e.*, $\partial U_j \psi / \partial \xi_j$. In (1), $(J, \partial \xi_i / \partial x_j)$ are the Jacobian and metric connection functions linking physical and computational space.

A key step in the wavy LES formulation is co-locating the solution variables $(\bar{\mathbf{u}}, \Pi, \bar{\theta}, e)$ at cell centers (Sullivan et al., 2000, 2008) which leads to a simple compact differencing stencil. To maintain tight velocity-pressure coupling the flux velocities (U, V) are located at cell centers while W is located at a cell face. We use so-called momentum interpolation to construct the intermediate right hand sides for the tendencies of the flux velocities. The spatial differencing is pseudospectral in the horizontal computational directions (ξ, η) and second-order finite differences in the ζ -coordinate. The time stepping is a low-storage third-order Runge-Kutta scheme, and the time step δt is picked dynamically based on a fixed Courant-Fredrichs-Lewy (CFL) number.

Compared to our flat LES code, the major algorithmic change is the pressure formulation. As a consequence of the incompressible flow assumption and the non-orthogonal mesh we are forced to solve a general Poisson equation. A direct solution of this elliptic problem is not possible, and thus we use the stationary iteration scheme

$$\mathcal{D}(\Pi^{i+1}) = \mathcal{D}(\Pi^i) - \frac{1}{\delta t} \frac{\partial}{\partial \xi_j} U_j(\Pi^i) \quad (2)$$

for Π^{i+1} , the superscript i is an iteration index and the operator \mathcal{D} is an approximate diagonalization of the full Poisson operator. At convergence $\mathcal{D}(\Pi^i) = \mathcal{D}(\Pi^{i+1})$ and (2) numerically satisfies mass conservation; typically 20 to 30 iterations are required to drive the residual error in (2) to machine accuracy for hard problems. (2) is designed so that it can be easily inverted using a combination of 2D Fast Fourier Transforms (FFTs) and tridiagonal matrix inversions, which nicely maps onto our 2D Message Passing Interface (MPI) parallelization, see Fig. 5.

The time dependence of the grid modifies the LES equations: the Jacobian $J(\mathbf{x}, t)$ appears inside the time tendency of each transport equation and advection contains a contribution from the grid movement, *i.e.*, the total vertical flux of variable ψ depends on the difference $(W - z_t)\psi$ where z_t is the grid speed. As a consequence of writing the equations in strong conservation form, we determine the grid speeds based on the discrete solution of $\partial J / \partial t = \partial z_t / \partial \zeta$, which is a simplified form of the geometric conservation law first discussed by Thomas and Lombard (1979). This prevents artificial sources and sinks from developing in the computational domain.

The MPI algorithm utilizes the 2D brick decomposition shown in Fig. 5. This scheme allows freedom in choosing the horizontal and vertical decompositions and allows simulations with a high degree of spatial anisotropy, *i.e.*, when the computational box is wide with small vertical extent. The algorithm relies on matrix transposes to carry out the global FFT and tridiagonal operations. Further details about the LES model and the algorithm are given by Sullivan et al. (2010a,b); Sullivan and Patton (2011).

2. Numerical experiments

For our project we propose carrying out the 7 simulations listed in Table 1; included in this table is an estimate of the computational resources required. These simulations allow us to quantify the effects of thermal stratification and a change in wind speed on the turbulent flow in and around the wave field. We also propose a stationary bump case, *i.e.*, the wave fields will be frozen in time so that they correspond to stationary resolved roughness which will further expose the influence of wave motion. All the numerical experiments will be conducted in domains $(L_x, L_y, L_z) = (1200, 1200, 800)$ m using meshes of $(N_x, N_y, N_z) = (1024, 1024, 512)$ gridpoints. The grid spacing in the horizontal directions is constant $\Delta x = \Delta y = 1.17$ m while the vertical grid is stretched to allow fine resolution near the wavy surface; $\Delta z = 0.5$ m or less at the surface. More than 370 gridpoints are then distributed between the water surface and the boundary-layer inversion. For the first 5 simulations in Table 1, the large scale winds will be held fixed at $U_g = 20$ m s⁻¹ and the surface buoyancy will be varied to generate cases with neutral, unstable and stable stratification to match the conditions in the Hi-Res field campaign (Fig. 1). Simulation *N10* will use the same wavefields as *N20* but the large-scale winds will be reduced to 10 m s⁻¹ to generate a swell dominated condition, a commonly observed ocean state. Based on previous simulations, the impact of wave age and swell on the atmosphere are pronounced as shown in Fig. 4.

The computational strategy we will adopt is to first carry out simulations with a flat stationary lower boundary (*F20*, *F10*) so as to develop near equilibrium 3D turbulence. 3D volumes from this seed simulation will then be used to spawn simulations with different combinations of wind, stratification, and waves. This strategy makes effective use of the computational resources since the LES code with a flat lower boundary runs between 2 ~ 3 times faster than the code with moving waves. Hence it is most efficient to spinup boundary-layer turbulence in the presence of a flat lower boundary.

3. Computational resources required

To estimate the core-hours \mathcal{C} required by a simulation we use the formula $\mathcal{C} = N_{cores} \times \Delta t \times N_{steps} / 3600.0$ where N_{core} is the number of cores, Δt is the core seconds required per computational step and N_{steps} is the number of steps required for producing equilibrium turbulence. On the Cray XE6 *Garnet*[‡] with a mesh of $512^2 \times 128$ using 512 cores the code $\Delta t \approx 5.4$ core-seconds/step. The number of time steps needed to achieve 6 large eddy turnover times is 105,000 and thus $\mathcal{C} = 80,640$ core-hours. To estimate the computational cost for the much higher resolution simulations on *Yellowstone* we increase the *Garnet* estimate by a factor of 39.5. This

[‡]Details about *Garnet* can be found at <http://www.erdhpc.mil/hardware/index.html>.

Table 1: Summary of proposed simulations

Run	Comment	Core-hour 10^6	Disk space TB	Archive space TB
<i>N20</i>	neutral stratification, 20 m/s	1.6	1.5	4.5
<i>S20</i>	stable stratification, 20 m/s	1.6	1.5	4.5
<i>U20</i>	unstable stratification, 20 m/s	1.6	1.5	4.5
<i>B20</i>	neutral stratification, bumps	1.6	1.5	4.5
<i>F20</i>	neutral stratification, flat wall, 20 m/s, used for initial conditions	1.6	1.5	4.5
<i>N10</i>	neutral stratification, 10 m/s	1.6	1.5	4.5
<i>F10</i>	neutral stratification, flat wall, 10 m/s, used for initial conditions	1.6	1.5	4.5

accounts for the increase in resolution (factor of 19.75 that includes the FFT scaling $N \log N$) and reduction in allowable time step due to the CFL constraint (factor of 2). We then reduce this estimate by a factor of 2 assuming *Yellowstone* is twice as fast as *Garnet*. Thus a single simulation on *Yellowstone* consumes $\mathcal{C} = 80,640 \times 39.5/2 = 1.6 \times 10^6$ core-hours. The total computational cost of the 7 simulations is then $\sim 12.0 \times 10^6$ core-hours.

D. Code requirements and production-readiness

1. Code to be used

The in-house NCAR wavy LES code is tested and production ready on large parallel supercomputers. We routinely use the wavy LES code on the three major supercomputer platforms, IBM, SGI, and Cray all with different compilers: *e.g.*, NCAR IBM (*Bluefire*) with the mpixlf90 compiler; ERDC SGI Altix Ice (*Diamond*) with the ifort compiler; the ERDC Cray XE6 (*Garnet*) with the pgf90 compiler. The LES code is robust across different platforms, and its compliance to the F90 standard and the use of the most common functions in the MPI libraries allows the code to be ported to new machine architectures quickly. A flat version of the LES code (no wavy boundaries) was one of the benchmark codes used in the procurement for the NCAR Wyoming Supercomputer Center, and hence we expect the wavy LES code will port to *Yellowstone* in a straightforward manner.

2. Programming environment

The specifics of the programming environment that the LES code utilizes are provided in Table 2. The estimates of the memory usage, wall-clock time, and scratch disk space are based on simulations with $1024^2 \times 512 \approx 540 \times 10^6$ gridpoints.

3. Benchmarks and scalability

The scaling performance of the flat LES code for three different machines for varying workload as a function of the total number of processors NP is documented in Sullivan and Patton (2011). An example of the code scaling is provided in Fig. 6 for the Cray machines at the National Energy Research Scientific Computing Center (NERSC). These timing tests illustrate the present algorithm exhibits strong scaling over a wide range of problem sizes. Note the code is able to use as many as 65,536 processors for a large problem with 3072^3 gridpoints. Generally, the performance only begins to significantly degrade when the number of processors exceeds about 8

Table 2: Programming environment

Programming language:	F90 compliant	Required libraries:	FFTPACK and MPI
Parallel paradigm:	MPI, 2D domain decomposition	Wall-clock time/run:	195 hours on 8192 cores
Estimated cores/run:	4096 or 8192	Scratch disk per run:	1.5 TB
Memory usage/core:	< 2 MB	Restart capability:	Yes, routinely used
		Data I/O:	MPI I/O

times the smallest grid dimension owing to increases in communication overhead. We speculate that the performance degradation at 65,536 processors is a consequence of the small node memory on *Hopper* for the large problem tested, 3072^3 gridpoints. The code also exhibits weak scaling (*i.e.*, where the problem size grows as the number of processors increases so the amount of work per processor is held constant).

Preliminary tests indicate that the wavy LES code scales in a similar manner as the flat code. The wavy LES code is routinely run in production mode with either 512 or 1024 processors on the ERDC machines *Diamond* and *Garnet* for problems with 33×10^6 gridpoints. On *Yellowstone* we expect to routinely use 4096 or 8192 processors for the proposed simulations with 540×10^6 gridpoints.

E. Data analysis and visualization

We typically use Tecplot 360 (<http://www.tecplot.com/>) on our desktop machines. This visualization package allows for building presentation quality animations quickly using 2D planes of data with time dependent moving grids. In the present project we will use Tecplot’s capabilities but will also modify our analysis to use NCAR’s VAPOR package for large 3D visualizations. Also, due to the large size of the data volumes we will alter our usual analysis strategy, leaving more data on the centralized file and data storage resources, and perform extensive analysis and visualization on the *Geyser* and *Caldera* machines.

F. Data management plan

We estimate that our simulations require approximately $5 \sim 8$ TB of working disk space for data analysis and visualization. This includes 2D planes sampled at an adequate temporal resolution for rapid movie making of selected flow variables. In addition, disk space is needed to hold several 3D volumes for conditional sampling and non-routine analysis not conducted on the fly during a simulation. Our long term storage plans rely on keeping several archival 3D volumes that can be used to perform code restarts if further analysis is needed. The LES code builds history files with numerous statistics as function of time, *e.g.*, vertical profiles of winds, fluxes, and variances in addition to point values. These history files are compact and provide a quick look at the simulation data using already built analysis codes.

G. Accomplishment report on prior large allocations

The PIs have worked extensively on IBM, SGI, and Cray supercomputers during the past 10 years. We estimate our current average use at 300,000 Gaus/year on NCAR’s *Bluefire*, more than 2 million core-hours/year at NERSC and 1 to 2 million core-hours/year on DOD machines. These past computational experiments focused on a wide range of LES related topics, *viz.*, air-sea interaction in the marine atmospheric and oceanic boundary layers, turbulent flow in vegetative canopies including chemistry, turbulent dispersion, flow over small-scale topography,

stable boundary layers with surface heterogeneity, and effects of grid resolution on LES solutions. This computational work has produced numerous publications that appear in *Journal of Fluid Mechanics*, *Journal of the Atmospheric Sciences*, *Boundary-Layer Meteorology*, *Journal of Physical Oceanography*, *Journal of Geophysical Research*, and *Annual Review of Fluid Mechanics*. An itemized list of recent publications can be found at <http://www.mmm.ucar.edu/people/sullivan/> and <http://www.mmm.ucar.edu/people/patton/>. The PIs routinely present results from their computational work at scientific meetings and workshops. The PIs research is funded internally by NSF and externally by the Office of Naval Research, the Army Research Office, and the Department of Energy. The PIs regularly collaborate with several university partners; PPS currently serves on 5 PhD thesis committees, *viz.*, University of Colorado (2), Stanford University (1), UCLA (1), and University of Rhode Island (1).

References

- Emanuel, K., 2004: Tropical cyclone energetics and structure. *Atmospheric Turbulence and Mesoscale Meteorology*, E. Fedorovich, R. Rotunno, and B. Stevens, eds., Cambridge University Press, 165–191.
- Sanford, T. B., J. F. Price, and J. B. Girton, 2011: Upper ocean response to Hurricane Frances (2004) observed by profiling EM-Apex floats. *J. Phys. Oceanogr.*, **41**, 1041–1056.
- Sullivan, P. P., J. B. Edson, T. Hristov, and J. C. McWilliams, 2008: Large eddy simulations and observations of atmospheric marine boundary layers above non-equilibrium surface waves. *J. Atmos. Sci.*, **65**, 1225–1245.
- Sullivan, P. P. and J. C. McWilliams, 2002: Turbulent flow over water waves in the presence of stratification. *Phys. Fluids*, **14**, 1182–1195.
- 2010: Dynamics of winds and currents coupled to surface waves. *Annual Review of Fluid Mechanics*, **42**, 19–42.
- Sullivan, P. P., J. C. McWilliams, and T. Hristov, 2010a: A large eddy simulation model of high wind marine boundary layers above a spectrum of resolved moving waves. *19th Amer. Meteorol. Soc. Symp. on Boundary Layer and Turbulence*, Keystone, CO.
- Sullivan, P. P., J. C. McWilliams, and C.-H. Moeng, 2000: Simulation of turbulent flow over idealized water waves. *J. Fluid Mech.*, **404**, 47–85.
- Sullivan, P. P. and E. G. Patton, 2011: The effect of mesh resolution on convective boundary-layer statistics and structures generated by large-eddy simulation. *J. Atmos. Sci.*, **68**, 2395–2415.
- Sullivan, P. P., E. G. Patton, and K. W. Ayotte, 2010b: Turbulent flow over and around sinusoidal bumps, hills, gaps and craters derived from large eddy simulations. *19th Amer. Meteorol. Soc. Symp. on Boundary Layer and Turbulence*, Keystone, CO.
- Thomas, P. D. and C. K. Lombard, 1979: Geometric conservation law and its application to flow computations on moving grids. *AIAA Journal*, **17**, 1030–1037.

H. Figures and captions



Figure 1: Photograph of the Floating Instrument Platform (FLIP) in seas generated by surface winds of 15 to 20 m s^{-1} during the High Resolution Air-Sea Interaction (Hi-Res) field campaign (2009) off the California coast, courtesy E. Terrill Scripps Institution of Oceanography. The goals and description of Hi-Res can be found at <http://airsea.ucsd.edu/hires/>. Hi-Res is supported by the Office of Naval Research.

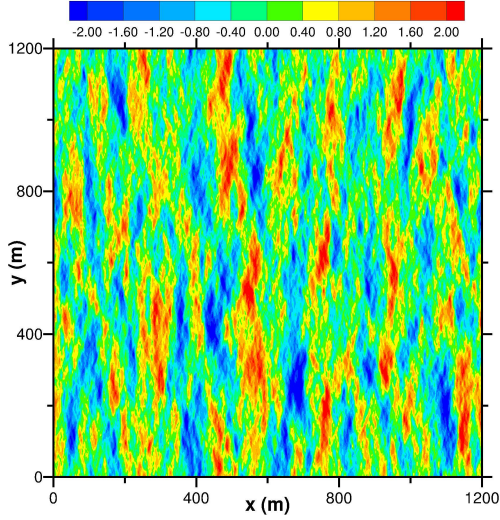


Figure 2: A snapshot of the wavefield height $h(x, y, t)$ that is imposed at the bottom of the LES code in low resolution runs. h is built from a sum of linear plane waves. Waves propagate left to right according to the dispersion relationship. The color bar is in units of meters.

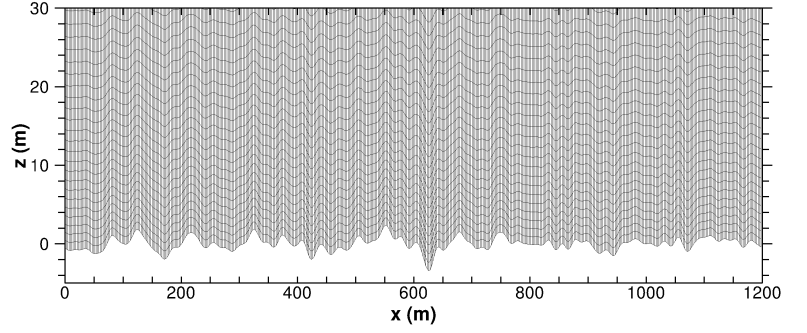


Figure 3: An instantaneous $x - z$ slice of the 3D time varying computational mesh in the lowest portion of the atmospheric boundary layer. The (ξ, η) gridlines become level surfaces at about 100 m above the water. Only a fraction of the grid is displayed.

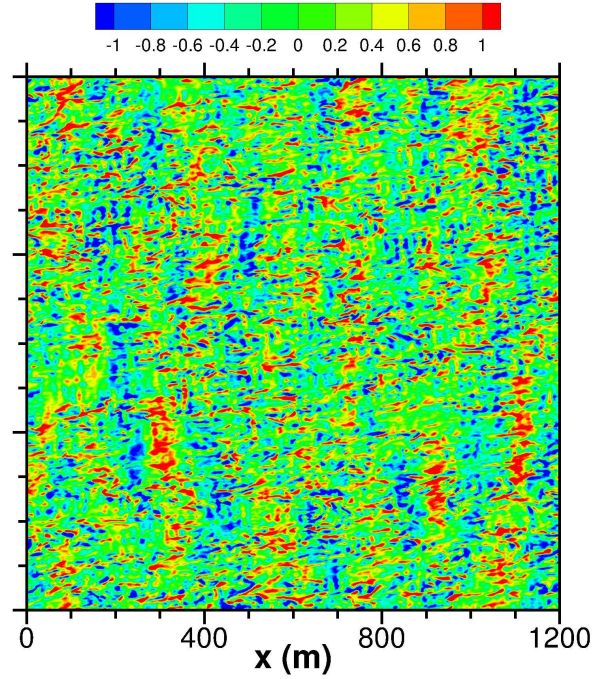
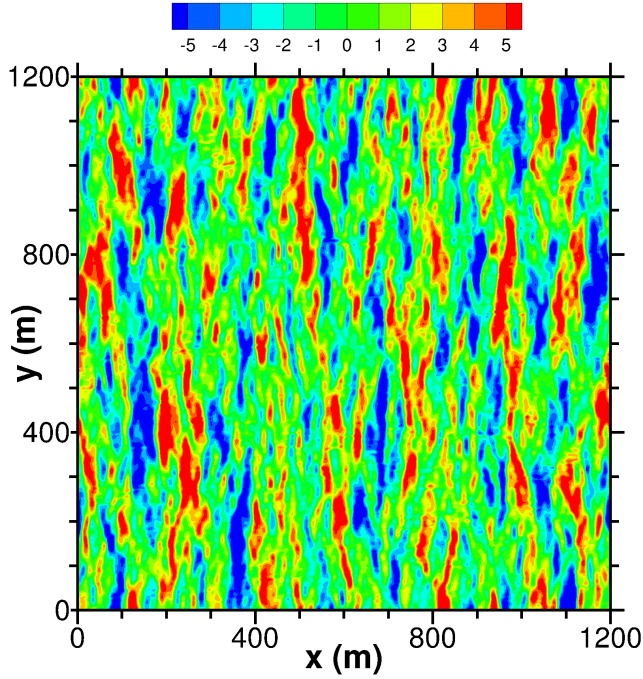


Figure 4: Snapshot of resolved vertical velocity fluctuations w'/u_* in a wave following $x - y$ plane near the water surface $\zeta = 2.5$ m. The left panel is a swell dominated regime while the right panel is a case near wind-wave equilibrium. The wave spectrum at the bottom of the PBLs is the same. Notice the range of the color bar is different between the two cases.

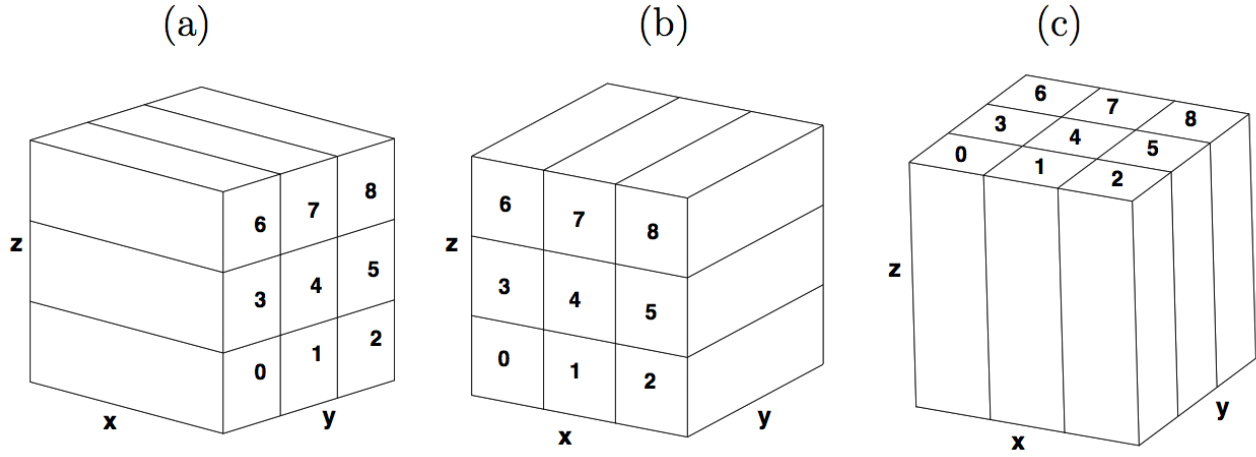


Figure 5: An example of 2D domain decomposition on $NP = 9$ processors. The number of horizontal processors $NP_{xy} = 3$ and the vertical domain is divided into $NP_z = 3$ levels, i.e., the total number of processors $NP = NP_{xy} \cdot NP_z$: (a) base state with $y-z$ decomposition; (b) $x-z$ decomposition used for computation of y derivatives and 2D planar FFT; and (c) $x-y$ decomposition used in the tridiagonal matrix inversion of the pressure Poisson equation.

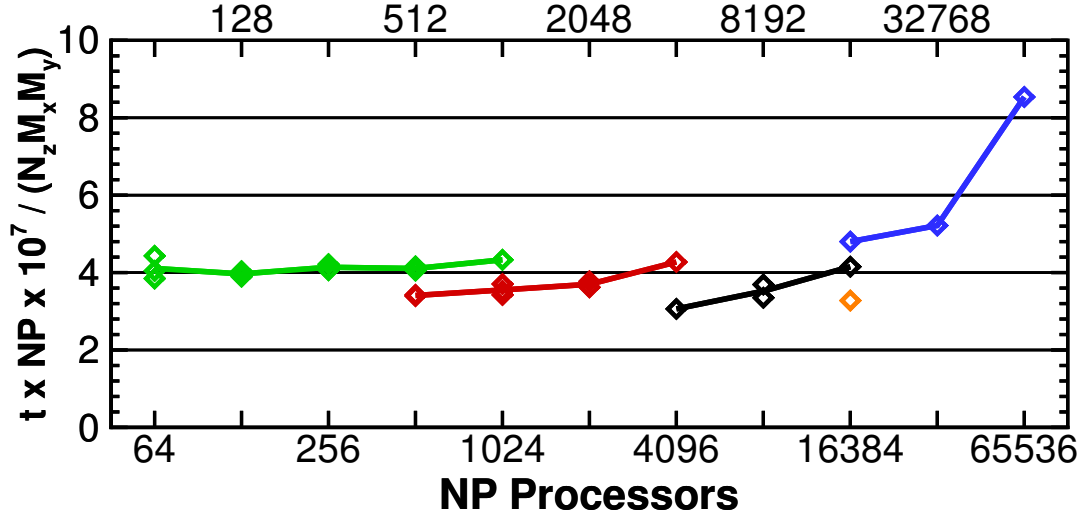


Figure 6: Performance of the NCAR parallel LES code on the NERSC Cray supercomputers, Franklin and Hopper. NP is the total number of processors and the vertical axis is total computational time $t \times NP$ divided by total work. N_z is the number of vertical levels and $M_{x,y}$ is proportional to the FFT work, i.e., $M_{x,y} = N_{x,y} \log N_{x,y}$ with $N_{x,y}$ the number of gridpoints in the x and y directions. Ideal scaling corresponds to a flat line with increasing number of processors. This figure illustrates that the LES code exhibits strong scaling for different combinations of problem size and 2D domain decompositions. a) Green \blacklozenge problem size 512^3 ; b) Red \blacklozenge 1024^3 ; c) Black \blacklozenge 2048^3 ; d) Orange \blacklozenge 3072^3 ; and e) Blue \blacklozenge 3072^3 . Cases [a) - d)] are timing tests performed on Franklin while case e) is a timing test on Hopper. For a given number of total processors NP the symbols are different vertical and horizontal decompositions, i.e., different combinations of (NP_z, NP_{xy}) as depicted in Fig. 5.